MULTI-MODAL QUANTITATIVE MICROWAVE AND SHEAR WAVE IMAGING FOR BREAST TUMOR IDENTIFICATION

A THESIS SUBMITTED TO
THE GRADUATE SCHOOL OF NATURAL AND APPLIED SCIENCES
OF
MIDDLE EAST TECHNICAL UNIVERSITY

BY

DAMLA ALPTEKİN SOYDAN

IN PARTIAL FULFILLMENT OF THE REQUIREMENTS
FOR
THE DEGREE OF DOCTOR OF PHILOSOPHY
IN
ELECTRICAL AND ELECTRONICS ENGINEERING

AUGUST 2024

Approval of the thesis:

MULTI-MODAL QUANTITATIVE MICROWAVE AND SHEAR WAVE IMAGING FOR BREAST TUMOR IDENTIFICATION

submitted by **DAMLA ALPTEKİN SOYDAN** in partial fulfillment of the requirements for the degree of **Doctor of Philosophy in Electrical and Electronics Engineering Department, Middle East Technical University** by,

Prof. Dr. Naci Emre Altun
Dean, Graduate School of **Natural and Applied Sciences** ________________

Prof. Dr. İlkay Ulusoy
Head of Department, **Electrical and Electronics Engineering** ________________

Prof. Dr. Nevzat G. Gençer
Supervisor, **Electrical and Electronics Engineering, METU** ________________

Dr. Can Barış Top
Co-supervisor, **ASELSAN A.Ş.** ________________

Examining Committee Members:

Prof. Dr. Gülbin Dural Ünver
Electrical and Electronics Engineering, METU ________________

Prof. Dr. Nevzat G. Gençer
Electrical and Electronics Engineering, METU ________________

Assoc. Prof. Dr. Lale Alatan
Electrical and Electronics Engineering, METU ________________

Prof. Dr. Vakur B. Ertürk
Electrical and Electronics Engineering, Bilkent University ________________

Prof. Dr. Özlem Özgün
Electrical and Electronics Engineering, Hacettepe University ________________

Date: 09.08.2024

I hereby declare that all information in this document has been obtained and presented in accordance with academic rules and ethical conduct. I also declare that, as required by these rules and conduct, I have fully cited and referenced all material and results that are not original to this work.

Name, Surname: Damla Alptekin Soydan

Signature :

ABSTRACT

MULTI-MODAL QUANTITATIVE MICROWAVE AND SHEAR WAVE IMAGING FOR BREAST TUMOR IDENTIFICATION

Alptekin Soydan, Damla
Ph.D., Department of Electrical and Electronics Engineering
Supervisor: Prof. Dr. Nevzat G. Gençer
Co-Supervisor: Dr. Can Barış Top

August 2024, 168 pages

Currently, mammography is used as the standard method for breast cancer screening. However, mammography has drawbacks such as the use of ionizing radiation, low sensitivity in dense breasts, and patient discomfort. To improve the diagnostic and screening performance of existing breast cancer imaging systems, research on multi-modal breast imaging systems, which use different imaging methods together, has increased recently. In this thesis study, a multi-physics, multi-modal imaging technique that combines microwave and shear wave elasticity imaging has been proposed. This method estimates both electrical and mechanical parameters of the tissue quantitatively. The quantitative permittivity map obtained from microwave imaging serves as prior information, guiding shear wave imaging to the suspicious tissues. By utilizing the quantitative Young's modulus values obtained from shear wave imaging, breast tumors can be identified. To investigate the feasibility of the proposed method, numerical studies were conducted to solve both electromagnetic and mechanical forward and inverse problems. To demonstrate the performance of the method experimentally, microwave imaging and shear wave imaging experiments were conducted using a phantom that has fibroglandular and tumor inclusions with a diameter of 20 mm. The results showed that tumor inclusion can be identified quantitatively with a maximum relative permittivity of 41.58 and maximum Young's modulus of 48.5 kPa. The results were found consistent with the reference ground truth values ($\varepsilon_{r_{tumor}}^{ref}$ = 44.8, $\mathrm{YM}_{tumor}^{ref}$ = 46.7 kPa). The tumor identification was achieved through the combined use of multi-modal quantitative microwave and shear wave elasticity imaging.

Keywords: breast cancer detection, multi-modal imaging, quantitative microwave imaging, shear wave elasticity imaging

ÖZ

KANTİTATİF MİKRODALGA VE KESME DALGASI ELASTİKİYETİ GÖRÜNTÜLEME İLE MEME TÜMÖRÜ TESPİTİ

Alptekin Soydan, Damla
Doktora, Elektrik ve Elektronik Mühendisliği Bölümü
Tez Yöneticisi: Prof. Dr. Nevzat G. Gençer
Ortak Tez Yöneticisi: Dr. Can Barış Top

Ağustos 2024 , 168 sayfa

Günümüzde meme kanseri taraması için standart yöntem olarak mamografi kullanılmaktadır. Ancak mamografinin iyonize radyasyon kullanımı, yoğun memelerde düşük hassasiyet ve hastaya rahatsızlık vermesi gibi dezavantajları vardır. Mevcut meme kanseri görüntüleme sistemlerinin tanı ve tarama performansını artırmak amacıyla, farklı görüntüleme yöntemlerini bir arada kullanan çok-modlu meme görüntüleme sistemlerine yönelik araştırmalar son dönemde artmıştır. Bu tez çalışmasında, meme kanseri tanısını geliştirmek amacıyla mikrodalga ve kesme dalgası elastikiyet görüntülemeyi birleştiren çok modlu bir görüntüleme tekniği önerilmiştir. Bu yöntem, nicel elektriksel ve mekanik parametreleri birlikte değerlendirmektedir. Mikrodalga görüntülemeden elde edilen nicel dielektrik haritası, kesme dalgası görüntülemeyi şüpheli dokulara yönlendiren bir ön bilgi sağlar. Bu ön bilgi kullanılarak, kesme dalgası görüntülemeden elde edilen nicel Young modülü değerleri ile meme tümörü tespiti mümkün olabilmektedir. Önerilen yöntemin uygulanabilirliğini araştırmak için hem elektromanyetik, hem de mekanik ileri ve geriçatım problemleri çözülmüştür. Yönte-

min performansını deneysel olarak göstermek için, çapı 20 mm olan silindirik formda fibroglandüler ve tümör içeren bir fantom kullanılarak mikrodalga görüntüleme ve kesme dalgası elastikiyet görüntüleme deneyleri gerçekleştirilmiştir. Sonuçlar, tümör fantomunun maksimum 41.58 göreceli elektriksel geçirgenlik ve maksimum 48.5 kPa Young modülü ile nicel olarak tanımlanabildiğini göstermiştir. Sonuçlar, referans değerlerle ($\varepsilon_{r_{tumor}}^{ref}$ = 44.8, YM$_{tumor}^{ref}$ = 46.7 kPa) uyumlu bulunmuştur. Tümör tespiti, çok-modlu nicel mikrodalga ve kesme dalgası elastikiyet görüntülemesinin bir arada kullanılması sayesinde gerçekleştirilmiştir.

Anahtar Kelimeler: meme kanseri tespiti, çok-modlu görüntüleme, kantitatif mikrodalga görüntüleme, kesme dalgası elastografi

To Deniz . . .

ACKNOWLEDGMENTS

First of all, I would like to thank my supervisor Prof. Dr. Nevzat G. Gençer. I want to express my gratitude to him due to the entire support and assistance he gave me throughout my thesis study.

I would like to express my sincere thanks to my co-supervisor Dr. Can Barış Top. I want to present my gratitude to him for his valuable time, inspiring discussions, suggestions, and guidance on my thesis. I present my endless appreciation to him.

I would also like to thank Prof. Dr. Mustafa Kuzuoğlu, Prof. Dr. Gülbin Dural Ünver, Prof. Dr. Vakur Ertürk, Assoc. Prof. Dr. Lale Alatan, and Prof. Dr. Özlem Özgün for having accepted to examine this work and for their valuable comments and insights.

I would like to thank the members of the METU BERG group, Önder Tetik, Mehmet Soner Gözü, and Volkan Tanrıverdi for their friendship and support.

I am grateful to ASELSAN A.Ş. for all facilities it offered me during my thesis studies

My sincere thanks go to my dear friend Ümit İrgin, for his help during difficult times, as well as for his encouragement, and support. He always found a way to help and motivated me to never hesitate in asking for his assistance.

I would like to thank my friends for all the great time we spent together and for all the love and support I have always felt by my side: Begüm Sönmez, Öykü Çobanoğlu, Dilek Baysal, and Tutku Bakan, and Tuğba Can. You all have been extraordinary examples and sources of motivation for me in my hard times.

I would like to thank Feza Turgay Çelik for his support and friendship, and I am especially grateful to Dr. Kamil Karaçuha for bringing joy to my life every time we met and for offering help in any way he could.

I would like to thank Feza Mutlu. I fondly remember the time we spent together during my long Ph.D. journey. I am deeply grateful for the motivation, encouragement, support, and the kindness and love she showed me.

I would like to thank Şirin Yazar Buran for her lovely friendship, support, and assistance during my Ph.D. Knowing I could always rely on her, seek her advice, and benefit from her valuable insights continually motivated and helped me. I am confident that she will also achieve great success in her own doctoral journey.

I would like to thank Dr. Koray Kadaş for being a wonderful friend who was always there when I needed him, for making the time we spent together enjoyable. I believe that our friendship will continue even after many years.

I would like to express my sincere thanks to Sefa Karaca. I am grateful for his endless support during the most challenging periods of my thesis, including many days and nights, for being a source of joy during the most hopeless moments. Although he is at the beginning of his academic career, his wisdom and ability to generate new ideas were invaluable. I feel both privileged and lucky to have the opportunity to work with such a remarkable colleague.

I would like to thank the Soydan family for their love, support, and encouragement. Their belief in me helped me to believe in myself as well. I feel very lucky to have them as my family.

I would like to thank my father Kamil Alptekin and my sister Duygu Alptekin Avcı. During my desperate times, they were always the first ones I turned to and have always been there to love and support me under any circumstances. It would be impossible to imagine myself in my current position without their everlasting love and encouragement. I am absolutely grateful to have them as my family.

Finally, I would like to thank my husband Yusuf Soydan. All I ever wanted, all I ever needed is here. Therefore, the words are very unnecessary. Thank you . . .

TABLE OF CONTENTS

LIST OF TABLES

TABLES

LIST OF FIGURES

FIGURES

LIST OF ABBREVIATIONS

2D	2 Dimensional
3D	3 Dimensional
MRI	Magnetic Resonance Imaging
MWI	Microwave Imaging
SWE	Shear Wave Elastography
ROI	Region of Interest
HMMDI	Harmonic Motion Microwave Doppler Imaging
FDTD	Finite Difference Time Domain
CPML	Convolutional Perfectly Matched Layer
GN	Gauss-Newton
TM-z	Transverse Magnetic-to-z
FD	Finite Difference
GD	Gradient Descent
FBTS	Forward-Backward Time-Stepping
TTP	Time-to-Peak
TTPS	Time-to-Peak-Slope
IQ	In-phase and Quadrature
DOF	Depth-of-Field
SNR	Signal-to-Noise Ratio

CHAPTER 1

INTRODUCTION

Breast cancer is a disease in which abnormal breast cells grow out of control and form tumours. In 2022, 2.3 million women around the world were diagnosed with breast cancer [4]. Currently, the standard method for the breast screening is mammography. However, mammography has drawbacks such as utilization of ionizing radiation, low sensitivity in dense breasts, and patient discomfort. Other traditional techniques, such as magnetic resonance imaging (MRI) and ultrasound, are mainly used to complement mammography for further investigation of suspicious findings. However, both methods have a high rate of false positives [5,6]. Additionally, MRI is costly and generally not easily accessible, and ultrasound imaging accuracy is highly dependent on the operator [7]. These limitations in current imaging techniques have led to research on finding alternative, safe, non-invasive, sensitive, and cost-effective methods for breast tumor imaging.

Studies have shown that there is a contrast between breast tissue, healthy tissues, and tumor tissues at microwave frequencies [2, 8–11]. These findings have initiated research on microwave imaging as an alternative breast imaging method.

Microwave imaging (MWI) is a technique which relies on the contrast of the dielectric properties (permittivity and conductivity) between the target and its surrounding medium. In microwave imaging, an imaging domain is illuminated by transmit antennas with low-power, non-ionizing electromagnetic waves, and the scattered data collected by the receiving antennas are used to infer information about the target [12–14]. Collected backscattered data can be within the frequency range of 0.5 - 9 GHz [15]. This technique, being safe, non-invasive, and cost-effective, is widely employed for biomedical applications, especially in breast cancer [15–21] and stroke detection [22–27].

Microwave imaging data can be either qualitative or quantitative depending on the reconstruction method [28]. Qualitative methods, such as radar based methods, focus on the presence and location of the target, if any exists. On the other hand, quantitative methods (microwave tomography) aim to reconstruct the complex permittivity distribution by solving non-linear scattering equations iteratively. Quantitative methods are more informative, as they provide information not only about the shape and position but also about the physical properties (i.e. dielectric parameters) .

In microwave breast imaging, extensive work has been done in both qualitative and quantitative studies, including testing a wide range of algorithms in numerical and experimental research [12, 16, 29]. Microwave imaging can currently be described as being in a clinical acceptance phase before transitioning to clinical practice [7]. Current operational qualitative and quantitative microwave systems have been reviewed in [15]. Although patient imaging studies have shown promising results for breast cancer detection, imaging becomes challenging in dense breasts due to the small contrast in dielectric properties [15].

In [2, 11], the dielectric properties of breast tissues from 100 patients (total 330 tissue samples) aged 28 to 85 years old were measured and compared with the dielectric properties of cancerous tissues. For the measurements, healthy tissues were classified into three groups:

- High Density Tissues: Healthy breast tissues with high water content and low adipose content less than 20%
- Medium Density Tissues: Healthy breast tissues with adipose content between 20 and 80%
- Low Density Tissues : Healthy breast tissues with low water content and high adipose content greater than 80%

The results, considering all types of healthy and tumorous tissues and the average values of the measured dielectric properties are shown in the Figure 1.1.The results demonstrate that normal breast tissues display a broad range of permittivity values and

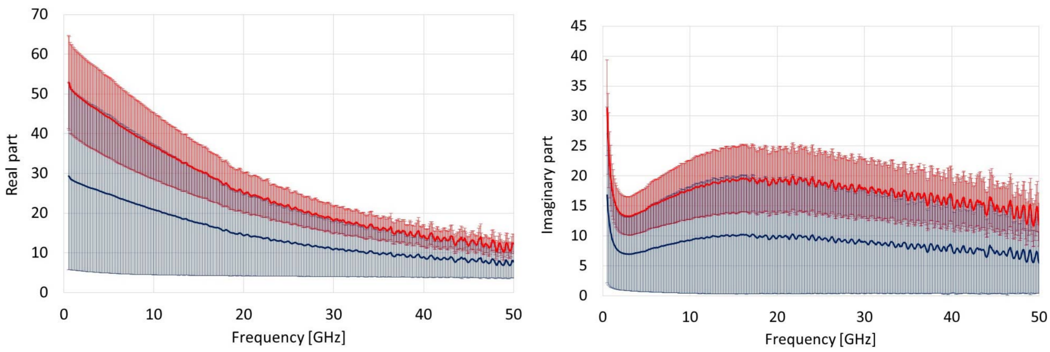

(a) (b)

Figure 1.1: Comparison between the relative dielectric permittivity of normal and tumorous tissues: (a) real part; (b) imaginary part. The red solid line indicates the mean value for the tumorous tissues, while the blue solid depicts the normal tissues. The shaded region refers to the variable region defined by the ± 1 standard deviation. The figure is retrieved from [2]

.

in some instances, the dielectric properties of denser tissues and cancerous tissues can overlap [2, 9–11].

Another alternative method for breast screening is ultrasound elastography. In ultrasound elastography, the mechanical properties of tissues (tissue stiffness) are measured noninvasively in response to an applied mechanical force [30–33]. *Ex-vivo* studies [34–37] have found that the Young's modulus of tumors is 1.5-16 times higher than that of normal breast tissues, and *in-vivo* studies [38, 39] have reported the modulus to be 1.1-7.8 times higher. Therefore, using the contrast in tissue stiffness, breast cancer detection may be possible.

Several ultrasound elastography techniques using different excitation methods have been developed. In general, these methods can be classified into two types [40]: strain imaging methods, which use internal or external compression forces, and shear wave elasticity imaging, which uses ultrasound-generated forces and tracks traveling shear waves. The strain imaging provides a qualitative evaluation of tissue stiffness, on the other hand, shear wave elasticity imaging provides quantitative measure of tissue Young's modulus (or shear modulus) for diagnosis.

In shear wave elastography (SWE), an acoustic radiation force generated by a high-intensity ultrasound beam is used to induce a tissue deformation. This deformation is tracked using ultrasound and based on this deformation, the Young's modulus of the tissues are estimated [33].

The shear wave elasticity imaging techniques can be broadly divided into two categories [40].The first technique, point SWE involves applying an acoustic radiation force to a single focal location. Then, by tracking the resulting shear waves, Young's modulus values are estimated quantitatively [41–43]. At the same time, the operator can obtain morphological images Using B-mode ultrasound. Currently, Siemens Virtual TouchTM Quantification (VTQ/ARFI) and Philips Elast-PQTM are the two commercially available products that uses point SWE [40].

The second technique, 2D-SWE, generates an acoustic radiation force at multiple focal points to create a near-cylindrical shear wave cone [44,45]. By monitoring these waves, the Young's modulus is quantitatively determined and visualized as a colored image along with B-mode images. This method is the newest, and commercially available systems using this technology include Siemens - Virtual TouchTM Imaging Quantification (VTIQ/ARFI), SuperSonic Imagine - Shear WaveTM Elastography, Philips Shear Wave Elastography, GE Healthcare 2D-SWE, and Toshiba Acoustic Structure QuantificationTM (ASQ).

Shear wave elasticity imaging was successfully used in clinical studies for the characterization of breast lesions [46, 47]. However, several factors can affect the performance of shear wave elasticity imaging. As a physical factor, when shear waves induced in the tissue propagate through a heterogeneous medium, interference, diffraction, and attenuation occur [48]. In addition, shear waves disperse as they propagate due to the viscoelasticity of the tissues. In both cases, the tracking of shear waves is affected leading to either overestimation or underestimation of the Young's modulus values [48]. Another consideration in the shear wave elasticity imaging is the operator dependency. Depending on the applied force to the transducer during the measurements, and depending on the orientation of the transducer, the shear wave speed estimations may vary [49]. Additionally, the performance of shear wave elasticity imaging is influenced by the selection of the region of interest (ROI) [50]. In a typical measurement procedure, the position of the focal point is determined near the ROI, and the waves are tracked within this region. However, the selection of the ROI is subjective and operator-dependent. Misplacement of the ROI can lead to varying elasticity parameter results. Finally, the output intensity of the push pulse is another important factor affecting shear wave speed estimation. In [51], it was observed that with a lower energy push pulse, shear wave measurements were failed, whereas increasing the push energy improved the success rate. Although shear wave elastography has some limitations, ongoing research aims to enhance its clinical use and imaging performance as a diagnostic method.

1.1 Motivation of the Thesis

Although several methods exist for breast cancer detection, the research continues to enhance the clinical efficacy of imaging systems in terms of sensitivity and specificity. To improve the diagnostic and screening performance of existing imaging systems, research on multi-modal breast imaging systems, which use different imaging methods together, have increased recently [52–60].

In [52, 53], magnetic resonance imaging (MRI) and microwave imaging were used together. MRI was used to acquire spatial information, which was then incorporated into the regularization process of the microwave image reconstruction algorithm. Simulations with numerical breast phantoms demonstrated that electrical property estimation for separate tissue zones could be enhanced. In 2024 [54], a microwave imaging system was integrated into an MRI system, and phantom experiments were conducted with data acquired simultaneously while being imaged in the MRI system. The initial results are promising, and research on the integration of MRI and microwave tomography for breast cancer detection is ongoing.

In addition to MRI studies, there have also been microwave imaging studies utilizing spatial information obtained from ultrasound imaging. [55, 56, 61, 62]. In [61], B-mode ultrasound images were incorporated as structural guidance into the microwave image reconstructions. Phantom studies demonstrated that with the geometry of the target and background known a prior from ultrasound, successful dielectric property images can be recovered. In [55, 62], the structural prior information, also known as spatial priors, derived from qualitative ultrasound imaging, was integrated into microwave imaging for the detection of tumors within the breast. These studies, tested in realistic numerical breast phantoms, showed that the accuracy of the reconstructed microwave images increases.

Rather than spatial information, multi-model methods which utilize multi-physics information were also studied [57,58,63,64]. In [57], joint inversion of electromagnetic and acoustic data has been studied on numerical breast phantoms, considering speed of sound and attenuation for ultrasound imaging, as well as dielectric parameters for microwave imaging. Imaging modalities were combined assuming that dielectric and acoustic parameters share the same distribution of discontinuity. The reconstruction results showed that the quality of reconstructed images are enhanced. In [58], breast phantoms, with acoustic and dielectric properties similar to real breast tissues, were measured using a dual-mode microwave imaging and ultrasound imaging system. The ultrasound imaging system was used to produce images of the acoustic speed of the phantoms quantitatively and this information was incorporated into the microwave imaging system. As a result, quantitative images of acoustic speed and complex-valued relative permittivity were obtained.

Another multi-physics based breast imaging method called as Harmonic Motion Microwave Doppler Imaging (HMMDI) method was proposed in [59, 65]. This novel method combined focused ultrasound and radar techniques to obtain data based on mechanical and electrical properties of the tissue. The feasibility of the HMMDI method was evaluated in detail in numerical and experimental studies [59, 65–71]. The studies showed that the imaging of coupled elastic and dielectric contrasts increased the reliability of tumor detection and enabled the detection of cancerous tumors hidden inside normal connective and fibroglandular breast tissues.

In another study [60], strain imaging with ultrasound and microwave imaging was performed using the dielectric and mechanical properties of breast tissue. Phantom experiments were conducted, resulting in qualitative millimeter-wave and elastography images. The promising preliminary results indicate that millimeter-wave, ultrasound, and elasticity imaging can be used jointly to detect tumor-like targets.

Similarly, [72], ultrasound and strain elastography imaging were integrated with an existing microwave breast imaging system, which measures average bulk permittivity. Simple phantom experiments were conducted, resulting in bulk permittivity images and qualitative strain images.

In the aforementioned studies where electrical and mechanical properties were used together, these parameters were not directly reconstructed. Instead, the presence and location of objects were detected, and qualitative information was obtained in terms of the contrast between dielectric and mechanical parameters. On the other hand, quantitative results are more informative than qualitative methods because they provide information about the physical properties of the object in addition to the information gained from qualitative methods. For example, in [73], microwave imaging was used for the breast scans of patients undergoing neo-adjuvant chemotherapy, and an increase in the dielectric properties of the tumor region was observed in a patient whose tumor did not respond to treatment. Therefore, obtaining quantitative values is important not only for tumor diagnosis and staging but also for monitoring treatment progress.

In this thesis study, a multi-physics, multi-modal imaging technique that combines microwave and shear wave elasticity imaging has been proposed to enhance breast cancer diagnosis. Using these imaging methods, quantitative values of both the electrical and mechanical parameters of tissues can be obtained.

In addition, using microwave and shear wave elasticity imaging methods together compensates for each other's limitations and provides complementary information. Combined shear and microwave imaging offers advantages over using only microwave or only shear wave elasticity imaging as follows.

– Evaluating quantitative electrical and mechanical parameters data together, provide more information compared to using only one method.

– Combining microwave imaging with shear wave elasticity imaging will enhance accuracy in microwave imaging by potentially reducing the rate of false positives and false negatives. This is particularly important in cases where the dielectric contrast between tissues is low, such as with healthy fibroglandular tissues, which can be misidentified and not easily distinguished. However, since tumors are generally stiffer than fibroglandular tissue, they can be detected using shear wave elasticity imaging. By integrating information from shear wave elasticity imaging, tumors that might not be detected by microwave imaging alone can be identified.

– Since shear wave elasticity imaging is typically used with B-mode ultrasound, obtained B-mode images can provide a morphological reference for microwave imaging. The integration of the B-mode ultrasound and elastography data can help improving the resolution of microwave imaging.

– Microwave imaging provides additional information to shear wave elasticity imaging by giving a map of electrical properties which shows possible regions of interest for tumors. Since ultrasound imaging will be applied to the suspicious region, the accuracy of the Young's modulus estimation can be improved.

– Another advantage microwave imaging provides is that operator can perform shear wave elasticity imaging only to the suspected areas instead of scanning the entire tissue for tumor detection. This reduces the scanning time for shear wave elasticity imaging.

– Additionally, both methods can be improved by using the results obtained from one method as prior information for reconstruction in the other. For example, spatial (structural) priors can be used to enhance sensitivity and specificity in tumor detection.

– Lastly, the multi modal use of shear wave and microwave imaging method is cost effective compared to previously suggested multi-modal MRI or computed ultrasound tomography methods. Since shear wave elasticity imaging is already used in clinical settings, microwave imaging can be feasibly integrated.

To the best of authors' knowledge, this is the first study to propose combining microwave imaging and shear wave elasticity imaging as a multi-modal approach to quantitatively determine electrical and mechanical properties for breast tumor detection. The schematic for the proposed imaging method is given in Figure 1.2. The contributions of this thesis can be summarized as follows:

– For the first time, the quantitative information provided by both the electrical and mechanical properties of tissue is utilized for breast tumor detection.

– To demonstrate the feasibility of the method, numerical simulation tools for solving both the forward and inverse problems in microwave and shear wave elasticity imaging have been developed.

– In the solution of the inverse problem for microwave imaging, adjoint methods have been examined in detail. Different adjoint methods have been categorized into two main groups and compared in detail for the first time. This study has been published [74].

– A tissue phantom was developed that includes both tumors and fibroglandular tissues, presenting a challenging scenario for microwave imaging.

– The feasibility of the proposed multi-modal approach was tested experimentally using the same phantom. The obtained quantitative microwave image is used as a map for shear wave elasticity imaging, which is then applied to the region of interest. The quantitative values for both mechanical and electrical properties were obtained.

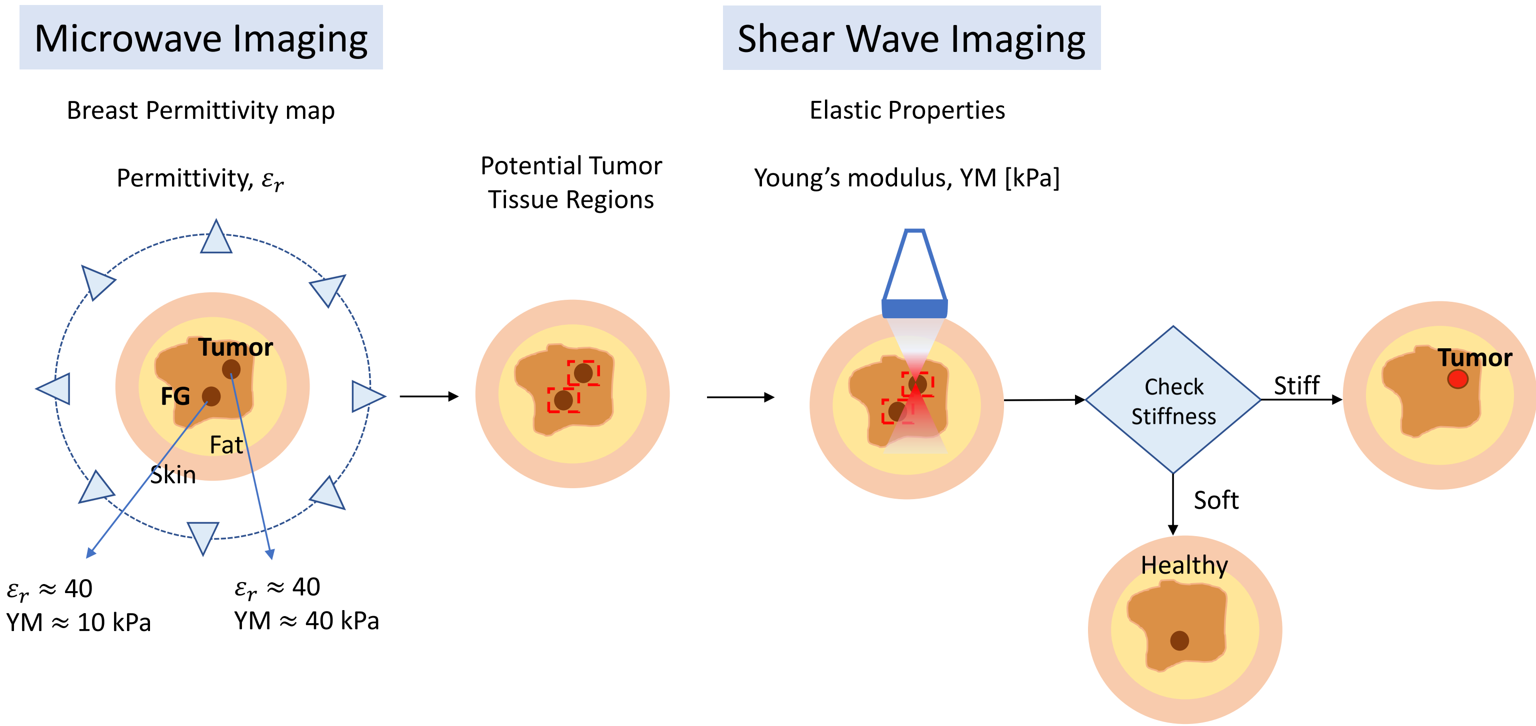

Figure 1.2: While healthy fibroglandular (FG) and tumor tissues have similar dielectric properties, they differ in elasticity, with the tumor being stiffer than the healthy FG tissues. The quantitative permittivity map obtained from microwave imaging serves as prior information, guiding shear wave imaging to the suspicious tissues. By utilizing the quantitative Young's modulus values obtained from shear wave imaging, breast tumors can be identified.

1.2 The Outline of the Thesis

This thesis consists of six chapters.

In Chapter 2, numerical simulations for the microwave imaging are presented. The microwave imaging simulations have been divided into two parts as the forward problem and the inverse problem. For the forward problem solution, 2D Finite Difference Time Domain Method (FDTD) is used. In the inverse problem, the cost function is formulated as the Euclidean distance between the measured and predicted data and is minimized through an iterative process using a Gauss-Newton based algorithm with Levenberg-Marquardt regularization. A simple 2D cylindrical target has been simulated and the quantitative reconstruction results are provided. In addition, in the solution of the inverse problem imaging for microwave imaging, the different applications of the adjoint method in microwave imaging are investigated in detail.

In Chapter 3, numerical simulations for the shear wave elasticity imaging are presented. The shear wave elasticity imaging simulations have been divided into two parts as the forward problem and the inverse problem. In the forward problem, the velocity-stress equations are solved using 2D-FDTD. In the inverse problem, the time-of-flight method, namely time-to-peak-slope, is used to determine Young's modulus values. A simple 2D cylindrical target has been simulated and the quantitative reconstruction results are provided.

In Chapter 4, the development of realistic breast phantoms for experimental analysis is presented. The elasticity and electromagnetic properties of the developed phantoms are measured. Two breast tissue phantoms are developed for the experiments, each containing fibroglandular tissue and tumor inclusions with a diameter of 20 mm. Microwave imaging phantom was developed for microwave imaging only, without considering elasticity differences, whereas multi-modal imaging phantom was developed to conduct both microwave and shear wave elasticity imaging experiments.

In Chapter 5, the proposed method is experimentally evaluated using the developed breast phantoms. Initially, microwave imaging is conducted to identify potential regions of interest for tumor detection. Subsequently, using the quantitative dielectric distribution map from the microwave imaging as prior information, shear wave elasticity imaging is applied to the suspicious areas to obtain quantitative Young's modulus values. The results demonstrate that tumor identification is achieved through the combined use of multi-modal quantitative microwave and shear wave elasticity imaging.

CHAPTER 2

QUANTITATIVE MICROWAVE IMAGING

In microwave imaging, the target is surrounded by antennas and illuminated (See Figure 2.1). While one antenna used as transmitter, the remaining antennas operate as receivers. Each antenna sequentially acts as the transmitter, and the back-scattered data is acquired. In quantitative microwave imaging, often referred to as microwave tomography, the back-scattered data is used to determine the location, size, and dielectric properties (specifically, the quantitative permittivity and conductivity values) of the target. Throughout this thesis, "microwave imaging" refers to "microwave tomography".

In the forward problem of the microwave imaging, electromagnetic fields are calculated for a known distribution of dielectric parameters. On the other hand, in the inverse problem, the received electromagnetic field data are used to infer information about the target. Starting with an initial guess, the forward problem is solved, and the dielectric properties are updated until a convergence criterion is met. In each iteration, the forward problem is solved for each antenna in transmit mode, leading to a significant computational load. Therefore, due to the high computational demands of inverse and also the forward problems, the imaging is generally conducted in a 2D domain to improve computational efficiency.

In this chapter, microwave imaging simulations have been divided into two parts : the forward problem, and the inverse problem. Both problems have been solved using 2D-FDTD, and the results are presented.

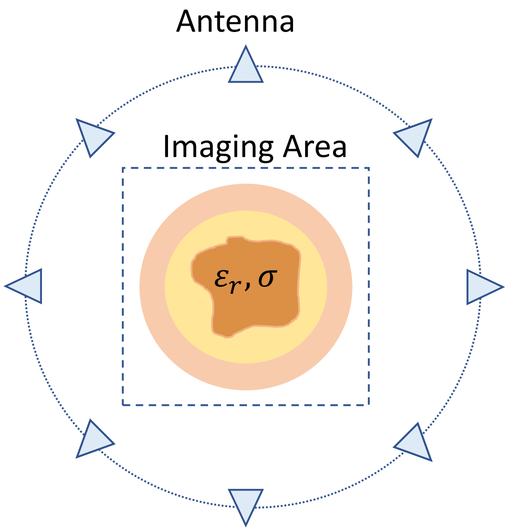

Figure 2.1: Schematic illustration of a typical microwave imaging setup. Antennas are circularly arranged around the target. The backscattered data can be used to infer information about location, shape, and dielectric properties (permittivity– ε_r and conductivity–σ) of the object.

2.1 Forward Problem

In the forward problem, the distribution of the electromagnetic properties of the object is known and received electric and/or magnetic fields at the desired locations are calculated by illuminating the object using the surrounding antennas. For the calculation of the received electric field, both analytical and numerical methods can be used. However, analytical solutions are available only for the certain cases such as homogeneous, layered, and circular (or spherical) targets [75]. Since the biomedical applications involve complex geometries and dispersive media, numerical methods are widely preferred for the forward problem solution.

In this thesis study, finite difference time domain (FDTD) method which is the most popular numerical technique for solving complex electromagnetic problems [76] has been used, since it is i) suitable to model heterogeneous biological tissues, ii) effective to obtain multi-frequency data, and iii) easy to implement.

2.1.1 2D FDTD

In the FDTD method, the time and space domain derivatives of the Maxwell equations are approximated using finite differences. The derivations are performed using sufficiently small space (Δx) and time steps (Δt). While discretizing the field values, singularities must be avoided and tangential continuity of the fields must be satisfied at the medium interfaces. These problems can be overcome by using the FDTD lattice developed by Yee [77].

For 2D TM-mode electromagnetic problem with a current source $\mathbf{J} = J_z(x, y, t)\ \hat{a}_z$, the Maxwell equations for the electric field $E_z(x, y, t)$, and magnetic fields $H_x(x, y, t)$ and $H_y(x, y, t)$, can be expressed as

$$\begin{aligned} \frac{\partial E_z(x,y,t)}{\partial y} &= -\mu(x,y)\frac{\partial H_x(x,y,t)}{\partial t}, \\ \frac{\partial E_z(x,y,t)}{\partial x} &= -\mu(x,y)\frac{\partial H_y(x,y,t)}{\partial t}, \\ \frac{\partial H_y(x,y,t)}{\partial x} - \frac{\partial H_x(x,y,t)}{\partial y} &= \epsilon(x,y)\frac{\partial E_z(x,y,t)}{\partial t} \\ &\quad + \sigma(x,y)E_z(x,y,t) + J_z(x,y,t), \end{aligned} \tag{2.1}$$

where $\mu(x, y)$ is the permeability, $\epsilon(x, y)$ is the permittivity, and $\sigma(x, y)$ is the conductivity distribution of the medium. In the microwave imaging case, $\mu(x, y) = \mu_0$, due to the non-magnetic nature of biological tissues. Using the Yee's FDTD scheme [77] and sampling the electric field at $t = n\Delta t$ and the magnetic field at $t = (n + 1/2)\Delta t$, Equation (2.1) can be discretized as follows

$$\frac{E_z^n(i,j+1) - E_z^n(i,j)}{\Delta y} = -\mu\frac{H_x^{n+1/2}(i,j+1/2) - H_x^{n-1/2}(i,j+1/2)}{\Delta t}. \tag{2.2}$$

Then the update equation for H_x field can be written as

$$H_x^{n+1/2}(i,j+1/2) = H_x^{n-1/2}(i,j+1/2) - \frac{\Delta t}{\mu\Delta y}\left[E_z^n(i,j+1) - E_z^n(i,j)\right]. \tag{2.3}$$

Similarly, the update equations for the H_y and E_z fields can be written as

$$H_y^{n+1/2}(i+1/2,j) = H_y^{n-1/2}(i+1/2,j) + \frac{\Delta t}{\mu\Delta x}\left[E_z^n(i+1,j) - E_z^n(i,j)\right] \tag{2.4}$$

$$
\begin{aligned}
E_z^{n+1}(i,j) = C_a(i,j) E_z^n(i,j) \\
&+ C_b(i,j) \left[\frac{H_y^{n+1/2}(i+1/2,j) - H_y^{n+1/2}(i-1/2,j)}{\Delta x} \right] \\
&- C_b(i,j) \left[\frac{H_x^{n+1/2}(i,j+1/2) - H_x^{n+1/2}(i,j-1/2)}{\Delta y} \right] \\
&- C_b(i,j)\, J_z^{n+1/2}(i,j)
\end{aligned}
\tag{2.5}
$$

where

$$
C_a(i,j) = \frac{2\,\epsilon(i,j) - \sigma(i,j)}{2\,\epsilon(i,j) + \sigma(i,j)} = \frac{1 - \frac{\sigma(i,j)\Delta t}{2\,\epsilon(i,j)}}{1 + \frac{\sigma(i,j)\Delta t}{2\,\epsilon(i,j)}}
$$

and

$$
C_b(i,j) = \frac{2\Delta t}{2\epsilon(i,j) + \sigma(i,j)} = \frac{\frac{\Delta t}{2\,\epsilon(i,j)}}{1 + \frac{\sigma(i,j)\Delta t}{2\,\epsilon(i,j)}}.
$$

2.1.2 2D FDTD using Convolutional Perfectly Matched Layer

In the previous section, the derivations for the 2D-FDTD equations were given for an unbounded medium. However, since the simulation domain is finite size, reflections are created from the surrounding boundaries. To eliminate these reflections, convolutional perfectly matched layer (CPML) boundaries have been implemented [76, 78, 79]. The CPML is based on the stretched coordinates and 2D Maxwell's equations using stretched coordinates can be written as ([76])

$$
\frac{\partial \varepsilon_0 E_z}{\partial t} + \sigma E_z + J = s_x(t) * \frac{\partial H_y}{\partial x} - s_y(t) * \frac{\partial H_x}{\partial y}, \tag{2.6}
$$

$$
-\frac{\partial \mu_0 H_x}{\partial t} = s_y(t) * \frac{\partial E_z}{,} \partial y, \tag{2.7}
$$

$$
\frac{\partial \mu_0 H_y}{\partial t} = s_x(t) * \frac{\partial E_z}{\partial x}, \tag{2.8}
$$

where $*$ denotes convolution operation. The stretch variable s_w can be expressed as

$$
s_w = \kappa_w + \frac{\sigma_w}{\alpha_w + j\omega\varepsilon_0} \quad w = x, y. \tag{2.9}
$$

where κ_w, σ_w, and α_w are one dimensional PML variables which exist only in the PML regions. The expressions for the κ_x, σ_x, and α_x can be written as

$$\kappa_x(x) = 1 + (\kappa_{x,max} - 1)(x/d)^m, \tag{2.10}$$

$$\sigma_x(x) = \sigma_{x,max}(x/d)^m, \tag{2.11}$$

$$\alpha_x(x) = \alpha_{x,max}\left(\frac{d-x}{d}\right)^{m_a}, \tag{2.12}$$

where d is the thickness of the PML region, m is the polynomial grade and typically taken as $3 \geq m \geq 4$, and m_a is the scaling order. The y-components, κ_y, σ_y, and α_y, can be calculated similarly.

The values for $\kappa_{x,max}$, $\sigma_{x,max}$, and d (the thickness of the PML or the number of PML cells) need to be optimized according to the imaging geometry. For example, if $\sigma_{x,max}$ is too small, the primary reflection from the PML is due to its perfect electrical conductor backing. However, if it is too large, discretization error dominates [76]. Thus, there are optimal values for PML parameters that balance reflections and discretization error. A common method to determine optimal values is to calculate the field values in an unbounded free space without PML (assuming no reflection errors), then test different PML parameters, and choose the ones that give the lowest relative error as the optimal parameters [76].

The convolution terms given in (2.6) - (2.8) can be evaluated using recursive convolution (RC) technique [76]. Using the discrete time and space approximations and the RC approximation of the convolution integrals, the update equations can be expressed as

$$\begin{aligned} H_x^{n+1/2}(i,j+1/2) &= D_a(i,j+1/2)\, H_x^{n-1/2}(i,j+1/2) \\ &\quad - D_b(i,j+1/2)\left[\frac{E_z^n(i,j+1) - E_z^n(i,j)}{\kappa_y(j+1/2)\Delta y} + \Psi^n_{H_{xy}}(i,j+1/2)\right] \end{aligned} \tag{2.13}$$

$$H_y^{n+1/2}(i+1/2,j) = D_a(i+1/2,j)\ H_y^{n-1/2}(i+1/2,j) \\ - D_b(i+1/2,j)\left[\frac{E_z^n(i+1,j) - E_z^n(i,j)}{\kappa_x(i+1/2)\Delta x} + \Psi^n_{H_{yx}}(i+1/2,j)\right] \tag{2.14}$$

$$\begin{aligned} E_z^{n+1}(i,j) = {} & C_a(i,j)\ E_z^n(i,j) \\ & + C_b(i,j)\ \left[\frac{H_y^{n+1/2}(i+1/2,j) - H_y^{n+1/2}(i-1/2,j)}{\kappa_x(i)\Delta x}\right] \\ & - C_b(i,j)\ \left[\frac{H_x^{n+1/2}(i,j+1/2) - H_x^{n+1/2}(i,j-1/2)}{\kappa_y(j)\Delta y}\right] \\ & + C_b(i,j)\ \left[\Psi^{n+1/2}_{E_{zx}}(i,j) - \Psi^{n+1/2}_{E_{zy}}(i,j)\right] \\ & - C_b(i,j)\ J_z^{n+1/2}(i,j) \end{aligned} \tag{2.15}$$

where

$$D_a(i,j+1/2) = \left(1 - \frac{\sigma^*(i,j+1/2)\Delta t}{2\mu(i,j+1/2)}\right) / \left(1 + \frac{\sigma^*(i,j+1/2)\Delta t}{2\mu_(i,j+1/2)}\right)$$

$$D_b(i,j+1/2) = \left(\frac{\Delta t}{\mu(i,j+1/2)}\right) / \left(1 + \frac{\sigma^*(i,j+1/2)\Delta t}{2\mu(i,j+1/2)}\right)$$

$$C_a(i,j) = \frac{2\ \epsilon(i,j) - \sigma(i,j)}{2\ \epsilon(i,j) + \sigma(i,j)} = \frac{1 - \frac{\sigma(i,j)\Delta t}{2\ \epsilon(i,j)}}{1 + \frac{\sigma(i,j)\Delta t}{2\ \epsilon(i,j)}}$$

$$C_b(i,j) = \frac{2\Delta t}{2\epsilon(i,j) + \sigma(i,j)} = \frac{\frac{\Delta t}{2\ \epsilon(i,j)}}{1 + \frac{\sigma(i,j)\Delta t}{2\ \epsilon(i,j)}}.$$

Note that σ^* corresponds to magnetic losses where $\sigma^* = 0$.

The auxiliary functions $\Psi_{H_{xy}}$, $\Psi_{H_{yx}}$, $\Psi_{E_{zx}}$, and $\Psi_{E_{zy}}$ can be expressed as

$$\begin{aligned}\Psi^n_{H_{xy}}(i,j+1/2) &= b_y(j+1/2)\ \Psi^{n-1}_{H_{xy}}(i,j+1/2)\\ &+ c_y(j+1/2)\left[\frac{E^n_z(i,j+1)-E^n_z(i,j)}{\Delta y}\right]\end{aligned}$$

$$\begin{aligned}\Psi^n_{H_{yx}}(i+1/2,j) &= b_x(i+1/2)\ \Psi^{n-1}_{H_{yx}}(i+1/2,j)\\ &+ c_x(i+1/2)\left[\frac{E^n_z(i+1,j)-E^n_z(i,j)}{\Delta x}\right]\end{aligned}$$

$$\begin{aligned}\Psi^{n+1/2}_{E_{zx}}(i,j) &= b_x(i)\Psi^{n-1/2}_{E_{zx}}(i,j)\\ &+ c_x(i)\left[\frac{H^{n+1/2}_y(i+1/2,j)-H^{n+1/2}_y(i-1/2,j)}{\Delta x}\right]\end{aligned}$$

$$\begin{aligned}\Psi^{n+1/2}_{E_{zy}}(i,j) &= b_y(j)\Psi^{n-1/2}_{E_{zy}}(i,j)\\ &+ c_y(j)\left[\frac{H^{n+1/2}_x(i,j+1/2)-H^{n+1/2}_x(i,j-1/2)}{\Delta y}\right]\end{aligned}$$

where

$$\begin{aligned}b_w &= e^{-\left(\frac{\sigma_w}{\epsilon_0\kappa_w}+\frac{\alpha_w}{\epsilon_0}\right)\Delta t}\\ c_w &= \frac{\sigma_w}{\sigma_w\kappa_w+\kappa_w^2\alpha_w}\left(b_w-1\right)\\ w &= x,y\end{aligned}$$

Note that $\Psi_{H_{xy}}$, $\Psi_{H_{yx}}$, $\Psi_{E_{zx}}$, and $\Psi_{E_{zy}}$ are discrete unknowns stored only in PML regions, and discrete coefficients b_w and c_w are nonzero only in PML regions.

When the update equations of unbounded medium (2.3 - 2.5) and the update equations obtained for the CPML case (2.13 -2.15) are compared, it can be observed that the CPML field updates are similar to the standard FDTD algorithm, with the exception of the convolutional terms and the scaling parameters.

2.1.2.1 Validation of the FDTD

To validate the developed FDTD code, the analytical and numerical solutions for the line source scattering from a circular dielectric cylinder were compared. The analytical solution can be found in [75].

The object with a radius of 40 mm and relative permittivity of 2 has been placed at the center of free-space imaging domain. The antenna was placed at x = 210 mm. The computational domain was terminated with a 12-grid perfectly matched layer (PML) in all directions. The source was implemented as a sinusoidal carrier of a certain frequency, with a Gaussian envelope. The operation frequency was 5 GHz. The problem geometry is presented in Figure 2.2.

For FDTD simulations, the grid size (Δx) was 1.5 mm and the time step was selected as $\Delta t < \Delta x/(2c_0)$ to ensure stability. The total number of time steps was 4000. The received time domain electric field was transformed to the frequency domain, and the field component at 5 GHz was used.

For both numerical and analytical simulations, the z-component of the electric field (E_z) was computed inside the imaging area of 200 mm $\times$ 200 mm. The fields were normalized with respect to their maximum values inside the imaging area.

For the analytical and numerical simulations, the magnitude and phase values of the normalized E_z values inside imaging area are given in Figure 2.3 and Figure 2.4, respectively. In addition, the magnitude and phase of normalized E_z values at $x = 0$ mm cut ($y = [-100, 100]$ mm) are given in Figure 2.5. There are some minor differences between magnitude and phase values which can be caused by the discretization of the FDTD imaging domain. The results show that the analytical and numerical results are close to each other, verifying that the FDTD method was formulated and implemented correctly.

2.2 Inverse Problem

In the inverse problem of the microwave imaging, the scattered data collected by the receiving antennas are used to estimate the dielectric distribution inside the imaging area by solving nonlinear scattering equations. Linear approximations (e.g., Born approximation) can be applied in low-contrast cases (i.e., the dielectric variation is relatively small). However, when there is a significant variation in dielectric properties inside the solution domain, the problem is treated as a non-linear inversion problem. In such cases, the misfit between measured and predicted data is mostly

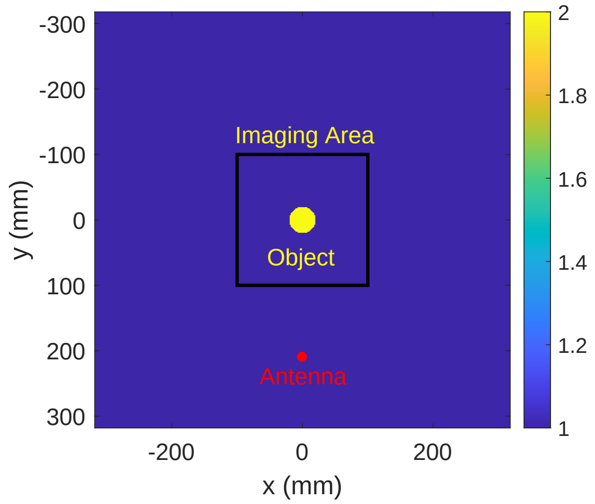

Figure 2.2: Simulation model for the validation of the developed FDTD code. Colorbar shows the relative permittivty values.

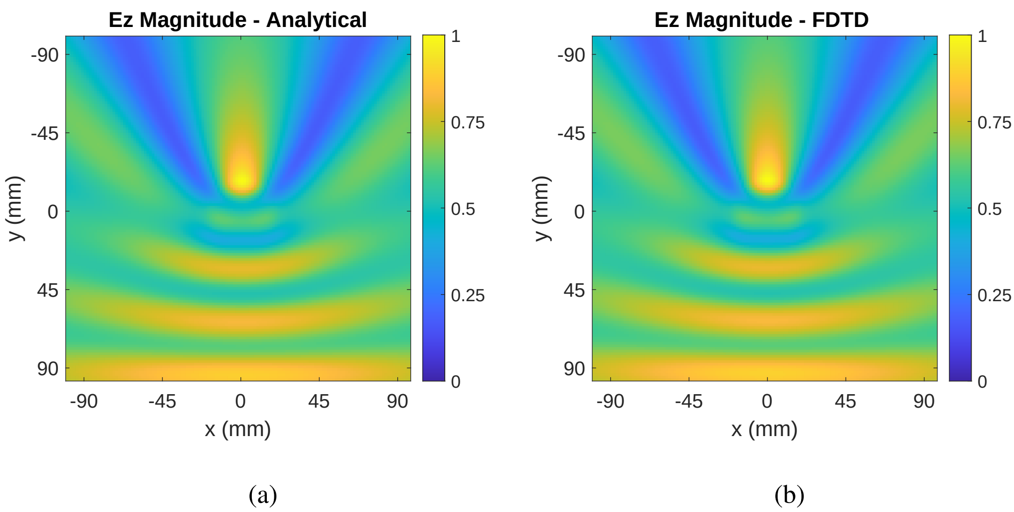

(a) (b)

Figure 2.3: The magnitude values of the normalized E_z values inside imaging area for (a) analytical and (b) FDTD simulations.

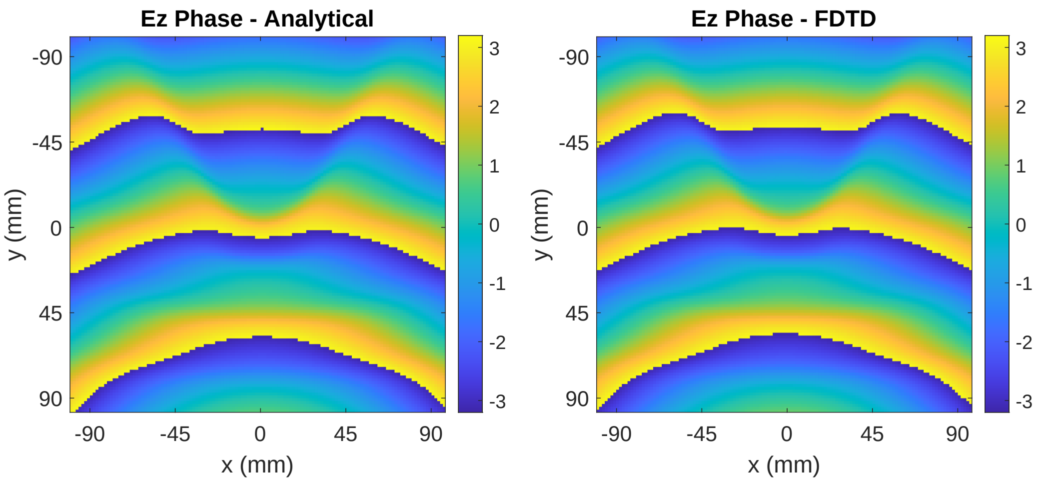

(a) (b)

Figure 2.4: The phase values of the normalized E_z values inside imaging area for (a) analytical and (b) FDTD simulations.

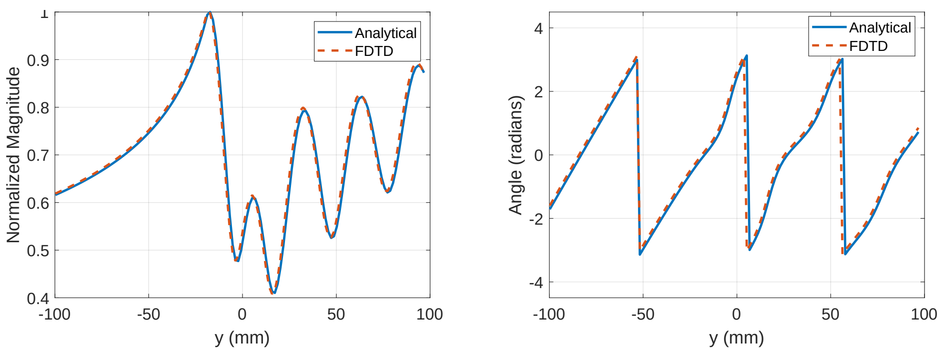

(a) (b)

Figure 2.5: Comparison of analytical results with FDTD results along the center axis of the cylinder. (a) Magnitude values (b) Phase values

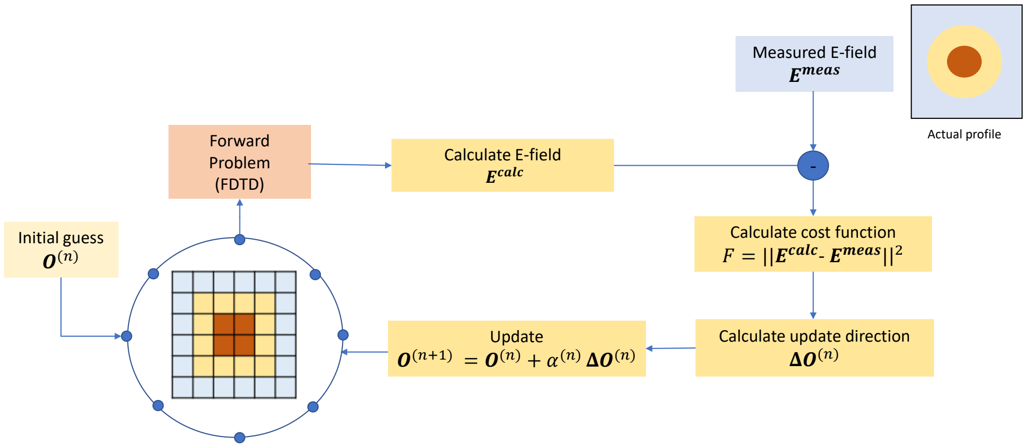

Figure 2.6: Schematic of the inverse problem in microwave imaging. Starting from an initial guess for the dielectric distribution (O), the field values at the measurement points (E^{calc}) are calculated. Using these calculated fields and the measured fields (E^{meas}), the update direction that minimizes the cost function F is found. Then, electrical parameters are updated using update direction ($\boldsymbol{\Delta} O^{(n)}$) and step length ($\alpha$). Note that (n) is the iteration number and each iteration involves a forward problem solution. This procedure continues until the cost functions reaches a minimum value. The figure is adapted from [3] .

defined as Euclidean norm and minimized through an iterative process in which the dielectric distribution is updated.

The inverse problem procedure used in this thesis can be summarized as follows: Starting from an initial guess of the dielectric distribution, the electric field values at the measurement points are calculated. Using these calculated fields, the update direction is found. Then, electrical parameters (i.e., complex dielectric distribution) are updated. Note that, each iteration involves a forward problem solution. This procedure continues until the cost function reaches a minimum value (See Figure 2.6).

2.2.1 Calculation of the Update Direction using Adjoint Method

Note: Most of the material in this chapter have been published in [74].

One of the important steps in the iterative process is the efficient calculation of the update direction. Mainly, two different approaches can be followed to find the update direction with respect to a change in the unknown model parameter. In this section, these approaches are denoted as the direct and indirect methods: 1) The direct method involves calculating the derivative of the cost function, which is then used directly in gradient-descent-based algorithms, 2) the indirect method involves calculating the derivative of the predicted data, known as sensitivity or Jacobian, which is then used in cost function minimization, as in the Gauss-Newton (GN) method. The direct method does not perform an explicit computation of the Jacobian matrix, but the Jacobian is implicitly included in the calculations. On the other hand, the indirect method explicitly calculates the Jacobian matrix. Once the Jacobian matrix is obtained, the derivative of the cost function can also be determined.

The adjoint method is an insightful technique used to understand the impact of changes in system parameters on the system's response. It has found widespread use in many fields, including seismology [80], ultrasound imaging [81], blood flow and clotting [82, 83], diffuse optical tomography [84–86], geophysics [87], photonics [88], and high-frequency structure analysis [89]. Microwave imaging also takes advantage of the adjoint method, which is frequently favored in both frequency domain [90–103] and time domain [104–112] imaging algorithms resulting in diverse formulations.

In this section, the derivative calculations and numerical simulations are described. The derivative calculations are divided into two categories: frequency and time domain formulations, each with two methods - *direct* and *indirect*. In the *direct* method, the derivative of the cost function with respect to relative permittivity distribution was calculated directly. On the other hand, in the *indirect* method, the derivative of the calculated electric field with respect to relative permittivity distribution (also known as sensitivity or *Jacobian* in discrete form) was calculated. The calculations for the derivative of the cost function were adapted from the work by Norton [113] and repeated here for completeness, while the sensitivity calculations in the frequency domain followed the methods outlined in Aghasi et al. [114], which formulates the problem for the Poisson equation. We also present numerical simulation models for two different scenarios involving N antennas. In the first scenario, only one antenna transmits while the others serve as receivers, whereas in the second scenario, each antenna acts as both transmitter and receiver.

2.2.1.1 Formulation in the Frequency Domain

For the transverse magnetic-to-z (TM-z) mode, the equation satisfied by the z-component of the electric field, E_z, in a lossless, isotropic, non-magnetic medium can be written as

$$\nabla^2 E_z(\mathbf{r}) + k_0^2\, \varepsilon_r(\mathbf{r})\, E_z(\mathbf{r}) = s(\mathbf{r}), \tag{2.16}$$

where $\mathbf{r} = (x, y)$ is the position vector, $\nabla^2 = \partial^2/\partial x^2 + \partial^2/\partial y^2$ is the Laplacian operator in the transverse plane, $k_0^2 = \omega^2 \varepsilon_0 \mu_0$ is free-space wave number, ω is the angular frequency, ε_0 is the free space permittivity, μ_0 is the free space permeability, $\varepsilon_r(\mathbf{r})$ is the relative permittivity distribution, $s(\mathbf{r}) = j\omega\mu_0\, J_z(\mathbf{r})$ is source, and J_z is the z-directed electric current density. Considering an imaging scenario with a single transmitter ($N_{tx} = 1$) for simplicity and N_{rx} receivers, the cost function can be defined as

$$F(\varepsilon_r(\mathbf{r})) = \frac{1}{2} \sum_{i=1}^{N_{rx}} \left| E_z(\mathbf{r}_i) - E_z^{meas}(\mathbf{r}_i) \right|^2, \tag{2.17}$$

where $\mathbf{r}_i = (x_i, y_i)$ is the measurement point, $E_z(\mathbf{r}_i)$ and $E_z^{meas}(\mathbf{r}_i)$ are the calculated and measured complex-valued electric fields at $\mathbf{r}_i$, respectively. The derivative of the cost function with respect to the relative permittivity distribution (ε_r) can be expressed as

$$\frac{\partial F(\varepsilon_r)}{\partial \varepsilon_r} = \sum_{i=1}^{N_{rx}} Re \left\{ \left. \frac{\partial E_z}{\partial \varepsilon_r} \right|_{\mathbf{r}=\mathbf{r}_i} \left[E_z(\mathbf{r}_i) - E_z^{meas}(\mathbf{r}_i) \right]^* \right\}, \tag{2.18}$$

where * denotes the complex conjugate.

The *Direct* Method Here, we show that the derivative of the cost function ($\partial F/\partial \varepsilon_r$, i.e., $\boldsymbol{\nabla} F$) can be calculated directly using the adjoint method. The aim of this approach is to determine the derivative of the cost function $\boldsymbol{\nabla} F$ that links the variation in the relative permittivity ($\delta\varepsilon_r$) with the modification in the cost function (δF), which is in the form of

$$\delta F(\varepsilon_r(\mathbf{r})) = \int\limits_S \boldsymbol{\nabla} F(\mathbf{r})\, \delta\varepsilon_r(\mathbf{r})\, d\mathbf{r} \tag{2.19}$$

for an imaging domain of S. Consider an infinitesimal change in the relative permittivity, $\varepsilon_r \to \varepsilon_r + \delta\varepsilon_r$, that causes a small change in the electric field, $E_z \to E_z + \delta E_z$. Inserting these variations in (2.16) and neglecting the small order terms ($k_0^2 \delta\varepsilon_r \delta E_z$) gives

$$\nabla^2 \delta E_z(\mathbf{r}) + k_0^2\, \varepsilon_r(\mathbf{r})\, \delta E_z(\mathbf{r}) + k_0^2 \delta\varepsilon_r(\mathbf{r}) E_z(\mathbf{r}) = 0. \tag{2.20}$$

Inserting the variation in the cost function, $F \to F + \delta F$, in (2.17) gives

$$\delta F(\varepsilon_r) = Re\left\{ \sum_{i=1}^{N_{rx}} \left[E_z(\mathbf{r}_i) - E_z^{meas}(\mathbf{r}_i)\right]^* \delta E_z(\mathbf{r}_i) \right\}. \tag{2.21}$$

Representing $\delta E_z(\mathbf{r}_i)$ as $\delta E_z(\mathbf{r}_i) = \int_S \delta E_z(\mathbf{r}) \delta(\mathbf{r} - \mathbf{r}_i) d\mathbf{r}$, (2.21) becomes

$$\delta F(\varepsilon_r) = Re\left\{ \int\limits_S \sum_{i=1}^{N_{rx}} \left[E_z(\mathbf{r}_i) - E_z^{meas}(\mathbf{r}_i)\right]^* \delta(\mathbf{r} - \mathbf{r}_i) \delta E_z(\mathbf{r}) d\mathbf{r} \right\}. \tag{2.22}$$

Now, consider an adjoint field $\tilde{E}_z$ as a solution to the wave equation

$$\nabla^2 \tilde{E}_z(\mathbf{r}) + k_0^2\, \varepsilon_r(\mathbf{r})\, \tilde{E}_z(\mathbf{r}) = \tilde{s}(\mathbf{r}), \tag{2.23}$$

where the adjoint source was defined as

$$\tilde{s}(\mathbf{r}) = \sum_{i=1}^{N_{rx}} \left[E_z(\mathbf{r}_i) - E_z^{meas}(\mathbf{r}_i)\right]^* \delta(\mathbf{r} - \mathbf{r}_i). \tag{2.24}$$

Note that the expression in (2.24) appears in the integral equation given in (2.22). By inserting the left-hand side of (2.23) to (2.22), and omitting the position dependence in the notations, the expression in (2.22) becomes

$$\delta F(\varepsilon_r(\mathbf{r})) = Re\left\{ \int\limits_S \nabla^2 \tilde{E}_z(\mathbf{r}) \delta E_z(\mathbf{r}) d\mathbf{r} + \int\limits_S k_0^2\, \varepsilon_r(\mathbf{r})\, \tilde{E}_z(\mathbf{r}) \delta E_z(\mathbf{r}) d\mathbf{r} \right\}. \tag{2.25}$$

Using the relation

$$\nabla^2 \tilde{E}_z\, \delta E_z = \nabla \cdot (\delta E_z\, \nabla \tilde{E}_z - \tilde{E}_z\, \nabla \delta E_z) + \tilde{E}_z\, \nabla^2 \delta E_z, \tag{2.26}$$

the first integral in (2.25) can be written as

$$\int\limits_S \nabla^2 \tilde{E}_z(\mathbf{r}) \delta E_z(\mathbf{r})\, d\mathbf{r} = \int\limits_S \tilde{E}_z(\mathbf{r})\, \nabla^2 \delta E_z(\mathbf{r})\, d\mathbf{r}. \tag{2.27}$$

Using the divergence theorem, the first surface integral term on the right-hand side of the (2.26) becomes a contour integral, and since (2.20) and (2.23) are boundary value problems, δE_z and $\tilde{E}_z$ are zero on the boundary contour. As a result, equation (2.25) can be simplified to

$$\delta F(\varepsilon_r(\mathbf{r})) = Re\left\{\int\limits_S \tilde{E}_z(\mathbf{r})\,\nabla^2\delta E_z(\mathbf{r})\,d\mathbf{r} + \int\limits_S k_0^2\,\varepsilon_r(\mathbf{r})\,\tilde{E}_z(\mathbf{r})\delta E_z(\mathbf{r})d\mathbf{r}\right\}. \quad (2.28)$$

Inserting $\nabla^2\delta E_z$ term from (2.20), (2.28) can be expressed as

$$\delta F(\varepsilon_r(\mathbf{r})) = \int\limits_S -k_0^2\,Re\left\{E_z(\mathbf{r})\,\tilde{E}_z(\mathbf{r})\right\}\delta\varepsilon_r(\mathbf{r})\,d\mathbf{r}. \quad (2.29)$$

Using the equivalence between (2.29) and (2.19), the derivative of the cost function can be expressed as

$$\boldsymbol{\nabla} F(\mathbf{r}) = -k_0^2\,Re\left\{E_z(\mathbf{r})\,\tilde{E}_z(\mathbf{r})\right\}. \quad (2.30)$$

This result indicates that independent of the number of receiver antennas (N_{rx}), the derivative of the cost function can be obtained by solving two forward problems. The first forward problem involves the calculation of the electric field (E_z) using (2.16), while the second forward problem (2.23) involves the calculation of the adjoint electric field ($\tilde{E}_z$) . For the second forward problem, the adjoint source is defined in (2.24), where the source corresponds to the sum of residual fields (i.e., the difference between the calculated and measured electric field) at measurement points. In Aghasi et al.'s study [114], this source is denoted as the *composite-source*. Similar terminology is adopted here, with a slight modification, and the source is referred to as the *composite-adjoint-source*.

The *Indirect* Method Unlike the *direct* method, the aim here is to find sensitivity at receiver locations ($\partial E_z/\partial\varepsilon_r|_{\mathbf{r}=\mathbf{r}_i}$, i.e., collection of the kernel functions $K_i(\mathbf{r})$), rather than finding the derivative of the cost function ($\boldsymbol{\nabla} F$) directly. The relation between the change in the relative permittivity ($\delta\varepsilon_r$) to the change in the calculated field at measurement points (δE_{z_i}) can be formulated as

$$\delta E_{z_i}(\varepsilon_r(\mathbf{r})) = \int\limits_S K_i(\mathbf{r})\,\delta\varepsilon_r(\mathbf{r})\,d\mathbf{r}, \quad (2.31)$$

where the kernel functions $K_i(\mathbf{r})$ are the derivative of E_{z_i} with respect to $\varepsilon_r(\mathbf{r})$. Left hand side of (2.31) can be expressed as

$$\delta E_{z_i}(\varepsilon_r(\mathbf{r})) = \int_S \delta(\mathbf{r} - \mathbf{r}_i)\, \delta E_z(\mathbf{r})\, d\mathbf{r}. \tag{2.32}$$

Now, consider an adjoint field $\tilde{E}_{z_i}$ as a solution to the wave equation

$$\nabla^2 \tilde{E}_{z_i}(\mathbf{r}) + k_0^2\, \varepsilon_r(\mathbf{r})\, \tilde{E}_{z_i}(\mathbf{r}) = \tilde{s}_i(\mathbf{r}), \tag{2.33}$$

where we define adjoint-source at the i^{th} receiver as

$$\tilde{s}_i(\mathbf{r}) = \delta(\mathbf{r} - \mathbf{r}_i). \tag{2.34}$$

Note that the adjoint-source $\tilde{s}_i(\mathbf{r}) = \delta(\mathbf{r} - \mathbf{r}_i)$ appears in the integral equation given in (2.32). By inserting the left hand side of (2.33) into (2.32), and following the steps from (2.25) to (2.29) by replacing $\tilde{E}_z$ with $\tilde{E}_{z_i}$, we obtain

$$K_i(\mathbf{r}) = -k_0^2\, E_z(\mathbf{r})\, \tilde{E}_{z_i}(\mathbf{r}). \tag{2.35}$$

This result shows that the sensitivity at a point $\mathbf{r}_i$ can be calculated by solving the forward problem (2.16) to get E_z and the adjoint problem (2.33) to get $\tilde{E}_{z_i}$ for a line current source located at $\mathbf{r}_i$.

By computing the residual field (i.e., the difference between the calculated and measured electric field), and the sensitivities for each receiver (corresponding to N_{rx} forward solutions) the derivative of the cost function defined in (2.18) can be obtained.

2.2.1.2 Formulation in Time Domain

The wave equation in the time domain for a lossless, isotropic, non-magnetic medium can be written as

$$\nabla^2 E_z(\mathbf{r}, t) - \frac{\varepsilon_r(\mathbf{r})}{c_0^2} \frac{\partial^2 E_z(\mathbf{r}, t)}{\partial t^2} = s(\mathbf{r}, t), \tag{2.36}$$

and the initial conditions at $t = 0$ can be defined as

$$E_z(\mathbf{r}, t = 0) = 0 \quad \text{and} \quad \left.\frac{\partial E_z(\mathbf{r}, t)}{\partial t}\right|_{t=0} = 0, \tag{2.37}$$

where $c_0 = 1/\sqrt{\mu_0 \varepsilon_0}$ is the speed of light in free space, and the source is $s(\mathbf{r}, t) = \mu_0(\partial J_z(\mathbf{r}, t)/\partial t)$. Similar to the frequency domain case, a single transmitter ($N_{tx} = 1$) and N_{rx} receivers were utilized. Using the E_z field measured at $\mathbf{r}_i$ over a time interval $[0,\ T]$, the cost function is defined as

$$F(\varepsilon_r(\mathbf{r})) = \frac{1}{2} \sum_{i=1}^{N_{rx}} \int_0^T \left(E_z(\varepsilon_r, \mathbf{r}_i, t) - E_z^{meas}(\mathbf{r}_i, t)\right)^2 \, dt, \tag{2.38}$$

and the derivative of the cost function is expressed as

$$\frac{\partial F}{\partial \varepsilon_r} = \sum_{i=1}^{N_{rx}} \int_0^T \left. \frac{\partial E_z(\mathbf{r}, t)}{\partial \varepsilon_r} \right|_{\mathbf{r}=\mathbf{r}_i} \left[E_z(\mathbf{r}_i, t) - E_z^{meas}(\mathbf{r}_i, t)\right] dt. \tag{2.39}$$

The *Direct* Method Similar to the frequency domain solution, we will seek a formulation in the form of (2.19). Introducing an infinitesimal variation in the relative permittivity and the electric field, the wave equation (2.36) and the cost function (2.38) becomes

$$\nabla^2 \delta E_z(\mathbf{r}, t) - \frac{\varepsilon_r(\mathbf{r})}{c_0^2} \frac{\partial^2 \delta E_z(\mathbf{r}, t)}{\partial t^2} - \frac{\delta \varepsilon_r(\mathbf{r})}{c_0^2} \frac{\partial^2 E_z(\mathbf{r}, t)}{\partial t^2} = 0, \tag{2.40}$$

$$\delta F(\varepsilon_r(\mathbf{r})) = \sum_{i=1}^{N_{rx}} \int_S \int_0^T \left[E_z(\mathbf{r}_i, t) - E_z^{meas}(\mathbf{r}_i, t)\right] \delta(\mathbf{r} - \mathbf{r}_i)\, \delta E_z(\mathbf{r}, t)\, dt\, d\mathbf{r}. \tag{2.41}$$

The wave equation for an adjoint field $\tilde{E}_z(\mathbf{r}, t)$ can be defined in terms of the reverse-time variable τ, where $\tau = T - t$:

$$\nabla^2 \tilde{E}_z(\mathbf{r}, \tau) - \frac{\varepsilon_r(\mathbf{r})}{c_0^2} \frac{\partial^2 \tilde{E}_z(\mathbf{r}, \tau)}{\partial \tau^2} = \tilde{s}(\mathbf{r}, \tau) \tag{2.42}$$

with the following initial conditions at $\tau = 0$ (corresponds to terminal conditions at $t = T$) :

$$\tilde{E}_z(\mathbf{r}, \tau = 0) = 0 \quad \text{and} \quad \left. \frac{\partial \tilde{E}_z(\mathbf{r}, \tau)}{\partial \tau} \right|_{\tau=0} = 0. \tag{2.43}$$

The adjoint-source $\tilde{s}(\mathbf{r}, \tau)$ is defined as

$$\tilde{s}(\mathbf{r}, \tau) = \sum_{i=1}^{N_{rx}} \left[E_z(\mathbf{r}_i, t) - E_z^{meas}(\mathbf{r}_i, t)\right] \delta(\mathbf{r} - \mathbf{r}_i). \tag{2.44}$$

Using (2.42) and (2.44), (2.41) can be expressed as

$$\delta F(\varepsilon_r(\mathbf{r})) = \int_S \int_0^T \left(\nabla^2 \tilde{E}_z(\mathbf{r}, \tau) - \frac{\varepsilon_r(\mathbf{r})}{c_0^2} \frac{\partial^2 \tilde{E}_z(\mathbf{r}, \tau)}{\partial \tau^2} \right) \delta E_z(\mathbf{r}, t)\, dt\, d\mathbf{r}. \tag{2.45}$$

Equation (2.45) can be divided into two integrals: one including the second-order spatial-derivative of the $\tilde{E}_z$, and the other one including the second-order time-derivative of the $\tilde{E}_z$. By following the steps given in (2.26) and (2.27), the first integral can be rearranged as follows

$$\int_S \int_0^T \nabla^2 \tilde{E}_z(\mathbf{r},\tau)\delta E_z(\mathbf{r},t)\, dt\, d\mathbf{r} = \int_S \int_0^T \tilde{E}_z(\mathbf{r},\tau)\nabla^2 \delta E_z(\mathbf{r},t)\, dt\, d\mathbf{r}. \tag{2.46}$$

For the second integral, the derivative with respect to reverse time variable τ is formulated in terms of the time variable t ($\partial^2 \tilde{E}_z(\tau)/\partial \tau^2 = \partial^2 \tilde{E}_z(\tau)/\partial t^2$). Then, integration by parts ($\int_0^T u\, dv = -\int_0^T v du + uv|_0^T$) is applied twice using the initial and terminal conditions given in (2.37) and (2.43). In the first one, u and v are defined as $u = \delta E_z(t)$ and $v = \partial \tilde{E}_z(\tau)/\partial t$, and in the second one, $u = \partial \delta E_z/\partial t$ and $v = \tilde{E}_z(\tau)$. Consequently, the second integral becomes

$$-\int_S \int_0^T \frac{\varepsilon_r(\mathbf{r})}{c_0^2} \frac{\partial^2 \tilde{E}_z(\mathbf{r},\tau)}{\partial t^2}\, \delta E_z(\mathbf{r},t)\, dt\, d\mathbf{r} = -\int_S \int_0^T \frac{\varepsilon_r(\mathbf{r})}{c_0^2} \tilde{E}_z(\mathbf{r},\tau) \frac{\partial^2 \delta E_z(\mathbf{r},t)}{\partial t^2}\, dt\, d\mathbf{r}. \tag{2.47}$$

Therefore, (2.45) can be written as

$$\delta F(\varepsilon_r(\mathbf{r})) = \int_S \int_0^T \left(\nabla^2 \delta E_z(\mathbf{r},t) - \frac{\varepsilon_r(\mathbf{r})}{c_0^2} \frac{\partial^2 \delta E_z(\mathbf{r},t)}{\partial t^2} \right) \tilde{E}_z(\mathbf{r},\tau)\, dt\, d\mathbf{r}. \tag{2.48}$$

Inserting $\nabla^2 \delta E_z(\mathbf{r},t)$ term from (2.40), $\delta F(\varepsilon_r(\mathbf{r}))$ can be expressed as

$$\delta F(\varepsilon_r(\mathbf{r})) = \frac{1}{c_0^2} \int_S \int_0^T \frac{\partial^2 E_z(\mathbf{r},t)}{\partial t^2}\, \tilde{E}_z(\mathbf{r},\tau)\, \delta\varepsilon_r(\mathbf{r})\, dt\, d\mathbf{r}. \tag{2.49}$$

Again, integrating by parts in the time domain ($u = \tilde{E}_z(\tau)$, $v = \partial E_z/\partial t$), (2.49) becomes

$$\delta F(\varepsilon_r(\mathbf{r})) = -\frac{1}{c_0^2} \int_S \int_0^T \frac{\partial E_z(\mathbf{r},t)}{\partial t} \frac{\partial \tilde{E}_z(\mathbf{r},\tau)}{\partial t}\, \delta\varepsilon_r(\mathbf{r})\, dt\, d\mathbf{r}. \tag{2.50}$$

Finally, comparing (2.50) and (2.19), and inserting $\tau = T - t$, the derivative of the cost function is found as

$$\boldsymbol{\nabla} F(\mathbf{r}) = -\frac{1}{c_0^2} \int_0^T \frac{\partial E_z(\mathbf{r},t)}{\partial t} \frac{\partial \tilde{E}_z(\mathbf{r},T-t)}{\partial t} dt \tag{2.51}$$

Similar to the frequency domain results, the derivative of the cost function can be calculated by solving two forward problems: $E_z(\mathbf{r}, t)$ and adjoint field $\tilde{E}_z(\mathbf{r}, \tau)$ can be obtained by solving (2.36) and (2.42) using the sources $s(\mathbf{r}, t)$ and $\tilde{s}(\mathbf{r}, \tau)$, respectively. The adjoint-source $\tilde{s}(\mathbf{r}, \tau)$ given in (2.44) corresponds to the sum of received residual signals. To obtain the adjoint electric field $\tilde{E}_z(\mathbf{r}, \tau)$, this source needs to be propagated backward in time from $t = T$ to $t = 0$. Instead of running the model backward in time, the residual field can be reversed in the time domain and backpropagated [81, 115].

The *Indirect* Method The aim here is to find collection of the sensitivity kernels ($K_{i,p}(\mathbf{r})$) at receiver points $\mathbf{r}_i$ and at time $t = t_p$. Similar to the frequency domain derivations, the sensitivity is computed explicitly. For a given transmitter-receiver configuration, the perturbation in the measured data due to the perturbation in the relative permittivity can be expressed as

$$\delta E_{z_{i,p}}(\varepsilon_r(\mathbf{r})) = \int\limits_S K_{i,p}(\mathbf{r})\, \delta\varepsilon_r(\mathbf{r})\, d\mathbf{r}. \tag{2.52}$$

The δE_{z_i} term can be written as

$$\delta E_{z_i}(\varepsilon_r(\mathbf{r}), t) = \int\limits_S \delta(\mathbf{r} - \mathbf{r}_i)\, \delta E_z(\mathbf{r}, t)\, d\mathbf{r}. \tag{2.53}$$

Now, an adjoint electric field $\tilde{E}_{z_i}(\mathbf{r}, \tau)$ is defined as a solution to the wave equation, where $\tau = T - t$:

$$\nabla^2 \tilde{E}_{z_i}(\mathbf{r}, \tau) - \frac{\varepsilon_r(\mathbf{r})}{c_0^2} \frac{\partial^2 \tilde{E}_{z_i}(\mathbf{r}, \tau)}{\partial \tau^2} = \tilde{s}_i(\mathbf{r}, \tau) \tag{2.54}$$

with initial conditions at $\tau = 0$ (terminal conditions at $t = T$) imposed as

$$\tilde{E}_{z_i}(\mathbf{r}, \tau = 0) = 0 \quad \text{and} \quad \left. \frac{\partial \tilde{E}_{z_i}(\mathbf{r}, \tau)}{\partial \tau} \right|_{\tau=0} = 0. \tag{2.55}$$

The time-dependent adjoint source is defined as

$$\tilde{s}_i(\mathbf{r}, \tau) = h(t)\delta(\mathbf{r} - \mathbf{r}_i), \tag{2.56}$$

where the source is located at $\mathbf{r} = \mathbf{r}_i$. By multiplying both sides of (2.53) with $h(t)$ and integrating in time, we arrive at

$$\int_0^T \delta E_{z_i}(\varepsilon_r(\mathbf{r}), t)\, h(t)\, dt = \int_0^T \int_S \delta E_z(\mathbf{r}, t)\, \tilde{s}_i(\mathbf{r}, \tau)\; dt\; d\mathbf{r}. \tag{2.57}$$

Substituting the left hand side of (2.54) into (2.57) gives

$$\int_0^T \delta E_{z_i}(\varepsilon_r(\mathbf{r}), t)\, h(t)\, dt = \int_0^T \int_S \left(\nabla^2 \tilde{E}_{z_i}(\mathbf{r}, \tau) - \frac{\varepsilon_r(\mathbf{r})}{c_0^2}\, \tilde{E}_{z_i}(\mathbf{r}, \tau)\right) \delta E_z(\mathbf{r}, t)\;\; dt\; d\mathbf{r}, \tag{2.58}$$

which is in similar form of (2.45). Replacing $\tilde{E}_z$ with $\tilde{E}_{z_i}$, and following the steps (2.46) to (2.50), we obtain

$$\int_0^T \delta E_{z_i}(\varepsilon_r(\mathbf{r}), t)\, h(t)\, dt = -\frac{1}{c_0^2} \int_S \int_0^T \frac{\partial E_z(\mathbf{r}, t)}{\partial t} \frac{\partial \tilde{E}_{z_i}(\mathbf{r}, \tau)}{\partial t}\; \delta\varepsilon_r(\mathbf{r})\; dt\; d\mathbf{r}. \tag{2.59}$$

By taking $h(t)$ as a time-line current source with unit amplitude $h(t) = \delta(t - t_p)$, and inserting $\tau = T - t$, then (2.59) can be expressed as

$$\delta E_{z_{i,p}}(\varepsilon_r(\mathbf{r})) = -\frac{1}{c_0^2} \int_S \int_0^T \frac{\partial E_z(\mathbf{r}, t)}{\partial t} \frac{\partial \tilde{E}_{z_i}(\mathbf{r}, \tau)}{\partial t}\; \delta\varepsilon_r(\mathbf{r})\; dt\; d\mathbf{r}. \tag{2.60}$$

By comparing the obtained equation with (2.52), the sensitivity kernels can be written as

$$K_{i,p}(\mathbf{r}) = -\frac{1}{c_0^2} \int_0^T \frac{\partial E_z(\mathbf{r}, t)}{\partial t} \frac{\partial \tilde{E}_{z_i}(\mathbf{r}, T - t)}{\partial t} dt, \tag{2.61}$$

This result implies that sensitivity at a space point $\mathbf{r} = \mathbf{r}_i$ and a time point $t = t_k$ can be calculated by solving the forward problem (2.36), and the adjoint problem (2.54). Depending on the value of t_k, forward and backward propagating fields are cross-correlated [116]. This can be regarded as a convolution of two fields (i.e., the electric field and the adjoint electric field) that are both stepped forward in time [117–119].

2.2.1.3 Numerical Simulations

For numerical simulations, TM-mode 2D FDTD method was utilized. The computational domain was terminated with a 12-grid perfectly matched layer (PML) in all directions. The source was implemented as a sinusoidal carrier with a Gaussian envelope. The operation frequency was 5 GHz and $N = 16$ antennas were placed in a uniform circular arrangement. The geometry utilized in simulations is depicted in Figure 2.7. Excluding the PMLs, the size of the computational domain was 600 mm with a grid size of $\Delta x \leq \lambda_{min}/20$, where $\lambda_{min} = \lambda_0/\sqrt{\varepsilon_{r,max}}$ is the minimum wavelength, and $\varepsilon_{r,max}$ is the maximum value of the relative permittivity. The imaging area was a square region with a side length of 200 mm, and antennas were placed on a radius of 210 mm. The received field was sampled at 2000 time points with time step $\Delta t \leq \Delta x/(2c_0)$. For frequency domain simulations, the received time domain electric field was transformed to the frequency domain, and the field component at 5 GHz was used. Two simulation scenarios were run: 1) single source and (N-1) receivers, and 2) N sources/receivers. The simulations were conducted in both the frequency domain and time domain.

Case - 1: Single Source and $(N-1)$ Receivers In this scenario, one of the antennas was used as the source, and the remaining $(N-1)$ antennas were in receiving mode. In contrast to typical microwave imaging setups where antennas serve as both transmitters and receivers, this particular scenario has been chosen for several reasons. Firstly, it allows for the validation of the derived formulations with minimal computational complexity. Secondly, it helps to gain a clear understanding of the implementation of the adjoint method before making transition to a more realistic imaging configuration. Lastly, it demonstrates the computational effectiveness of the *direct* method when the number of sources is less than the number of receivers.

Frequency Domain Simulations The derivative of the cost function for M grid cells, a single transmitter ($N_{tx} = 1$), and $N_{rx} = N-1$ receiving antennas can be expressed in the frequency domain as

$$\mathbf{f} = Re\{\mathbf{J^T}\mathbf{e}^*\}, \tag{2.62}$$

where $\mathbf{f} \in \mathbb{R}^M$ is the derivative of the cost function (which corresponds to $\partial F/\partial \varepsilon_r$), $\mathbf{J} \in \mathbb{C}^{((N-1)\times M)}$ is the complex-valued Jacobian matrix (i.e., sensitivity, $\partial E_z/\partial \varepsilon_r$) and $\mathbf{e} \in \mathbb{C}^{(N-1)}$ is the complex-valued residual vector, i.e., the difference between

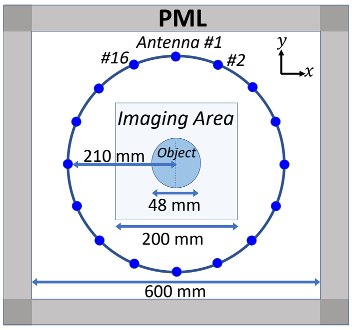

Figure 2.7: Simulation model. The gray shaded area shows the perfectly matched layer (PML) region. A dielectric object was inserted at the center of the imaging domain. The transmitting and receiving antennas were located at the circle with a radius of 210 mm. The square imaging area has a side length of 200 mm. (Note that the drawing is not to scale and is for illustrative purposes only.)

the calculated and measured data. Note that (2.62) corresponds to the vector domain representation of (2.18).

To calculate the derivative of the cost function ($\mathbf{f}$), three simulations were conducted in the frequency domain, and their results were compared: 1) *finite-difference (FD)* method, 2) *direct* method, and 3) *indirect* method. For all simulations, the initial model was selected as an empty background with a relative permittivity of $\varepsilon_r(\mathbf{r}) = 1$.

In the first simulation, the *FD* method was used to calculate the Jacobian matrix. The $(i, j)^{th}$ element of the $[(N-1)\times M]$ matrix is $\partial E_{z_i}/\partial\varepsilon_j$. The sensitivity of the electric field at i^{th} antenna location with respect to permittivity variation at j^{th} grid cell ($\delta\varepsilon_j$) can be expressed as

$$\frac{\partial E_{z_i}}{\partial \varepsilon_j} = \frac{E_{z_i}[\varepsilon_1 \dots \varepsilon_j + \delta\varepsilon_j \dots \varepsilon_M] - E_{z_i}[\varepsilon_1 \dots \varepsilon_j \dots \varepsilon_M]}{\delta\varepsilon_j}. \tag{2.63}$$

A single simulation was run for the initial model, and the received field at each cell in the grid was calculated. Then, the relative permittivity of a single cell was perturbed by 10%, and the simulation was run again to calculate the E_z at receiver points. The amount of perturbation was selected to be small enough to ensure linear approximation, but large enough to avoid numerical errors. A perturbation amplitude of 10% was used since it remains in the validity domain of the linear approximation [120]. Using (2.63) at receiving points ($\mathbf{r} = \mathbf{r}_i$) gives the j^{th} column of the Jacobian matrix.

Simulations were repeated for each grid cell resulting in M simulations. After the calculation of the Jacobian matrix, the derivative vector (**f**) was obtained using (2.62).

In the second simulation, the *direct* method was used to calculate the derivative of the cost function directly instead of computing the Jacobian matrix explicitly. E_z in the simulation domain was calculated using the initial model, and then, the residual data $e_i = E_z(\mathbf{r}_i) - E_z^{meas}(\mathbf{r}_i)$ was calculated at each receiver position. To calculate the adjoint field $\tilde{E}_z$, the residual data at all receiver points was used as the *composite-adjoint-source*. Subsequently, the entries of the derivative of the cost function ($\mathbf{f}$) were calculated by using

$$\frac{\partial F}{\partial \varepsilon_j} = -k_0^2 \int\limits_{S_j} Re\left\{E_z \, \tilde{E}_z\right\} \, d\mathbf{r}, \tag{2.64}$$

where S_j corresponds to the area of the j^{th} grid cell. Note that only two simulations were run to obtain the derivative of the cost function, and the method is independent of the number of grid cells and the number of receivers.

In the third simulation, the *indirect* method was used to calculate the entries of the Jacobian matrix. A single simulation was run for the initial model to calculate the E_z component at each grid cell. Then, i^{th} receiver was used as an adjoint source to obtain the adjoint field $\tilde{E}_{z_i}$. i^{th} row of the Jacobian matrix was calculated by evaluating

$$\left.\frac{\partial E_z}{\partial \varepsilon_j}\right|_{\mathbf{r}=\mathbf{r}_i} = -k_0^2 \int\limits_{S_j} \tilde{E}_{z_i} \, E_z \, d\mathbf{r}. \tag{2.65}$$

Since the field values were calculated at all grid cells, multiplication of the real and adjoint fields provided the i^{th} row of the Jacobian matrix. The simulations were repeated for each receiver, resulting in $(N-1)$ simulations. Then, the computed Jacobian (**J**) was utilized in (2.62) to calculate the derivative of the cost function ($\mathbf{f}$).

Time Domain Simulations Similar to the frequency domain case, the derivative of the cost function for M grid cells, a single transmitter ($N_{tx} = 1$), and $N_{rx} = N-1$ receiving antennas, and N_t time points can be expressed in the time domain as

$$\mathbf{f} = \mathbf{J}^{\mathbf{T}}\mathbf{e}, \tag{2.66}$$

where $\mathbf{f} \in \mathbb{R}^M$ is the derivative of the cost function (which corresponds to $\partial F/\partial \varepsilon_r$), $\mathbf{J} \in \mathbb{R}^{([(N-1)\times N_t]\times M)}$ is the Jacobian matrix (i.e., sensitivity, $\partial E_z(\mathbf{r}, t)/\partial \varepsilon_r$) and $\mathbf{e} \in \mathbb{R}^{[(N-1)\times N_t]}$ is the residual vector, i.e., the difference between the calculated and measured data. Note that (2.66) corresponds to the vector domain representation of (2.39).

Three simulations were conducted to calculate the derivative of the cost function: 1) *FD* method, 2) *direct* method, and 3) *indirect* method. The initial model was selected as an empty background with a relative permittivity of $\varepsilon_r(\mathbf{r}) = 1$. In the first simulation, the *FD* method was used. Time domain electric fields at receiver points were calculated for the initial and perturbed model. As in the frequency domain case, the relative permittivity at the j^{th} grid cell was changed 10% to ensure linearity. The Jacobian matrix was calculated using (2.63) and repeating the simulations for M grid cells. Then, the functional derivative was obtained using (2.66).

In the second simulation, the derivative of the cost function was determined through the *direct* method rather than explicitly calculating the Jacobian matrix. First, $E_z(\mathbf{r}, t)$ was calculated, and then, the adjoint field $\tilde{E}_z(\mathbf{r}, t)$, was calculated by reversing and backpropagating the *composite-adjoint-source* (2.44) in the time domain. The derivative of the cost function was calculated by using (2.51). Analogous to the frequency domain, only two simulations were run to obtain the derivative of the cost function, and the method is independent of the number of grid cells and the number of receivers.

In the third simulation, the *indirect* method was used to calculate the functional derivative. First, the $E_z(\mathbf{r}, t)$ field was obtained at each grid cell. Then, the adjoint source was applied at each receiver to obtain the adjoint field $\tilde{E}_{z_i}(\mathbf{r}, t)$. The Jacobian was calculated by convolving the actual and adjoint fields, and then, (2.66) was used to calculate to calculate the derivative of the cost function (**f**). Note that the residual (**e**) was convolved with the source function used for the adjoint field before computing (2.66) [121, 122]. A total of $(N-1)$ forward simulations, which are independent of the number of grid cells, were required to compute the Jacobian matrix.

To compare the derivative of the cost function obtained with the aforementioned methods, a cylindrical dielectric object with a radius of 24 mm and the highest relative permittivity of $\varepsilon_{r,max} = 2$ was placed at the center of the imaging domain (refer to Figure 2.7). The relative permittivity distribution was

$$\varepsilon_r(x, y) = \begin{cases} (\varepsilon_{r,max} - 1)\sin\left[\frac{\pi(a-r)}{2a}\right] + 1 & 0 \le r \le a, \\ 1 & \text{otherwise,} \end{cases} \tag{2.67}$$

where $r = \sqrt{x^2 + y^2}$ is the magnitude of the position vector $\mathbf{r} = (x, y)$, and a is the radius of the object.

The maps for the derivative of the cost function were calculated by taking the absolute value of the derivative of the cost function ($|\partial F/\partial \varepsilon_r|$, or $|\mathbf{f}|$), and normalizing it to its maximum value.

In terms of implementations, we would like to point out that the source term in (2.16) includes $j\omega\mu_0$ term whereas the adjoint-sources in (2.24) and (2.56) do not. Therefore, in cases where the same forward solver is used for both field and adjoint-field calculations, the sources need to be configured accurately for precise computations. The same is also valid for the time-domain simulations since the adjoint source does not include the time-derivative ($\partial/\partial t$) of the current source.

The flow diagrams for the calculation of the derivative of the cost function, together with the required number of forward simulation runs (FDTD runs), are presented in Figure 2.8.

Case - 2: N Sources / Receivers In this scenario, a realistic microwave imaging configuration is considered in which the antennas were used as both transmitter and receiver. Each antenna sequentially transmits while the response is measured on the remaining $N_{rx} = N - 1$ antennas. For $N_{tx} = N$ transmitter antennas, the cost function was defined as

$$F(\varepsilon_r(\boldsymbol{r})) = \frac{1}{2}\sum_{l=1}^{N_{tx}}\sum_{i=1}^{N_{rx}} \left|E_z(\varepsilon_r, \mathbf{r}_i) - E_z^{meas}(\mathbf{r}_i)\right|^2 \tag{2.68}$$

The flow diagrams for the calculation of the derivative of the cost function are shown in Figure 2.9, along with the number of forward simulation runs.

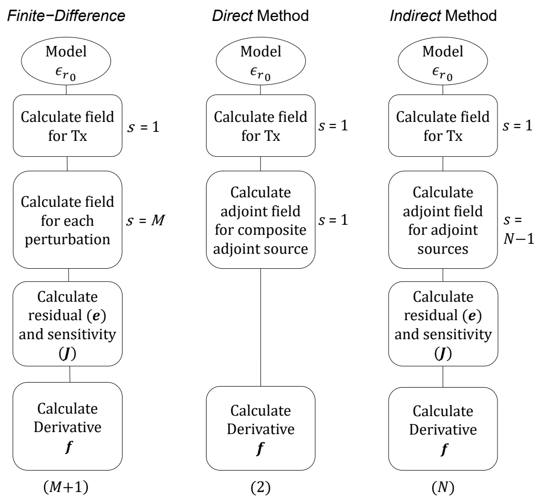

Figure 2.8: Flow diagrams for the calculation of the derivative of the cost function – *single source and* $(N-1)$ *receivers* case. s is the number of forward simulation runs (FDTD runs), M is the number of grid cells, and N is the number of antennas where $M \gg N$. The total number of forward simulation runs was provided at the bottom of the diagrams.

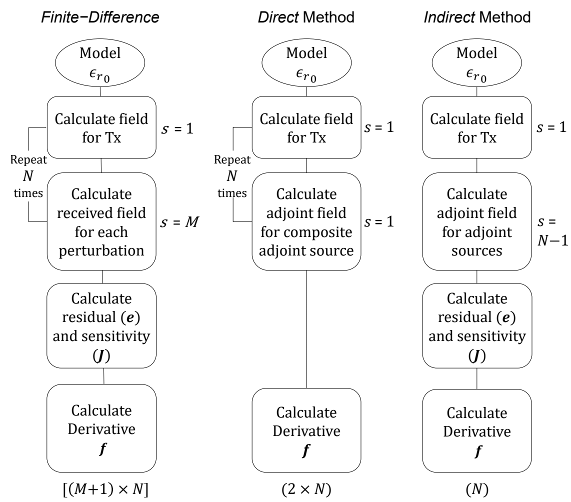

Figure 2.9: Flow diagrams for the calculation of the derivative of the cost function – N *sources and* N *receivers* case. s is the number of forward simulation runs (FDTD runs), M is the number of grid cells, and N is the number of antennas where $M \gg N$. The total number of forward simulation runs was provided at the bottom of the diagrams.

For the *FD* method, the initial and perturbed permittivity distributions were used to calculate the received fields, and then this process was repeated for each transmitter. Similarly, for the *direct* method, the received field due to the *actual* and the *composite-adjoint* sources was calculated for each transmitter. For the *indirect* method, on the other hand, additional calculations were not required as the transmitter antenna changes. Due to reciprocity, the previously calculated adjoint fields, obtained using line current sources at the receivers, can also be utilized as the electric fields generated by the transmit antennas. Likewise, this approach can be applied in cases where field values can be acquired through the utilization of the linearity and scaling.

The maps for the derivative of the cost function were computed for two imaging configurations using the *indirect* method. The calculation of the functional derivative is performed in both frequency and time domains. For the first configuration, the same dielectric object (radius: 24 mm, $\varepsilon_{r,max} = 2$) was used as in the case of a single transmit antenna (See Figure 2.14.a). In the second configuration, the derivative map was computed where two dielectric cylinders with diameters of 15 mm and 21 mm were placed in the imaging domain with 120 mm separation (See Figure 2.15.a). The relative permittivity of the left and right cylinders was defined according to (2.67) with maximum values of 2 and 4, respectively. The imaging area was selected as a rectangular region of 200 mm$\times$80 mm.

2.2.2 Results

2.2.2.1 Case 1: Single Source and $(N-1)$ Receivers

The resulting maps for the derivative of the cost function obtained with a cylindrical object (radius = 24 mm, $\varepsilon_{r,max}$ = 2) using the *FD*, *direct*, and *indirect* methods in the frequency domain are shown in Figure 2.10. In addition, the normalized derivative values at $y = 0$ mm cut ($x =$ [-100,100] mm) and $x = 0$ mm cut ($y =$ [-100, 100] mm) are given in Figure 2.11. Similarly, the obtained results in the time domain are shown in Figure 2.12 and Figure 2.13.

The results show that the derivative values obtained from all methods are in good agreement, verifying that the adjoint method was formulated and implemented correctly in the both frequency and time domains. As a consequence of using only a single transmit antenna to illuminate the object, the information derived from the derivative maps is limited in terms of making inferences about the object. (Detailed results for a more realistic microwave imaging configuration are presented in the subsequent section.)

In terms of computational load, a comparison of the utilized methods shows that the *FD*, *direct*, and *indirect* methods required $(M+1)$, 2, and N forward simulation runs (FDTD runs), respectively. Since the number of unknowns (the grid cell dielectric constants) was greater than the number of antennas ($M \gg N$), the computational burden of the *FD* method was enormous. Therefore, *FD* method is not practical for the iterative solution procedure. For a single source case, the *direct* method was advantageous in terms of the required forward simulation runs since it involved only two forward simulation runs.

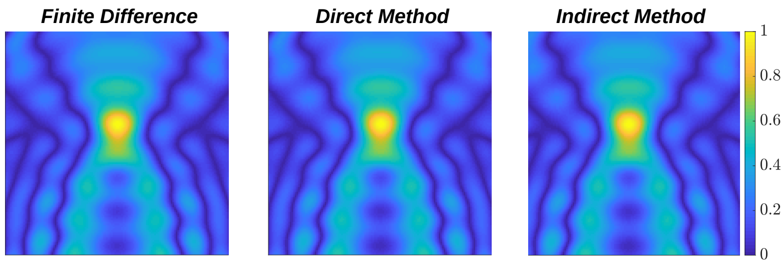

Figure 2.10: Maps for the normalized derivative of the cost function obtained using the *finite-difference* method, *direct* method, and *indirect* method inside the imaging area of 200 mm $\times$ 200 mm for a cylindrical object (radius = 24 mm, $\varepsilon_{r,max}$ = 2). The results are obtained in the frequency domain for the *single source and (N-1) receiver* case. The color bar shows the normalized value of the absolute of the derivatives.

2.2.3 Case 2: N Sources / Receivers

In this scenario, using all antennas sequentially as transmitters allowed information to be obtained about the shape and permittivity distributions of the objects through the derivative of the cost function.

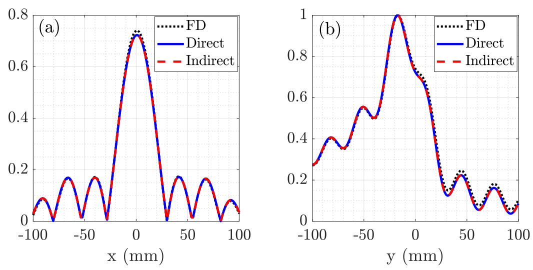

Figure 2.11: Normalized values for the derivative of the cost function at (a) $y = 0$ mm cut ($x =$ [-100, 100] mm). (b) $x = 0$ mm cut ($x =$ [-100, 100] mm) for a cylindrical object (radius = 24 mm, $\varepsilon_{r,max}$ = 2) using the *finite-difference*, *direct*, and *indirect* methods. The results are obtained in the frequency domain for the *single source and (N-1) receiver* case.

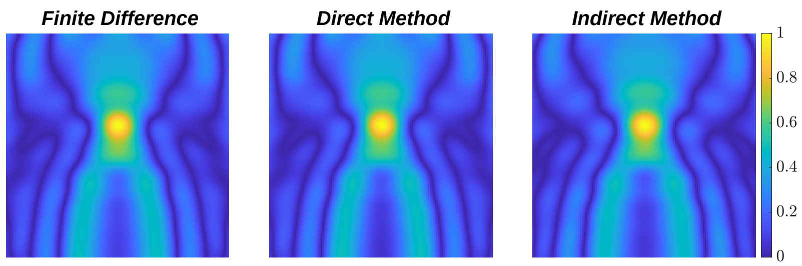

Figure 2.12: Maps for the normalized derivative of the cost function obtained using the *finite-difference* method, *direct* method, and *indirect* method inside the imaging area of 200 mm × 200 mm for a cylindrical object (radius = 24 mm, $\varepsilon_{r,max}$ = 2). The results are obtained in the time domain for the *single source and (N-1) receiver* case. The functional gradient maps appear smoother in the due to the use of broadband frequency-domain information. The color bar shows the normalized value of the absolute of the derivatives.

For the first configuration, the relative permittivity map of the imaging area and the maps for the normalized derivative of the cost function are shown in Figure 2.14. Likewise, Figure 2.15 illustrates the relative permittivity map of the imaging area, the map for the normalized derivative of the cost function, the normalized derivative, and the relative permittivity along the center line for the second configuration. The derivative of the cost function has a smooth variation around the dielectric objects, and a peak around the object centers can be observed for both configurations. In

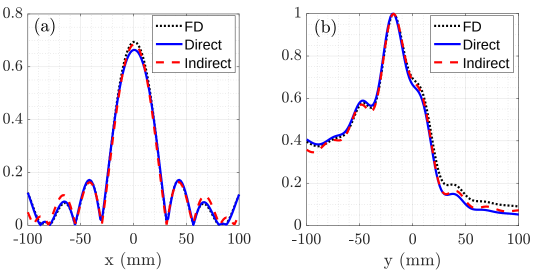

Figure 2.13: Normalized values for the derivative of the cost function at (a) $y = 0$ mm cut ($x =$ [-100, 100] mm). (b) $x = 0$ mm cut ($x =$ [-100, 100] mm) for a cylindrical object (radius = 24 mm, $\varepsilon_{r,max}$ = 2) using the *finite-difference*, *direct*, and *indirect* methods. The results are obtained in the time domain for the *single source and (N-1) receiver* case.

addition, the objects with greater relative permittivity resulted in a higher gradient value (larger amount of change), as expected.

In terms of computational load, compared to the *single source and (N-1) receiver* case, the number of total forward simulation runs was multiplied by the number of antennas (N) for the *FD* and the *direct* methods, resulting $[(M+1) \times N]$ and $(2 \times N)$ forward simulation runs (FDTD runs), respectively (see Figure 2.9). On the other hand, the number of total simulations did not change when the *indirect* method was used. Due to the reciprocity of the antennas, the field distribution was the same (or scaled if the source amplitudes were different) when an antenna radiates the actual source or the adjoint source. Therefore, one forward solution for each antenna, resulting in N forward simulation runs, was adequate to obtain the derivative of the cost function. Consequently, the computational burden of the *FD* method is the greatest compared to the adjoint methods. Among the adjoint methods, the *indirect* method has higher computational efficiency than the *direct* method when the antennas were used as both transmitter and receiver.

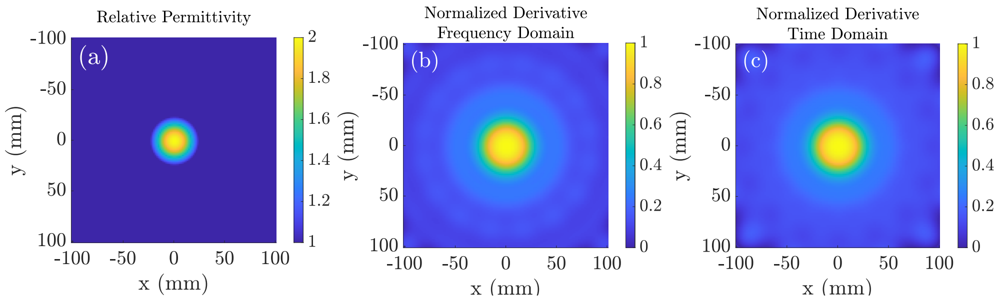

Figure 2.14: Simulation results of the first configuration for a cylindrical object (radius = 24 mm, $\varepsilon_{r,max}$ = 2) inside the imaging area of 200 mm $\times$ 200 mm. (a) Relative permittivity, (b) Normalized derivative of the cost function in the frequency domain, (c) Normalized derivative of the cost function in the time domain. The results are obtained for the N *sources and* N *receivers* case using the *indirect* method.

2.2.4 Discussion

2.2.4.1 Computational Efficiency

The computational efficiency of the *direct* and *indirect* methods depends on the imaging configuration and the utilization of the antennas (or sensors). Note that the computational efficiency is evaluated in terms of the number of forward solution runs since it is the most time-consuming part of the iterative microwave tomography algorithms. For an imaging configuration, assume N_s and N_r correspond to the number of source and receiver antennas, respectively. To calculate the derivative of the cost function using the *direct* approach, $2 \times N_s$ forward simulations are required. On the other hand, for the *indirect* approach, the number of the required forward simulation runs is $N_s + N_r$. However, the transmitters and receivers can be used interchangeably in an imaging scenario where the reciprocity principle holds. Therefore, there is no need to recalculate the field when an antenna switches roles. As a result, the number of forward simulation runs for the *indirect* method reduces to $[N_s + N_r - (N_s \cap N_r)]$ where $(N_s \cap N_r)$ corresponds to the number of antennas that can be used as both transmitter and receiver, i.e., transceivers. If we compare the *direct* and *indirect* methods, the *indirect* method is efficient when $[N_s + N_r - (N_s \cap N_r)] < [2 \times N_s]$. This expression can be simplified as $N_s > [N_r - (N_s \cap N_r)]$, where $(N_s \cap N_r) \geq 0$. Therefore, when $(N_s \cap N_r) = 0$ and the number of sources outweighs the num-

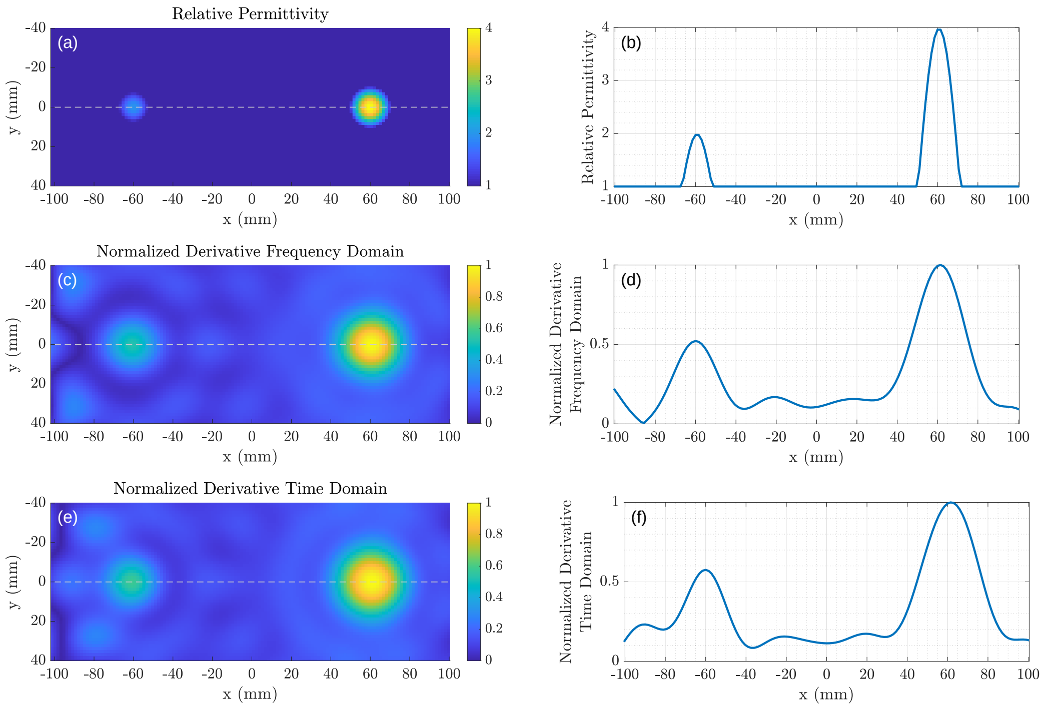

Figure 2.15: Simulation results for the second configuration. (a) Relative permittivity map inside the imaging area of 200 mm $\times$ 80 mm. The cylinders had diameters of 15 mm and 21 mm, and their maximum relative permittivity values were 2 and 4, respectively. (b) Relative permittivity values along $y = 0$ mm cut (x = [-100, 100] mm). (c) Map for the normalized derivative of the cost function in the frequency domain. (d) Normalized derivative values along $y = 0$ mm cut (x = [-100, 100] mm) in the frequency domain. (e) Map for the normalized derivative of the cost function in the time domain. (f) Normalized derivative values along $y = 0$ mm cut (x = [-100, 100] mm) in the time domain. The results are obtained for the N *sources/receivers* case using the *indirect* method.

ber of receivers ($N_s > N_r$), the *indirect* method becomes computationally advantageous [116,121,123,124]. Accordingly, even if one is not interested in the sensitivity or Jacobian, the *indirect* method may still be chosen for calculating the derivative of the cost function due to the smaller number of forward solutions.

In microwave imaging, antennas can function as both transmitters and receivers, with $N_s = N_r = N$, and $(N_s \cap N_r) = N$. As a result, the number of forward solutions required for the *direct* and *indirect* methods can be expressed as $2 \times N$ and N, respectively. It can be observed that the *indirect* method requires half the forward solutions compared to the *direct* method to obtain the functional gradient. Therefore, the *indirect* method provides advantages in certain scenarios even when sensitivity is not required, particularly in scenarios where computational efficiency and reduced forward solutions are crucial factors.

2.2.4.2 Calculation of the Update Direction for Gradient Descent and Gauss-Newton Algorithms

Comparing the obtained results for commonly used Gauss-Newton based iterative algorithms and gradient descent (GD)-based algorithms in microwave imaging would provide valuable perspectives. Note that our aim is not to compare the reconstruction performance of these methods since other reconstruction parameters, such as convergence, regularization, image quality, and signal-to-noise ratio analysis, need to be analyzed, and they are out of scope. Instead, we compared the utilization of the different adjoint methods for calculating the update direction, $\mathbf{u}$, that both GD and GN methods require. The update equation for the unknown model parameter $\mathbf{m}$ (in our case, relative permittivity ε_r) can be expressed as

$$\mathbf{m}^{(n+1)} = \mathbf{m}^{(n)} + \alpha^{(n)}\mathbf{u}^{(n)} \tag{2.69}$$

where n is the iteration number, α is the step length, and $\mathbf{u}$ is the update direction. For gradient-descent algorithm, the update direction $\mathbf{u}$ can be written as

$$\begin{aligned} \mathbf{u} &= -\nabla F \\ &= -\mathbf{J}^T\mathbf{e}, \end{aligned} \tag{2.70}$$

whereas, for Gauss-Newton based iterative algorithm, the update direction $\mathbf{u}$ can be expressed as

$$\mathbf{u} = -\left(\mathbf{J}^T\mathbf{J}\right)^{-1}\mathbf{J}^T\mathbf{e}. \tag{2.71}$$

For gradient descent algorithms, the update direction, $\mathbf{u}$, can be obtained using both the *direct* and *indirect* methods. The *direct* method provides the derivative of the cost function (∇F) directly, while the *indirect* method obtains the functional derivative through the Jacobian and residual ($\mathbf{J}^T\mathbf{e}$). The selection between the *direct* and *indirect* methods depends on the imaging configuration and computational efficiency requirements. For example, in cases where forward solution computation costs are the most substantial, as in microwave imaging, and the antennas can be used as both transmitter and receiver, the *indirect* approach becomes advantageous since it requires a smaller number of forward solutions compared to the *direct* method. Therefore, calculating the *Jacobian* first, then the gradient of the cost function, i.e., the *indirect* method, becomes more efficient. However, it should be noted that this method requires a large-scale and memory-inefficient Jacobian matrix. This problem can be solved by dividing the Jacobian matrix into sub-matrices [121].

On the other hand, for Gauss-Newton based inversion, the update direction, $\mathbf{u}$, requires Jacobian calculation; therefore, a comparison can be made between the *indirect* and *FD* methods. As expected, the *indirect* method leads to better computational efficiency since the number of the grid cells in the imaging domain (M) was greater than the number of antennas ($M \gg N$).

The calculation of the Jacobian matrix offers another noteworthy observation. The Jacobian matrix is calculated row-by-row, where each row is computed by multiplying the actual electric field generated by the transmitter antenna with the adjoint field caused by the receiver antenna, see (2.65). Since the adjoint field is equivalent to the forward solution of the receiver antenna (with a scaling factor), each row of the Jacobian matrix corresponds to the multiplication of the two forward solution vectors associated with the selected pair of transmit and receive antennas [125].

Although Newton-like methods (such as GN and Levenberg-Marquardt) [53,126,127] are widely employed in microwave tomography, quasi-Newton methods (e.g., Broyden–Fletcher–Goldfarb–Shanno — BFGS algorithm) have also been implemented to a limited extent [26, 100, 128–131]. The low adoption of quasi-Newton approaches might be due to the slower convergence rate compared to Newton-like methods [130, 131]. Nevertheless, the quasi-Newton methods perform well for nonlinear, large-scale optimization problems and are frequently employed in ultrasound tomography [132–135]. In quasi-Newton methods, the *Hessian* matrix, which includes the computationally expensive second order derivative terms, is not used directly, but an approximate *Hessian* matrix is calculated using the gradient information obtained from previous iterations [128, 131]. The gradient information (update direction) can be calculated using both the *direct* and *indirect* adjoint approaches, similar to gradient-descent methods. As previously stated, the most computationally efficient method depends on the addressed problem and the imaging configuration.

2.2.4.3 The Comparison of Frequency Domain and Time Domain Adjoint Method

As mentioned in the introduction, frequency domain algorithms are often used more than time domain algorithms in microwave imaging. However, time-domain reconstruction brings the advantage of improved resolution due to its broadband information. Although the same outcome can be achieved through multifrequency or frequency hopping reconstruction techniques [136, 137], they bring the challenge of selecting appropriate frequencies and determining the number of frequencies to be used. Depending on the frequency selection strategy, non-linearity-related inaccuracies may arise in the resulting reconstructions. Therefore, the time-domain reconstruction is considered more robust than frequency-domain algorithms [105,138]. On the other hand, in time-domain algorithms, the initial frequency domain data needs to be calibrated and transformed into the time domain. This requirement arises because microwave tomography experiments are usually conducted using a vector network analyzer, and the broadband data is acquired in the frequency domain.

In terms of computation time, time domain reconstruction methods in microwave tomography literature have been observed to be slower than their frequency domain counterparts [138]. For time-domain reconstructions, the forward-backward-time-stepping (FBTS) method, which utilizes the *direct* adjoint method—where received residual signals are reversed in time and used as sources- is usually preferred. Therefore, the forward problem needs to be solved twice for each transmitter at each iteration. In addition, the FBTS method uses gradient-based algorithms to minimize the cost function iteratively. Instead of using the *direct* method in the time domain, the *indirect* method can provide comparable computational efficiency to the frequency domain. Firstly, the *indirect* method requires half the forward solutions, and secondly, the *indirect* method allows the use of the Gauss-Newton inversion, which converges faster than gradient descent when the initial model is sufficiently close to a local or global minimum. Therefore, using the *indirect* method with Gauss-Newton inversion in the time domain may provide an additional advantage in terms of computation time compared to the frequency domain.

The simulation setup used in this study has been configured to provide a functional gradient map that can serve as a good initial guess in the frequency domain. Therefore, the results of frequency and time domain reconstructions are quite close to each other. When the results for *Case-1* (one source, N-1 receivers) are compared between the frequency domain and time domain, the functional gradient maps appear smoother in the time domain due to the utilization of wideband information.

Lastly, we would like to emphasize that for both frequency domain and time domain algorithms, the map of the derivative of the cost function strongly depends on the imaging configuration (i.e., operation frequency, number, and location of the antennas, size of the computational domain, grid size, etc.) and object parameters (location, size, proximity, and relative permittivity). Therefore, the location of the objects may not be as clearly visible as in the examples of the map of the derivative of the cost function given here. Nevertheless, the resulting derivative maps provide an initial guess and intuition for inverse problems solved by iterative methods.

2.2.4.4 Applications of the Adjoint Method in Inverse Problems

The determination of the update direction using the adjoint method is frequently utilized in inverse problems. Therefore, the concepts presented here are not limited to microwave imaging and apply to scenarios where physical models are characterized by a mathematical framework that involves partial differential equations along with boundary and initial conditions. We would like to briefly provide some examples of inverse problems that utilize the adjoint method for optimization.

In the field of biomedical imaging, the adjoint method is widely used in ultrasound computed tomography [81, 139]. In this technique, the tissue is imaged using ultrasound transducers, and the acquired signals are used to reconstruct acoustic properties. The ultrasound transducers are reciprocal, i.e., the sources (transmitters) and receivers (detectors) can be used interchangeably. Depending on the optimization algorithm, both the *direct* and *indirect* methods can be utilized. Usually, the *direct* adjoint method is used for the *full waveform inversion*. Using the *indirect* adjoint method for the optimization may provide a computational advantage in terms of the number of forward simulations. In addition, the *indirect* method allows the calculation of the Jacobian matrix which can be used in fast converging algorithms. However, it should be noted that this method requires the development of a memory-efficient implementation of the Jacobian matrix.

In addition, the adjoint method finds application in many other disciplines, including seismic [121, 122, 140] and geophysics [114, 116, 141]. In the seismic waveform inversion, seismic waves are generated through a controlled source and detected by seismic sensors placed on the earth's surface. Typically, the number of receivers exceeds the number of sources [142, 143]. Similarly, in ground-penetrating radar tomography, permittivity and conductivity distributions are usually investigated in the shallow subsurface using a few tens to a few hundred receivers [116, 144]. In these methods, the direct method is commonly utilized due to the greater number of receivers compared to sources. Typically, the cost function is minimized through the *direct* method (e.g., gradient-based methods) without calculating the Jacobian matrix. However, the computation of the Jacobian matrix can be preferred, as it provides additional information and allows for the performance of cumulative sensitivity and formal model resolution analyses [116].

2.2.5 Conclusion on the Calculation of the Update Direction using Adjoint Method

In this study, we focused on investigating the different applications of the adjoint method in microwave imaging. We have provided clear and concise analytical expressions for the adjoint formulations, filling a gap in existing literature where such formulations are predominantly presented based on specific applied problems. We classified the update direction calculations using adjoint method into two groups, the *direct* and the *indirect* methods, and presented the derivations independent of the forward solution method. The resulting analytical expressions were verified through numerical simulations, and the computational loads were measured in terms of the number of forward simulation runs. The results have demonstrated the differences between the adjoint methods and have shown the computational efficiency that can be achieved through the proper strategy. Moreover, the study has provided observations into how the method is utilized, thereby enhancing its practical utility.

2.3 Construction of the Jacobian Matrix

In the previous section, the derivations for the update calculations are given for a scenario where the conductivity of the object was not considered [74]. In this section, both permittivity and the conductivity of the object are taken into account, and the derivations are presented.

The Helmholtz equation for a lossy, non-magnetic, isotropic medium can be written as

$$\nabla^2 E + \gamma^2 E = j\omega\mu_0 J_z, \tag{2.72}$$

where

$$\gamma = j\omega\sqrt{(\mu_0\varepsilon_c)} = j\omega\sqrt{(\mu_0\left(\varepsilon_0\varepsilon_r - j\sigma/\omega\right))}, \tag{2.73}$$

and

$$\gamma^2 = -\omega^2\mu_0\left(\varepsilon_0\varepsilon_r - j\frac{\sigma}{\omega}\right) = -\omega^2\mu_0\varepsilon_0\varepsilon_r + j\omega\mu_0\sigma. \tag{2.74}$$

Consider a perturbation to the propagation constant, $\gamma^2 = \gamma^2 + \delta\gamma^2$, resulting in perturbation in the electric field as $E \to E + \delta E$. Then (2.72) becomes

$$\nabla^2(E + \delta E) - \left(\gamma^2 + \delta\gamma^2\right)(E + \delta E) = j\omega\mu_0 J_z, \tag{2.75}$$

$$\nabla^2 E + \nabla^2\delta E - \gamma^2 E - \delta\gamma^2 E - \gamma^2\delta E - \delta\gamma^2\delta E = j\omega\mu_0 J_z. \tag{2.76}$$

Using (2.72) in (2.76) gives

$$\nabla^2\delta E - \delta\gamma^2 E - \gamma^2\delta E - \delta\gamma^2\delta E = 0. \tag{2.77}$$

If small order term $\delta\gamma^2\delta E$ is neglected, the equation (2.77) becomes

$$\nabla^2\delta E - \delta\gamma^2 E - \gamma^2, \delta E = 0 \tag{2.78}$$

The aim is to find a collection of kernel functions, i.e., $K_i(\boldsymbol{r})$ which satisfies

$$\delta E_i = \int_S K_i(\boldsymbol{r})\, \delta\gamma^2(\boldsymbol{r}) d\boldsymbol{r}. \tag{2.79}$$

The kernels are the derivative of E_i with respect to γ^2, which corresponds the change in the electric field at the receiver locations ($\mathbf{r} = \mathbf{r}_i$) due to the change in the γ^2. The δE_i term can also be represented as

$$\delta E_i = \int_S \delta\left(\boldsymbol{r} - \boldsymbol{r}_i\right) \delta E \, d\boldsymbol{r}. \tag{2.80}$$

Now consider an adjoint field $\tilde{E}_i$ as a solution to the adjoint problem

$$\nabla^2 \tilde{E}_i - \gamma^2 \tilde{E}_i = \tilde{s}_i(\boldsymbol{r}), \tag{2.81}$$

where adjoint source is $\tilde{s}_i(\boldsymbol{r}) = \delta\left(\boldsymbol{r} - \boldsymbol{r}_i\right)$. Here $\tilde{E}_i$ is the adjoint field due to line current source of amplitude unity located at the i^{th} receiver.

Then (2.81) becomes

$$\nabla^2 \tilde{E}_i - \gamma^2 \tilde{E}_i = \delta\left(\boldsymbol{r} - \boldsymbol{r}_i\right). \tag{2.82}$$

Notice that $\delta\left(\boldsymbol{r} - \boldsymbol{r}_i\right)$ term appears in the integral equation given in (2.80). By inserting the left-hand side of the (2.82) into (2.80), the expression in (2.80) becomes

$$\begin{aligned} \delta E_i &= \textstyle\int_S \left(\nabla^2 \tilde{E}_i - \gamma^2 \tilde{E}_i\right) \delta E d\boldsymbol{r}, \\ \delta E_i &= \textstyle\int_S \nabla^2 \tilde{E}_i \, \delta E \, d\boldsymbol{r} - \int_S \gamma^2 \, \tilde{E}_i \, \delta E d\boldsymbol{r}, \end{aligned} \tag{2.83}$$

Using the relation

$$\nabla^2 \tilde{E}_i \delta E = \nabla \cdot \left(\delta E \nabla \tilde{E}_i - \tilde{E}_i \nabla \delta E\right) + \tilde{E}_i \nabla^2 \delta E, \tag{2.84}$$

and taking the surface integral of (2.84), the expression in (2.84) becomes

$$\int_S \nabla^2 \tilde{E}_i \delta E d\boldsymbol{r} = \int_s \nabla \cdot \left(\delta E \nabla \tilde{E}_i - \tilde{E}_i \nabla \delta E\right) d\boldsymbol{r} + \int_S \tilde{E}_i \nabla^2 \delta E d\boldsymbol{r}. \tag{2.85}$$

Using the divergence theorem, the first surface integral term on the right-hand side of the (2.85) becomes a contour integral and since (2.78) and (2.81) are boundary value problems, δE and $\tilde{E}_i$ are zero on the boundary contour. Then (2.85) becomes

$$\int_S \nabla^2 \tilde{E}_i \, \delta E \, dr = \int_S \tilde{E}_i \, \nabla^2 \delta E \, dr. \tag{2.86}$$

Inserting right hand-side of (2.86) into (2.83), the expression in (2.83) becomes

$$\delta E_i = \int_S \tilde{E}_i \nabla^2 \delta E d\boldsymbol{r} - \int_S \gamma^2 \tilde{E}_i \delta E d\boldsymbol{r}. \tag{2.87}$$

Inserting $\nabla^2 \delta E$ term from (2.78), the expression in (2.87) becomes

$$\begin{aligned} \delta E_i &= \int_S \tilde{E}_i \left(\delta\gamma^2 E + \gamma^2 \delta E\right) d\boldsymbol{r} - \int_S \gamma^2 \tilde{E}_i \delta E d\boldsymbol{r} \\ \delta E_i &= \int_S \left(\delta\gamma^2 \tilde{E}_i E + \gamma^2 \tilde{E}_i \delta E - \gamma^2 \tilde{E}_i \delta E\right) d\boldsymbol{r} \\ \delta E_i &= \int_S \delta\gamma^2 \tilde{E}_i E d\boldsymbol{r}. \end{aligned} \tag{2.88}$$

Now comparing (2.79) and (2.88), the kernel function $K_i(\boldsymbol{r})$ in (2.79), becomes

$$K_i(\boldsymbol{r}) = \tilde{E}_i(\boldsymbol{r}) E(\boldsymbol{r}), \tag{2.89}$$

which corresponds the change in the electric field at the receiver points due to the change in the γ^2.

Note that, here $\tilde{E}_i(\boldsymbol{r})$ is the adjoint field due to line current source of amplitude unity located at the i^{th} receiver (i.e., $\boldsymbol{r} = \boldsymbol{r}_i$), and is found by solving (2.81) for a lossy, isotropic medium. On the other hand, $E(\boldsymbol{r})$ is found by solving (2.72).

2.3.1 Jacobian Representation in Matrix Form

For the sake of completeness, Jacobian is represented in the matrix form using Taylor's expansion. The Taylor's expansion for the complex electric field can be expressed as

$$E\left(\gamma^2\right) \approx E\left(\gamma_0^2\right) + \frac{\partial E\left(\gamma_0^2\right)}{\partial \gamma^2} \Delta\gamma^2 \tag{2.90}$$

$$E\left(\gamma^2\right) - E\left(\gamma_0^2\right) = \frac{\partial E\left(\gamma_0^2\right)}{\partial \gamma^2} \Delta\gamma^2. \tag{2.91}$$

where the subscript 0 in γ^2 correspond to current value of the γ^2. The difference between the updated and current values can be written as

$$\begin{aligned} \Delta\gamma^2 &= \gamma^2 - \gamma_0^2 \\ \Delta\gamma^2 &= -\omega^2 \mu_0 \varepsilon_0 \left(\varepsilon_r - \varepsilon_{r0}\right) + j\omega\mu_0 \left(\sigma - \sigma_0\right) = -\omega^2 \mu_0 \varepsilon_0 \Delta\varepsilon_r + j\omega\mu_0 \Delta\sigma. \end{aligned} \tag{2.92}$$

Let propagation constant γ^2 is discretized to form a vector $\boldsymbol{\gamma}^2 = [\gamma_1^2, \ldots, \gamma_M^2]$ and $\boldsymbol{E}^{calc}$ is a vector of field values calculated at thereceiver points using the given distribution of constitutive parameters stored in the $\boldsymbol{\gamma}^2$, and $\boldsymbol{E}^{meas}$ is a vector of field values measured at the receiver points for the actual distribution of constitutive parameters.

Considering (2.92), the $\boldsymbol{E}^{calc}$ at the $(n+1)^{th}$ iteration can be expressed as [95]

$$\boldsymbol{E}^{calc}\left(\boldsymbol{\gamma}^{2^{(n+1)}}\right) = \boldsymbol{E}^{calc}\left(\boldsymbol{\gamma}^{2^{(n)}}\right) + \boldsymbol{J}\left(\boldsymbol{\gamma}^{2^{(n)}}\right)\boldsymbol{\Delta\gamma}^{2^{(n)}}. \tag{2.93}$$

Using the residual fields which are defined as

$$\begin{aligned} \boldsymbol{e_R} &= \mathrm{Re}\left(\boldsymbol{E}^{calc} - \boldsymbol{E}^{meas}\right), \\ \boldsymbol{e_I} &= \mathrm{Im}\left(\boldsymbol{E}^{calc} - \boldsymbol{E}^{meas}\right), \end{aligned}$$

and considering the real and imaginary parts of the $\boldsymbol{\gamma}^2$, the linear problem can be written as [145]

$$\left[\ \boldsymbol{J}\ \right]\left[\ \boldsymbol{\gamma}^2\ \right] = \left[\ \boldsymbol{e}\ \right]$$

$$\begin{bmatrix} \frac{\partial\,\mathrm{Re}(\boldsymbol{E})}{\partial\,\mathrm{Re}(\boldsymbol{\gamma}^2)} & \frac{\partial\,\mathrm{Re}(\boldsymbol{E})}{\partial\,\mathrm{Im}(\boldsymbol{\gamma}^2)} \\ \frac{\partial\,\mathrm{Im}(\boldsymbol{E})}{\partial\,\mathrm{Re}(\boldsymbol{\gamma}^2)} & \frac{\partial\,\mathrm{Im}(\boldsymbol{E})}{\partial\,\mathrm{Im}(\boldsymbol{\gamma}^2)} \end{bmatrix} \begin{bmatrix} \mathrm{Re}\left(\Delta\boldsymbol{\gamma}^2\right) \\ \mathrm{Im}\left(\Delta\boldsymbol{\gamma}^2\right) \end{bmatrix} = \begin{bmatrix} \boldsymbol{e_R} \\ \boldsymbol{e_I} \end{bmatrix}. \tag{2.94}$$

The derivative terms of the Jacobian matrix in (2.94) can be calculated using (2.89), where

$$\frac{\partial\,\mathrm{Re}(E)}{\partial\,\mathrm{Re}\left(\gamma^2\right)} = \frac{\partial\,\mathrm{Im}(E)}{\partial\,\mathrm{Im}\left(\gamma^2\right)} = \mathrm{Re}\left(\tilde{E}_i\,E\right), \tag{2.95}$$

and

$$\frac{\partial\,\mathrm{Im}(E)}{\partial\,\mathrm{Re}\left(\gamma^2\right)} = -\frac{\partial\,\mathrm{Re}(E)}{\partial\,\mathrm{Im}\left(\gamma^2\right)} = \mathrm{Im}\left(\tilde{E}_i\,E\right). \tag{2.96}$$

The matrix equation in (2.94) is solved using the Gauss-Newton based iterative algorithm with Levenberg-Marquardt regularization (see next section) and unknown parameters $\mathrm{Re}\left(\Delta\boldsymbol{\gamma}^2\right)$ and $\mathrm{Im}\left(\Delta\boldsymbol{\gamma}^2\right)$ are obtained, where

$$\mathrm{Re}\left(\Delta\boldsymbol{\gamma}^2\right) = -\omega^2\mu_0\varepsilon_0\boldsymbol{\Delta\varepsilon_r},$$

and

$$\mathrm{Im}\left(\Delta\boldsymbol{\gamma}^2\right) = \omega\mu_0\boldsymbol{\Delta\sigma}.$$

Then, the permittivity and conductivity updates can be expressed as

$$\boldsymbol{\Delta\varepsilon_r} = -\operatorname{Re}\left(\Delta\gamma^2\right)/\omega^2\mu_0\varepsilon_0,$$
$$\boldsymbol{\Delta\sigma} = \operatorname{Im}\left(\Delta\gamma^2\right)/\omega\mu_0.$$

2.4 Reconstruction Algorithm

For the microwave tomography, the cost function to be minimized is defined by

$$F(\varepsilon_r, \sigma) = \sum_{i=1}^{N_t}\sum_{i=1}^{N_r} \left|E^{meas}(\mathbf{r_i}) - E^{calc}(\mathbf{r_i})\right|^2, \tag{2.97}$$

where N_t is the number of transmitting antennas, N_r is the number of receiving antennas per transmitter, $\mathbf{r_i}$ is the measurement points $(i = 1, .., N_r)$, $E^{meas}(\mathbf{r_i})$ and $E^{calc}(\mathbf{r_i})$ are the measured and calculated complex-valued electric fields at $\mathbf{r_i}$, respectively. For the solution of the minimization problem, the Gauss-Newton based iterative algorithm which has been widely preferred for the microwave tomography has been used [93, 95, 127, 146, 147]. In this method, a Jacobian matrix is constructed using the calculated fields and an under-determined linear problem is solved using 2.98

$$\boldsymbol{\Delta\gamma}^2 = (\mathbf{J}^T\mathbf{J})^{-1}\mathbf{J}^T(\mathbf{E}^{calc} - \mathbf{E}^{meas}). \tag{2.98}$$

However, since the problem is ill-posed, regularization is used to stabilize the results. The update direction using the Gauss-Newton based iterative algorithm with Levenberg-Marquardt regularization [148, 149] can be expressed as

$$\boldsymbol{\Delta\gamma}^2 = (\mathbf{J}^T\mathbf{J} + \lambda\mathbf{I})^{-1}\mathbf{J}^T(\mathbf{E}^{calc} - \mathbf{E}^{meas}), \tag{2.99}$$

where $\mathbf{I}$ is the identity matrix and λ is the regularization parameter which can be found using 2.100 [150]

$$\lambda = \beta\, err_n \frac{1}{M}\, Trace(\mathbf{J^T J}), \tag{2.100}$$

where $err = \left\|\mathbf{E}^{meas} - \mathbf{E}^{calc}\right\|$, and the normalized relative error was defined as $err_n = err/err(i = 1)$, with respect to the error value at the first iteration, M is the number of grid cells, and β is a parameter which is determined empirically.

The schematic for the inverse problem algorithm is presented in Figure 2.16 and the overall inversion process is summarized as follows:

- Step 1: Compute calculated electric field ($\mathbf{E}^{calc}$) from an initial electrical parameters distribution

- Step 2: Calculate Jacobian matrix (**J**) for the current electrical parameters distribution using 2.94.

- Step 3: Obtain update direction ($\boldsymbol{\Delta\gamma}^2$) by solving (2.99).

- Step 4: Update electrical parameters $\boldsymbol{\gamma}^{2^{(n+1)}} = \boldsymbol{\gamma}^{2^{(n)}} + \alpha^{(n)}\boldsymbol{\Delta\gamma}^{2^{(n)}}$, where n is the iteration number.

- Step 5: Go to Step -1 and continue with the updated electrical parameters.

- Step 6: Continue until a convergence criterion is satisfied.

The algorithm computes the electric field values by solving the forward problem for each antenna, at each iteration. Therefore, the computational burden of the inversion algorithm comes from the large number of forward problem solution requirement.

Note that, step size parameter α can be determined by using advanced algorithms [151]. However, these methods requires additional forward problem calculations resulting in increase in the computational load. Therefore, step size parameter generally selected empirically depending on the imaging scenario [95].

When using this approach, the value of λ is set to a high value in the first few iterations then, it decreases as the algorithm progresses since the reconstructed and actual image distribution becomes closer. Generally, the λ parameter selected empirically by testing testing the inversion algorithm with different λ values [16].

For the convergence, the error was defined as $err(i) = \left\|\mathbf{E}^{meas} - \mathbf{E}^{calc}\right\|$, and the normalized relative error was defined as $err_n(i) = err(i)/err(i = 1)$, where i is the iteration number. The normalized error starts from 1 for the first iteration, and decreases as the iterations continue. The stopping criteria was set according to the error difference between the current and previous iteration, typically less than 0.01. In general, the algorithm converged within 20 to 25 iterations.

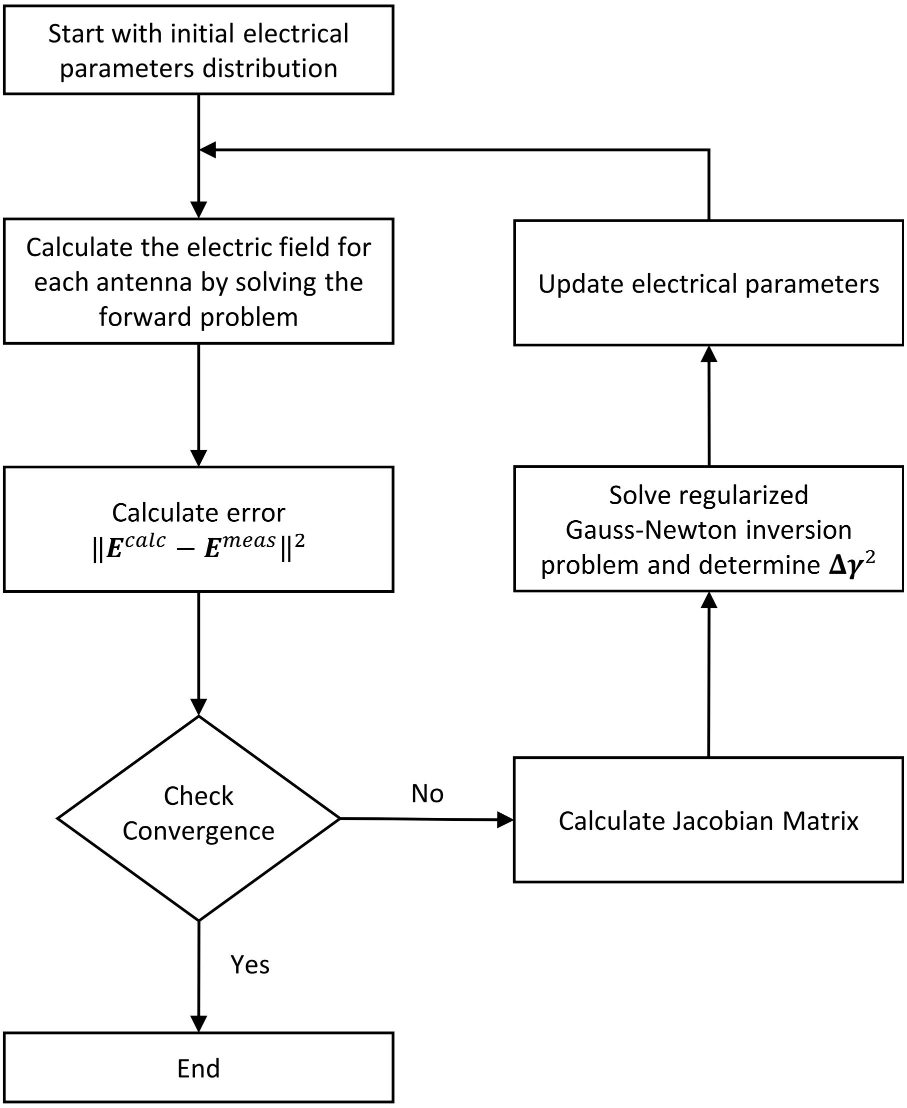

Figure 2.16: The schematic for the inverse problem algorithm.

2.5 Validation of the Algorithm

In this section, a simple 2D cylindrical target has been simulated and the reconstruction results are provided. For the imaging scenario, the background medium is modeled as glycerin-water mixture which is mostly used as coupling medium in microwave imaging experimental setups [92]. The electrical parameters of the background medium is $\varepsilon_{r,b} = 20$, $\sigma_b = 1.3$. As a target, a circular cylinder with a diameter of 20 mm and electrical parameters of $\varepsilon_{r,t} = 45$, $\sigma_t = 2$ is used. The target values are selected close to the tumor/fibroglandular values given in [152]. The target is placed at $x = 0, y = -20$ mm and illuminated using 16 antennas which are centered on the imaging domain with a radius of 80 mm. The imaging area was 90 mm $\times$ 90 mm. The operation frequency was selected as 1.5 GHz. The simulation was run for 16 iterations and terminated when the normalized error reaches below 0.01.

The reconstructed permittivity and conductivity images are given in Figure 2.17. In addition, the reconstruction results are compared along $x = 0$ line and shown in Figure 2.18.

The results indicate that the permittivity and conductivity values have been reconstructed well at the target region. Note that, the permittivity values overshoot the true values as a result of the regularization algorithm. Since the sharp change of the electrical parameters between the target and the background medium is smoothed in the reconstructed image, the algorithm tries to compensate this change with an overshoot at the center region. Similar results can also be observed in [95, 147].

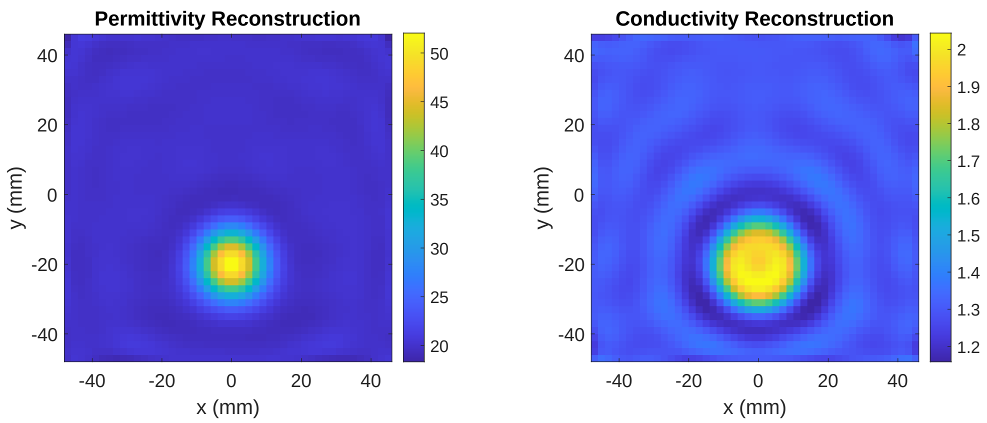

(a) (b)

Figure 2.17: The reconstructed (a) permittivity and (b) conductivity values inside imaging area

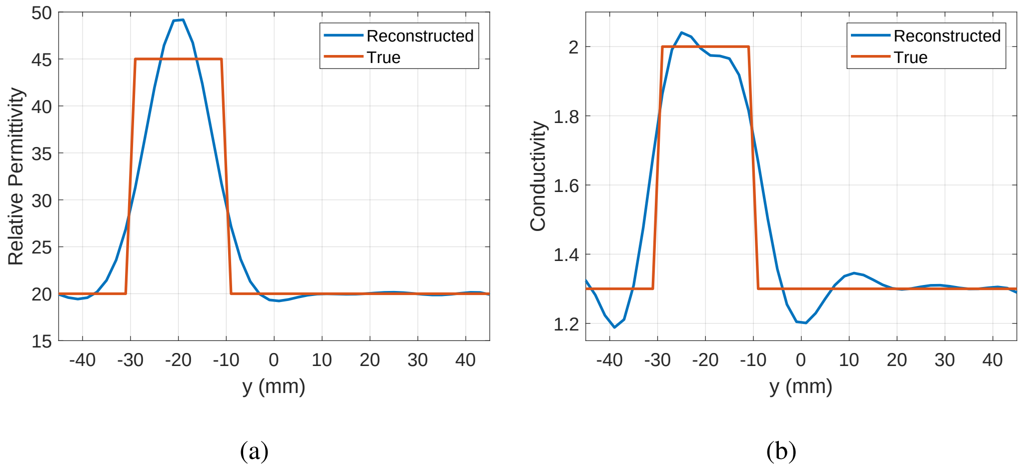

Figure 2.18: The reconstructed (a) permittivity and (b) conductivity values along $x = 0$ cut

CHAPTER 3

SHEAR WAVE ELASTICITY IMAGING

3.1 Introduction

In shear wave elastography (SWE), an acoustic radiation force is generated inside tissue using ultrasound beams. The applied force induces shear waves which propagate perpendicular to the force direction (See Figure 3.1). By tracking the shear waves, the speed of shear waves are estimated, which is an indicative of the tissue's elasticity; shear waves propagates faster in stiffer tissues.

In the forward problem of shear wave elasticity imaging, an acoustic radiation force is created using a focused ultrasound beam. The applied force can be expressed as [153]

$$F = \frac{2\alpha I}{c} \tag{3.1}$$

where α is the attenuation coefficient, c is the speed of sound in tissue, and I is the acoustic intensity. The applied force causes shear wave generation at a targeted region, and transient shear waves propagate away from the excitation region. While shear waves propagate, the dynamic displacement in the target region is calculated.

In the inverse problem of the shear wave imaging, the propagating shear waves, i.e., the dynamic displacement in the tissue, is tracked using ultrasound imaging. However, instead of line-by-line tracking, planes waves are utilized for high speed imaging. After obtaining the dynamic displacement data, time of flight methods can be used for the shear wave speed detection. For a linear, isotropic, elastic materials, the shear wave speed can be expressed as

$$c_s = \sqrt{\frac{\mu}{\rho}} = \sqrt{\frac{\text{YM}}{2(1+\nu)p}}, \tag{3.2}$$

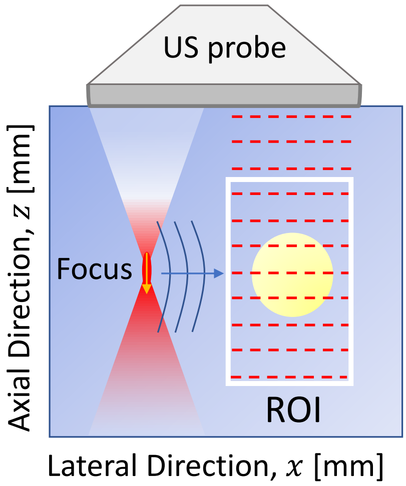

Figure 3.1: Schematic illustration of a shear wave elasticity imaging. Acoustic radiation force is generated at focus the in z-direction. Propagating shear waves are tracked and the shear wave speed is used to estimate the Young's modulus of the tissue.

where μ is the shear modulus, ρ is the density of the medium, YM is the Young's modulus, and ν is Poisson's ratio. For soft tissues, the shear wave speed is approximately 1–10 m/s and the Poisson ratio is taken as $\nu = 0.5$. In this case, the Young's modulus can be expressed as [33]

$$\mathrm{YM} = 3\,\rho\,c_s^2 \tag{3.3}$$

Once the shear wave speed is estimated, the stiffness of the tissues can be found quantitatively using (3.3).

In this chapter, shear wave elasticity imaging simulations have been divided into two parts: the forward problem and the inverse problem. The forward problem was solved using 2D-FDTD and the inverse problem is solved using time-of-flight methods [33].

3.2 Forward Problem

The forward problem of the shear wave elasticity imaging includes the detection of the transient displacement due to applied force. To model the shear wave propagation in the tissue several methods can be used.

As an analytical method, Green's function can be utilized for shear wave simulations. Green's function approach is suitable for modeling both elastic and viscoelastic media, and provides computational speed when compared to numerical methods. However, the shear waves can only be simulated for homogeneous media.

To include heterogenities of the medium, numerical methods are preferred. The finite element method are generally used for shear wave elasticity imaging since it successfully simulates both acoustic radiation force and shear wave propagation. The disadvantage of this method is it is often complicated and the computational efficiency can be low.

In this thesis study, we have used finite difference time domain domain which is easier to implement, and suitable for modeling heterogeneous mediums, and memory requirements are lower when compared to the finite element method.

3.2.1 Mechanical 2D FDTD

The elasticity of a material refers to its ability to return to its original size and shape after being exposed to a deforming force or stress. Assuming low frequency which is valid for shear wave propagation, the biological tissues can be modeled as elastic materials. The elastic wave equation due to applied force can expressed as [154]

$$\rho\frac{\partial^2\overline{u}}{\partial t^2} = \overline{\nabla}\lambda(\overline{\nabla}\cdot\overline{u}) + \overline{\nabla}\mu\cdot[\overline{\nabla}\cdot\overline{u} + (\overline{\nabla}\cdot\overline{u})^T] + (\lambda+2\mu)\overline{\nabla}(\overline{\nabla}\cdot\overline{u}) - \mu\overline{\nabla}\times\overline{\nabla}\times\overline{u}$$

where $\overline{u}$ is the displacement vector, ρ is the density of the medium, and λ and μ are Lamé constants which can be written in terms of Young's modulus (YM) and

Poisson's ratio (ν), and expressed as

$$\lambda = \frac{\nu \text{ YM}}{(1+\nu)(1-2\nu)}$$
$$\mu = \frac{\text{YM}}{2(1+\nu)}$$
$$\nu = \frac{1}{2} - \frac{c_s^2}{2(c_L^2 - c_s^2)}$$

The elastic wave equation includes both shear wave speed c_s and longitudinal (pressure) wave speed c_L (c_p). Therefore, elastic media supports both compressional and shear waves . For soft tissues, the shear wave speeds are smaller by orders of magnitude than the longitudinal (pressure) wave speed. c_s values for soft tissues are typically in the range of 1 to 10 m/s. On the other hand, c_L values for the soft tissues are around 1500 m/s.

When the force is applied to the elastic medium, first, compression waves are generated and propagates in the direction of the force. Then shear waves are generated and they propagate perpendicular to the applied force. The shear wave speed is smaller than the compressional wave speed, but the amplitude of the shear wave displacement is higher than the compression wave displacement [155]. To simulate the wave propagation in elastic medium, the staggered FDTD method formulated in [156, 157] for the velocity-stress equations is used. The 2D velocity-stress equations for spatial components of x and z are given in (3.4) and each variable is explained in Table 3.1

$$\begin{aligned}
\frac{\partial v_x}{\partial t} &= \frac{1}{\rho}\left(\frac{\partial \tau_{xx}}{\partial x} + \frac{\partial \tau_{xz}}{\partial z} + f_x\right) \\
\frac{\partial v_z}{\partial t} &= \frac{1}{\rho}\left(\frac{\partial \tau_{xz}}{\partial x} + \frac{\partial \tau_{zz}}{\partial z} + f_z\right) \\
\frac{\partial \tau_{xx}}{\partial t} &= (\lambda + 2\mu)\frac{\partial v_x}{\partial x} + \lambda\frac{\partial v_z}{\partial z} \\
\frac{\partial \tau_{zz}}{\partial t} &= (\lambda + 2\mu)\frac{\partial v_z}{\partial z} + \lambda\frac{\partial v_x}{\partial x} \\
\frac{\partial \tau_{xz}}{\partial t} &= \mu\left(\frac{\partial v_x}{\partial z} + \frac{\partial v_z}{\partial x}\right)
\end{aligned} \tag{3.4}$$

Time is uniformly sampled at $t = n\Delta t$ for $n = 1, \ldots, N_t$ time steps and interval Δt. Similarly, space is uniformly sampled where indices i, and j, count intervals Δx and Δz to form cartesian coordinates x and z, respectively.

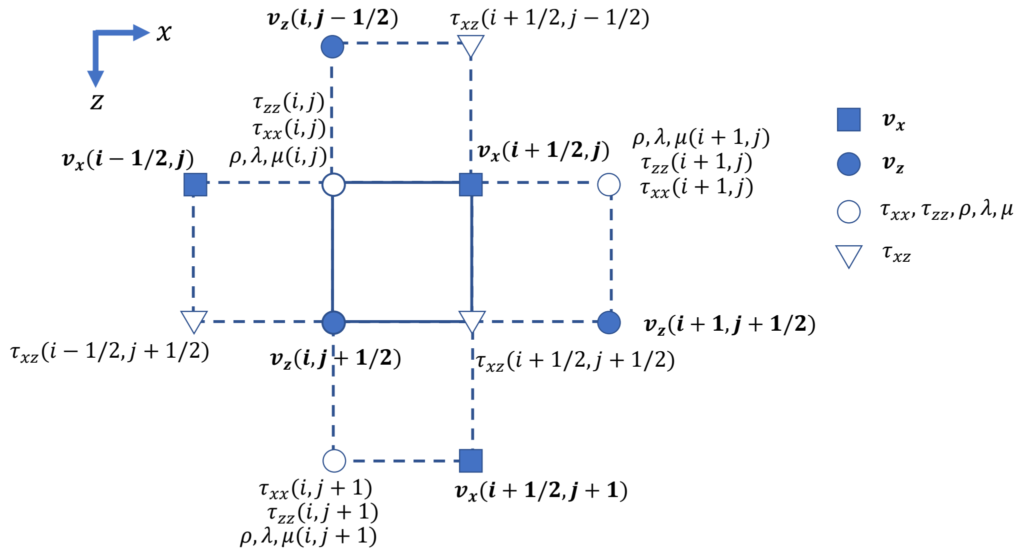

Figure 3.2: Diagram of the staggered grid discretization with the positions of the wavefield variables. Bold symbols denote the velocity components.

Table 3.1: Definiton of the variables used in velocity-stress equations given in 3.4

Variable	Definition
$v_x,\ v_z$	velocity components
$\tau_{xx},\ \tau_{zz},\ \tau_{xz}$	stress components
$f_x,\ f_z$	force components
ρ	density

The equations are discretized according to staggered grid [158] as shown in Figure 3.2. Velocity components are specified at grid positions that are offset by half-intervals from the corresponding stress components. The update equations for the velocity-stress equations are expressed as

$$v_x\big|^{n+1/2}_{i+\frac{1}{2},j} = v_x\big|^{n-1/2}_{i+\frac{1}{2},j} + \frac{\Delta t}{2}\left(\frac{1}{\rho_{i+1,j}} + \frac{1}{\rho_{i,j}}\right)$$
$$\left(\frac{\tau_{xx}\big|^{n}_{i+1,j} - \tau_{xx}\big|^{n}_{i,j}}{\Delta x} + \frac{\tau_{xz}\big|^{n}_{i+1/2,j+1/2} - \tau_{xz}\big|^{n}_{i+1/2,j-1/2}}{\Delta z} + f_x\big|^{n}_{i+1/2,j}\right) \tag{3.5}$$

$$
\begin{aligned}
v_z\big|_{i,j+1/2}^{n+1/2} = v_z\big|_{i,j+1/2}^{n-1/2} + \frac{\Delta t}{2}\left(\frac{1}{\rho_{i,j+1}} + \frac{1}{\rho_{i,j}}\right) \\
\left(\frac{\tau_{xz}\big|_{i+1/2,j+1/2}^{n} - \tau_{xz}\big|_{i-1/2,j+1/2}^{n}}{\Delta x} + \frac{\tau_{zz}\big|_{i,j+1}^{n} - \tau_{zz}\big|_{i,j}^{n}}{\Delta z} + f_z\big|_{i,j+1/2}^{n}\right)
\end{aligned}
\tag{3.6}
$$

$$
\begin{aligned}
\tau_{xx}\big|_{i,j}^{n+1} &= \tau_{xx}\big|_{i,j}^{n} \\
&+ \Delta t\left(\lambda_{i,j} + 2\mu_{i,j}\right)\frac{v_x\big|_{i+1/2,j}^{n+1/2} - v_x\big|_{i-1/2,j}^{n+1/2}}{\Delta x} + \Delta t\lambda_{i,j}\frac{v_z\big|_{i,j+1/2}^{n+1/2} - v_z\big|_{i,j-1/2}^{n+1/2}}{\Delta z}
\end{aligned}
\tag{3.7}
$$

$$
\begin{aligned}
\tau_{zz}\big|_{i,j}^{n+1} &= \tau_{zz}\big|_{i,j}^{n} \\
&+ \Delta t\left(\lambda_{i,j} + 2\mu_{i,j}\right)\frac{v_z\big|_{i,j+1/2}^{n+1/2} - v_z\big|_{i,j-1/2}^{n+1/2}}{\Delta z} + \Delta t\lambda_{i,j}\frac{v_x\big|_{i+1/2,j}^{n+1/2} - v_x\big|_{i-1/2,j}^{n+1/2}}{\Delta x}
\end{aligned}
\tag{3.8}
$$

$$
\begin{aligned}
\tau_{xz}\big|_{i+1/2,j+1/2}^{n+1} = \tau_{xz}\big|_{i+1/2,j+1/2}^{n} \\
+ \frac{\Delta t}{4}\left(\frac{1}{\mu_{i,j}} + \frac{1}{\mu_{i+1,j}} + \frac{1}{\mu_{i,j+1}} + \frac{1}{\mu_{i+1,j+1}}\right) \\
\left[\frac{v_x\big|_{i+1/2,j+1}^{n+1/2} - v_x\big|_{i+1/2,j}^{n+1/2}}{\Delta z} + \frac{v_z\big|_{i+1,j+1/2}^{n+1/2} - v_z\big|_{i,j+1/2}^{n+1/2}}{\Delta x}\right]
\end{aligned}
\tag{3.9}
$$

The FDTD code was implemented in MATLAB [159] and validated with the results obtained by the commercial multiphysics software COMSOL [160] 5.6. In COMSOL simulations, the *Elastic Waves, Time Explicit* interface which is based on a higher order discontinuous Galerkin method with a time-explicit time integration scheme, was utilized [161]. The force was applied only in the z-direction and modeled as Gaussian waveform in both time and space domain. The parameters used in the MATLAB and COMSOL simulations are given in Table 3.2.

$$
f_z(x,z,t) = A(t)\, e^{-x^2/dS} e^{-z^2/dS} \tag{3.10}
$$

$$
A(t) = A_0\, e^{-\left(\frac{t-t_0}{\tau}\right)^2} \tag{3.11}
$$

Table 3.2: Parameters used in FDTD and COMSOL simulations

Parameter	Value
Focus (x_0, z_0)	(0,0) mm
Shear wave speed, c_s	1 m/s
Pressure wave speed, c_p	2 m/s
Young's modulus	3 kPa
Grid size, dx	0.025 mm
Time step, dt	6.25 μs
Source parameter, t_0	1 ms
Source parameter, τ	0.16 ms
Source parameter, dS	2.5×10^{-10}

A homogeneous medium that has YM of 3 kPa was modeled in a square region where the side length is equal to 100 mm. The force was applied at (x, z) = (0,0) mm and the corresponding waves were saved at lateral positions of x = 5 mm, x = 10 mm, and x = 15 mm. The recorded displacement values were normalized for comparison and plotted in Figure 3.3. It can be seen that the results are consistent with each other verifying that the FDTD code is implemented accurately.

To illustrate the propagation of the both pressure and the shear waves, 2D displacement maps for the case where focus at z = 0 mm are shown in Figure 3.4 for different time instances. Displacement data have been normalized by dividing the maximum displacement value at t = 10 ms to help visualize the propagation of the shear wave at different time steps. Notice that pressure waves propagate in the same direction of the applied force (z-direction), whereas shear waves propagate perpendicular (x-direction) to the applied force. When the force is applied, first pressure waves, then shear waves are generated. At the same time instance, the displacement of the pressure waves are two times higher than the shear waves since the speed of the pressure wave ($c_p = 2m/s$) was selected two times higher than the shear wave speed ($c_s = 1m/s$).

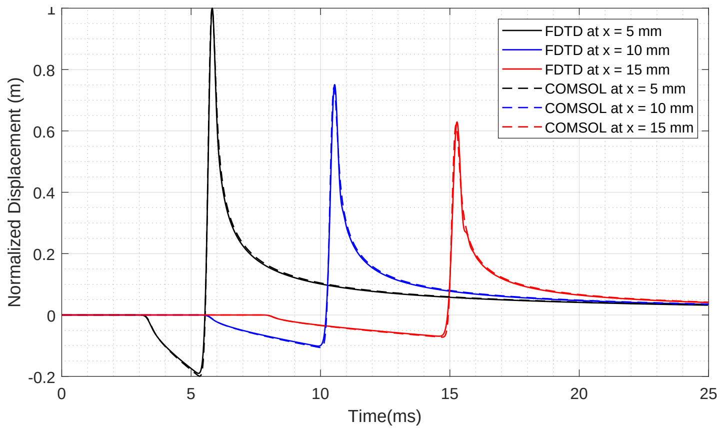

Figure 3.3: The displacement data obtained from FDTD and COMSOL simulations for different lateral positions, x= 5 mm, 10 mm, 15 mm. The focus is at x = 0 mm, z = 0 mm.

3.3 Inverse Problem

In the inverse problem of the shear wave elasticity imaging, the displacement data collected using ultrasound is used to detect the shear wave speed and estimate the YM of the target using the shear wave speed.

The inverse problem procedure can be summarized as follows: The 3D displacement data [axial $\times$ lateral $\times$ time] converted to 2D displacement maps [lateral $\times$time] for each axial position. Then, to eliminate the reflections from the boundaries with different stiffness, directional filters are applied. Using the filtered 2D displacement map and the time-of-flight methods such as time-to-peak or Radon sum transformation [162], the shear wave speed is estimated. Assuming a linear, elastic material for soft tissues, the YM value is given by

$$\text{YM} = 3\,\rho\, c_s^2 \tag{3.12}$$

where ρ is the density of the tissue and c_s is the shear wave speed. The density is typically taken as 1000 kg/m^3 and, the shear wave speed c_s is expressed in m/s. In this case, YM is in units of Pa.

First, the 3D displacement data [axial $\times$ lateral $\times$ time] is converted into 2D displacement maps [lateral $\times$time] for each axial position and expressed as $d(x,t)$.

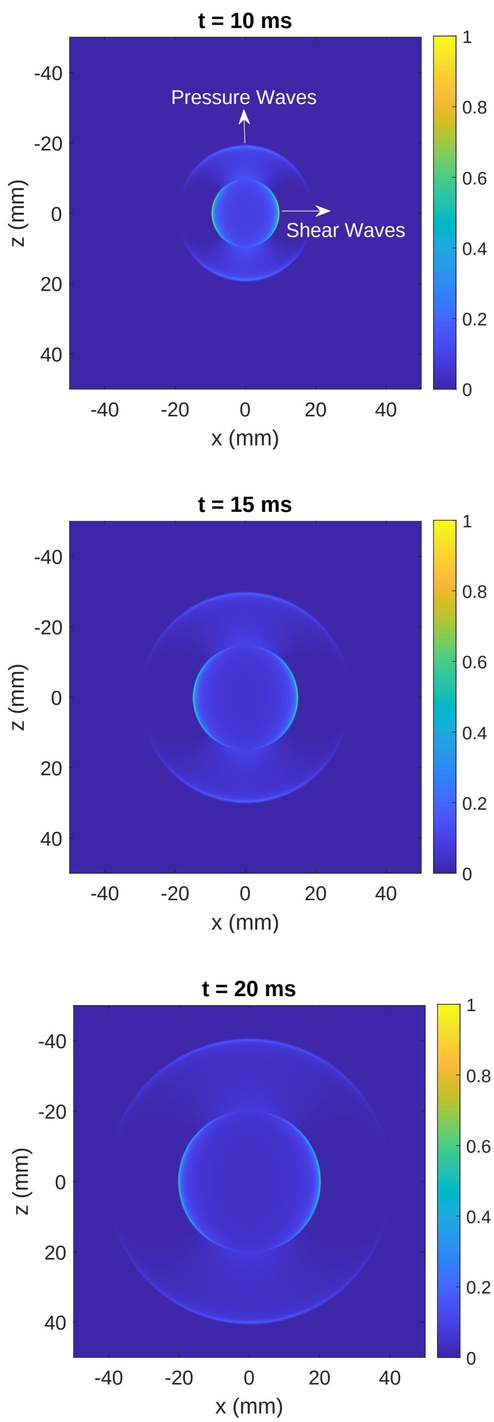

Figure 3.4: Simulated displacement data at different time instances: 10 ms, 15 ms, 20 ms. The focus is at $x = 0$ mm, $z = 0$ mm, and the force is applied at the z-direction. To visualize the propagation of the waves at different time steps, displacement data have been normalized by dividing the maximum displacement value at t = 10 ms.

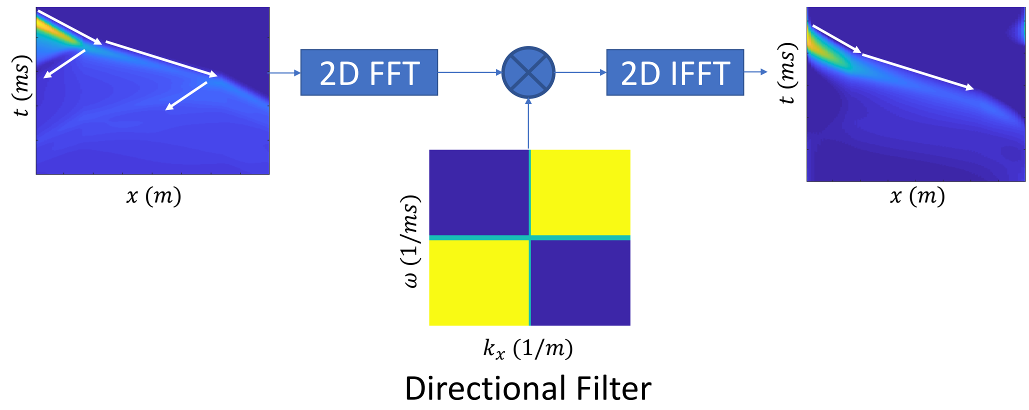

Figure 3.5: The schematic shows the directional filtering process. The displacement data is transformed into frequency domain and only the rightward propagation waves ($[k_x, w > 0]$ and $[k_x, w < 0]$) are selected using the directional filter. Then, by taking the inverse Fourier transform, the filtered displacement data is obtained. The wave propagation and the reflections are shown with white arrows.

Then, the 2D displacement data is transformed to the frequency (spectral) domain data (k_x, ω) and only the shear waves propagating through the desired direction (rightward or leftward) is selected [163]. For a propagating wave, the k-space domain is separated into four quadrants and the forward propagating waves corresponding the first and third quadrants of the spectrum are selected. Using these quadrants and multiplying the frequency domain displacement data the reverse propagating waves are eliminated. Then, using the inverse Fourier transform, the displacement data in space-time domain is obtained. The process for the directional filtering is summarized in Figure 3.5.

After obtaining filtered 2D displacement maps, time-of-flight methods can be used for the shear wave speed estimation. One of the most popular time-of-flight method is called as lateral time-to-peak (TTP) algorithm [33]. In this algorithm, the shear waves are tracked along the lateral direction and it is assumed that the peak of the shear wave displacement propagates at shear wave speed. For each lateral position, the arrival time of the shear wave peak is determined and expressed as a function of lateral position. Then, using the linear regression between the lateral locations and the shear wave arrival times, the shear wave speed is calculated from the slope. Another time-of-flight method, which is called as time-to-peak-slope can also be used for shear wave estimation. In this method, the displacement versus time data is differentiated in time domain, and the peak of the velocity data is tracked at lateral positions. Similar to the TTP algorithm, the shear wave speed is obtained using linear regression.

Once the shear wave speed is determined, the YM value can be obtained using (3.12).

3.4 Test of the Algorithm

In this section, a simple 2D target has been simulated and the reconstruction results are provided. For the imaging scenario, the Young's moduli of the background medium and the target were selected as 15 kPa and 60 kPa, respectively. Target is modeled as a cylindrical inclusion with a diameter of 10 mm and centered at $x = 10$ mm, z = 0 mm. The total size of the imaging domain was 60 mm $\times$ 60 mm. The ultrasound beam was modeled as a Gaussian source and focused from -6 mm to 6 mm with 2 mm steps. The Gaussian force distribution can be expressed as

$$f(x, z, t) = A(t)e^{-x^2/dS}e^{-(z-z_f)^2/dS} \tag{3.13}$$

where, $A(t)$ is the time dependent force amplitude, and dS is the beamwidth parameter, and z_f is the focus point in the z-direction. The amplitude term $A(t)$ can be set empirically to obtain a displacement value of 20 μm which is a typical displacement value for shear wave simulations [33, 162]. The displacements around the focus region were tracked along lateral positions of x = [2, 16] mm. The imaging scenario is illustrated in Figure 3.6. To decrease the computational burden and observe pure shear wave propagation in the simulations, the normal stress components τ_{xx} and τ_{zz} were omitted from the formulations [157].

In addition, the displacement values at z = -6 mm which corresponds to background medium, and z = 0 mm which includes the target are shown in Figure 3.7. When the shear waves enter the target region (target is at the lateral distance of 5 mm to 15 mm), the shear wave speed increases due to the high stiffness (See Figure 3.7 - (b)). In addition, the shear waveform is distorted due to reflections from the boundary between the background and the target.

After obtaining 3D displacement maps for each focus position, the displacement maps

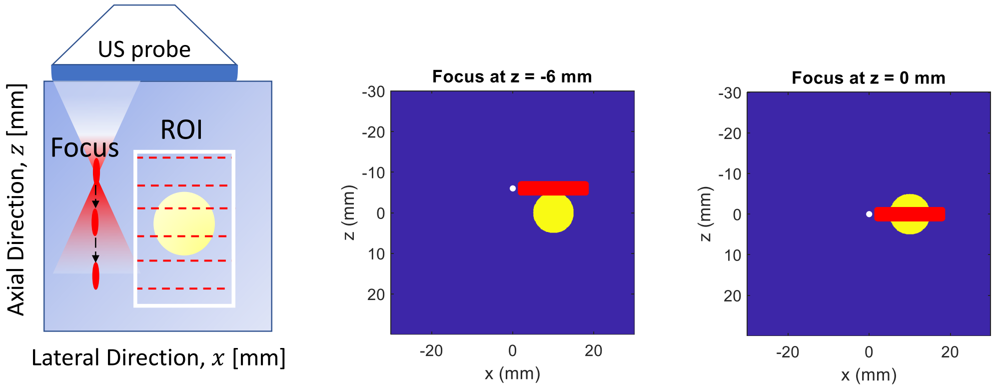

Figure 3.6: Illustration of the shear wave elasticity imaging scenario. The ultrasound beam is focused at different axial depths and the propagating shear waves are tracked inside the region of interest. Tracking locations are highlighted with red color. The white dot shows the position of the focused beam.

were converted into 2D and directional filtering is applied as shown in Figure 3.5. Then, the time-to-peak-slope algorithm was used for the shear wave tracking. The lateral position versus time graphics are given for z = -6 mm and z = 0 mm in Figure 3.8. Note that, the slope of the graphs correspond to the shear wave speed. For Figure 3.8 - (b), as the shear wave enters the target region, the slope increases due to the higher stiffness, and when the shear waves exit the target region the slope decreases. On the other hand, nearly constant slope is observed for Figure 3.8 - (a) since the shear wave propagates at the background medium. However, around t = 8 ms, the reflections from the tumor edges start to interfere with the rightward propagating waves. This interference changes the slope around t = 8 ms and results in artifacts in the reconstructed YM images.

Using TTPS vs lateral position information for each focus position, linear regression was performed with a kernel size of 0.4 mm and the slope, i.e., shear wave speed was determined. In cases where linear regression results in negative slope values, these values are omitted for the accuracy of the estimation. After all the shear wave speeds were obtained for each focus position, the calculated speed values were converted to YM values using (3.12). The obtained Young's moduli were smoothed using a 3 $\times$ 3 median filter and interpolated using $imresize$ function of MATLAB which uses

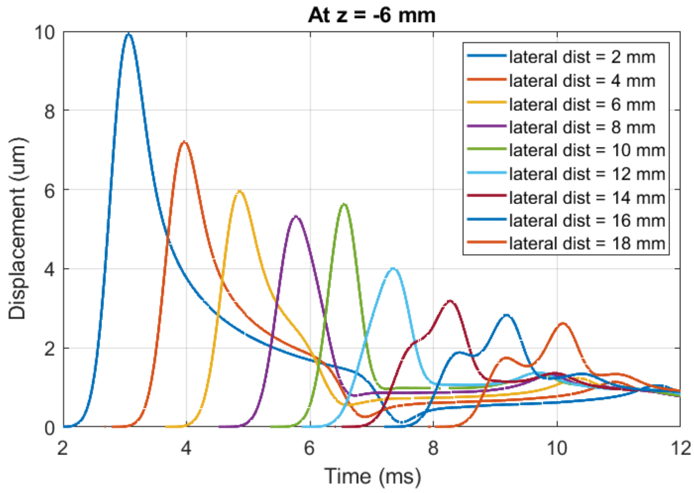

(a)

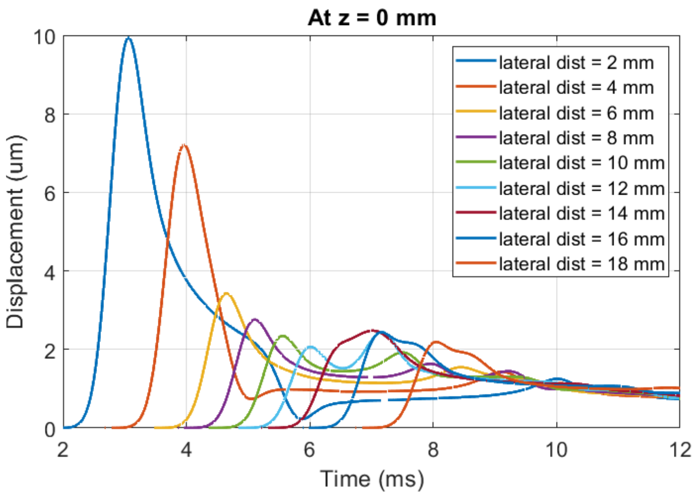

(b)

Figure 3.7: Simulated displacement data resulting from excitations centered at (a) z = -6 mm and (b) 0 mm. Plots show displacement versus time profiles for lateral positions of [2:2:18] mm.

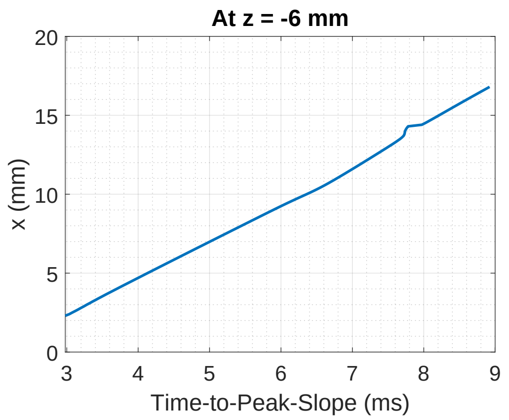

(a)

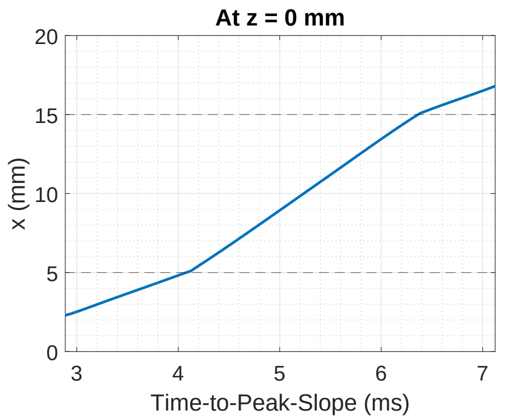

(b)

Figure 3.8: Time-to-peak-slope versus lateral positions for the cases when focus is at (a) z = -6 mm and (b) 0 mm. For each displacement, the time at which the velocity data (derivative of the displacement data) arrives the lateral position is plotted. The slope of the graphs correspond to the shear wave speed. For case (b), the tumor positions are represented with dashed line. Notice that, the shear wave speed (slope) increases at the target region.

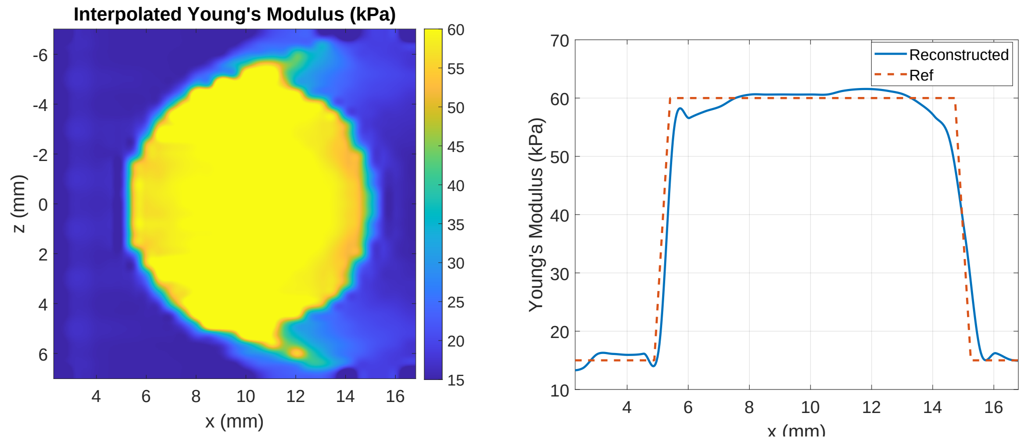

(a) (b)

Figure 3.9: The reconstruction results for the shear wave elasticity imaging. (a) Reconstructed Young's modulus values for a background medium with 15 kPa and target with a 60 kPa stiffness. (b) Comparison of the reconstruction results with the reference values along z = 0 mm cut.

bicubic interpolation. The resulting shear wave image is shown in Figure 3.9-(a) . In addition, the reconstruction results were compared with the reference values along z = 0 mm line and shown in Figure 3.9-(b).

The results indicate that the Young's modulus values were reconstructed quantitatively for the imaged region. Some artifacts were observed in the reconstructed image due to the reflections from the edges of the tumor. To eliminate these artifacts, the kernel size can be modified, however, the kernel size affects the reconstruction results significantly [162]. Small kernel sizes provide better spatial resolution at the expense of accuracy. On the other hand, larger kernel sizes decrease the error at the expense of spatial resolution. Therefore, the optimal kernel size requires a compromise between the accuracy and the spatial resolution. Another method to eliminate artifacts is to apply trajectory based methods for the shear wave speed estimation, such as Radon sum algorithm [162]. In this algorithm, the 2D displacement maps are obtained for each focus position and the optimal trajectory is found using Radon sums for the 2D displacement data. This algorithm was used for the measurement reconstructions and details are given in the Chapter 5.

CHAPTER 4

TISSUE MIMICKING BREAST PHANTOM DEVELOPMENT

4.1 Introduction

To conduct experiments on both microwave imaging and shear wave imaging, tissue-mimicking materials called as phantoms which have the electrical and mechanical parameters similar to the realistic tissues were developed. These phantoms enable the evaluation of imaging system performance for different imaging scenarios.

In previous studies, tissue mimicking materials which have similar dielectric properties of breast have been prepared using agar mixtures [164], oil-in-gelatin mixtures [164–166], and 3D-printed materials [167, 168]. Similarly, to mimic the mechanical properties of tissues, oil-gelatin mixtures [165], milk-gelatin mixtures [169], and agar-silicon-gelatin mixtures [170] were prepared. A review of the literature on breast tissue phantoms can be found in [1, 171]. Some drawbacks of the previously developed phantoms include the use of toxic ingredients (e.g., formaldehyde) that require specific laboratory equipment, the high cost of some ingredients, intensive preparation procedures, and the need for sophisticated and expensive equipment. Additionally, the variety of phantoms for categorizing breast tissues was limited.

Recently, in 2022, oil-in-gelatin phantoms were proposed in [1], which only involve low-cost, easy-to-handle, and safe materials capable of mimicking both the dielectric and mechanical properties of breast tissues. The materials used include sunflower oil, deionized water, dishwashing liquid, and gelatin. In addition, a large variety of phantoms representing all categories of human breast tissues were developed using these ingredients. In this thesis study, the phantoms have been developed according to the recipes given in [1].

4.2 Phantom Preparation Procedure

For the experimental studies, two breast phantoms were developed to mimic both the dielectric and mechanical properties of tissues. These phantoms are named "Phantom – 1 : microwave imaging phantom" and "Phantom – 2 : multi-modal imaging phantom" . Both phantoms contain medium-density, high-density, and malignant breast tissues. Phantom-1 was developed for microwave imaging only, without considering elasticity differences, whereas Phantom-2 was developed for multi-modal imaging (i.e. microwave and shear wave elasticity imaging). For both phantoms, high-density breast tissue was chosen to represent fibroglandular tissue, creating a challenging scenario for microwave imaging. The properties of the developed phantoms are described in the next section. Since the preparation procedure is the same for both phantoms, the procedure is described here first.

The materials used for the phantom development include gelatin, deionized water, safflower oil, and dish-washing liquid. As a gelatine material, gelatine 200 Bloom, food grade, was used. An analytical balance was used for measuring the gelatin amounts. The preparation procedure is as follows:

1. Gelatin and deionized water are mixed in a glass beaker and heated to 85 °C. To prevent water evaporation, the beaker is covered with aluminum foil.
2. The heated gelatin-water mixture is allowed to cool to 65 °C.
3. Safflower oil is heated to 65 °C.
4. When both mixtures are at 65 °C, dish-washing liquid is added, and the mixture is stirred with a magnetic stirrer until it cools to 50 °C.
5. The mixture is then allowed to polymerize for about 3.5 hours at room temperature (approximately 25 °C).

During phantom development process, we had some observations. For step-1, using double boiler resulted in a more homogeneous and clear solution. For step-4, adding a portion of the dish-washing liquid slowly to the gelatin-water mixture, followed by gradually adding the oil, made dissolving easier than mixing the oil and dish-washing liquid all at once. When the oil dissolves, the mixture should form an emulsion, appearing as a uniform, dense, pale liquid.

As an example, the ingredients used for the Phantom – 2 development are shown in Figure 4.1. From left to right, the mixtures were prepared for breast, fibroglandular, and tumor phantoms. The glass beakers in the back contain gelatin- deionized water mixtures, while the beakers in the front contain oil. The figure shows that, the stiffest tissue, i.e., the tumor phantom, contains the lowest amount of oil. In addition, due to the lower relative permittivity of oil ($\varepsilon_r \sim 3$ [1]), as the amount of oil increases, the overall permittivity decreases. Therefore, the breast phantom has the highest amount of oil. Figure 4.1 also shows the final mixture for the breast phantom, which has a uniform, creamy texture.

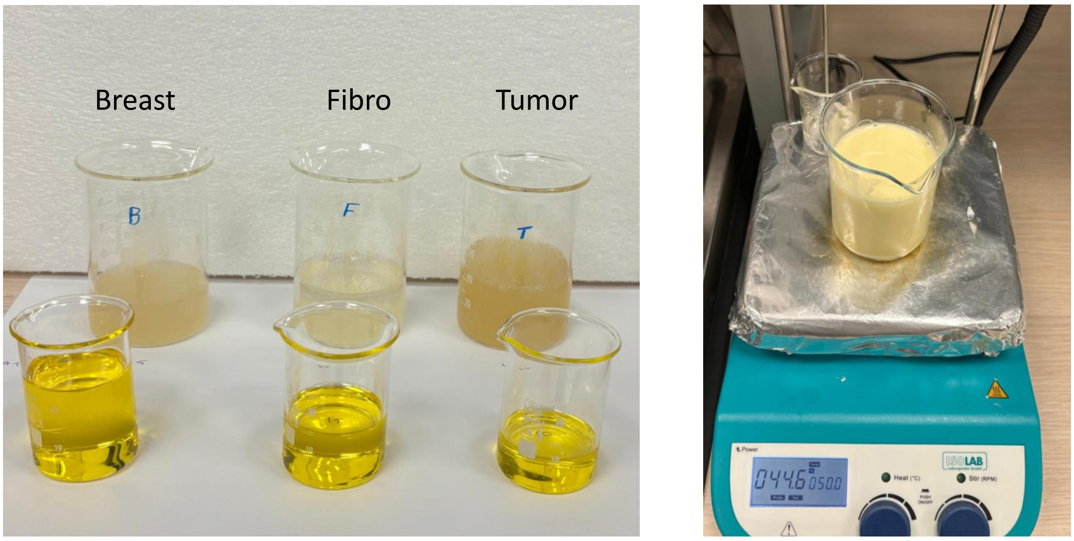

Figure 4.1: The ingredients used for the Phantom-2 development and the final mixture for the breast phantom. From left to right: Breast, fibroglandular, and tumor phantom mixtures. The glass beakers in the back contain gelatin-deionized water mixtures, while the beakers in the front contain oil.

4.3 Breast Phantoms for Imaging

4.3.1 Phantom – 1 : Microwave Imaging Phantom

For the first phantom, a phantom was developed involving medium-density breast tissue, high-density breast tissue, and malignant tissue, without considering elasticity differences. The terminology for the tissue phantoms follows the naming convention in [1] and has been simplified here. For example, the third medium-density breast tissue mixture G9.55O50 is abbreviated as Med3G9, and the second malignant tissue mixture G16O20 is abbreviated as Mali2G16. The ingredients for Phantom – 1 are listed in the Table 4.1.

Table 4.1: The ingredients for the developed Phantom – 1. D-Water is deionized water, and DL is the dishwashing liquid.

Mimicked tissue	D-water (ml)	Gelatin (g)	Oil (ml)	DL (ml)
Breast Med3G9	68	13	68	3.8
Fibroglandular High2G9	68	10	34	3.8
Tumor Mali2G16	68	13.6	17	3.8

Phantom – 1 contains medium-density breast tissue Med3G9, high-density breast tissue High2G9, and malignant tissue Mali2G16. The high-density breast tissue represents fibroglandular tissue and is referred to as the fibroglandular phantom, while the medium-density breast tissue is simply called the breast phantom for simplicity. Therefore, there are three types of phantoms: breast, fibroglandular, and malignant tissue phantoms. The fibroglandular and malignant tissue phantoms were prepared and poured into 20-mm diameter syringes.

While preparing Phantom – 1, the breast tissue phantom mixture was first poured into an 85 mm diameter mold to a height of 4 cm. Then, the tumor and fibroglandular inclusions were manually fixed in place, and the mold was filled with breast tissue phantom. Due to the manual placement, there were some shifts when additional breast tissue was poured over the fixed inclusions. The prepared phantom is shown in Figure 4.2, with tumor and fibroglandular inclusions indicated by dashed lines.

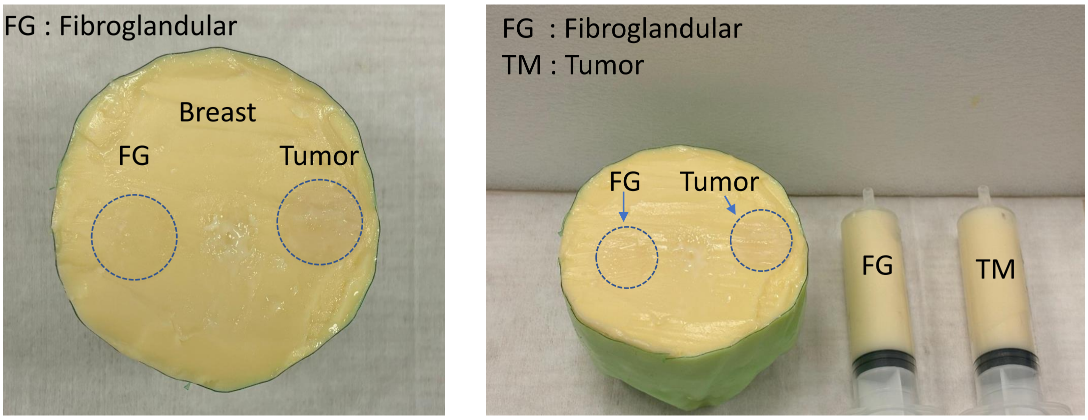

Figure 4.2: The photographs of the microwave imaging phantom (Phantom – 1). Tumor and fibroglandular inclusions are indicated with dashed lines and arrow. The syringes show the tumor and fibroglandular inclusions before they were inserted inside the Phantom – 1.

4.4 Phantom - 2 : Multi-Modal Imaging Phantom

For the second phantom, a phantom which includes a medium density breast tissue, a high density breast tissue, and a malignant tissue was developed. Phantom-2 mimics both the dielectric and mechanical properties of tissues and developed for multi-modal imaging (i.e. microwave and shear wave elasticity imaging) . Phantom preparation procedure similar to the first phantom was applied. The dielectric and mechanical properties of the phantom was modified considering two factors: first, the dielectric properties of the fibroglandular and tumor inclusions were selected to decrease the dielectric contrast between them, and, second, the elastic contrast between the tumor and breast, and between tumor and fibroglandular tissue, was increased. The decrease in the dielectric contrast between the tumor and fibroglandular tissue represents a difficult case for microwave imaging, where the tumor and the healthy fibroglandular tissue may not be easily identified due to their similar permittivity and conductivity values. On the other hand, the increase in the stiffness of the tumor helps in its identification using shear wave elasticity imaging.

Table 4.2: The ingredients for the developed Phantom-2. D-Water is deionized water, and DL is the dishwashing liquid. * : High1G6 recipe given in [1] was slightly changed. The amount of oil was decreased from 34 ml to 29 ml.

Mimicked tissue	D-Water (ml)	Gelatin (g)	Oil (ml)	DL (ml)
Breast Med2G7	68	10	68	3.8
Fibroglandular High1G6*	68	6.8	29*	3.8
Tumor Mali3G21	68	18	17	3.8

The breast and tumor phantoms were developed according to a recipe given in [1]. Mixture Med2G7 and Mali3G21 were used for breast and tumor phantom preparation, respectively. However, for the high density fibroglandular tissue, the recipe of the High1G6 mixture was modified slightly. At the original recipe, the amount of the deionized water, gelatin and oil was 68 ml, 6.8 g, and 34 ml. To increase the permittivity and conductivity values of the fibroglandular tissue, thereby decreasing the contrast between the tumor tissue, the amount of oil decreased from 34 ml to 29 ml. The volume percentage of gelatin and oil was changed from 6.6% to 7.0% and 33.3% to 29.9%, respectively. The ingredients for Phantom – 2 are listed in the Table 4.2.

The fibroglandular and malignant tissue phantoms were prepared and poured into 20-mm diameter syringes. For visualization, these inclusion were colored using food coloring gel. In the first phantom, the tumor and fibroglandular inclusions were manually fixed, which caused them to shift. For this phantom, a mold was created to hold them in place. After placing the tumor and fibroglandular tissues with this mold, the rest of the phantom was filled with breast tissue phantom. Phantom holders were used while filling the phantoms, and the top holders were removed at the end. The construction steps and the completed form of the Phantom – 2 are shown in Figure 4.3.

4.4.1 Measurements of the Developed Phantoms

Both dielectric and mechanical parameters of the phantoms were measured. For dielectric measurements, the virtual line method, which utilizes an open-ended coaxial

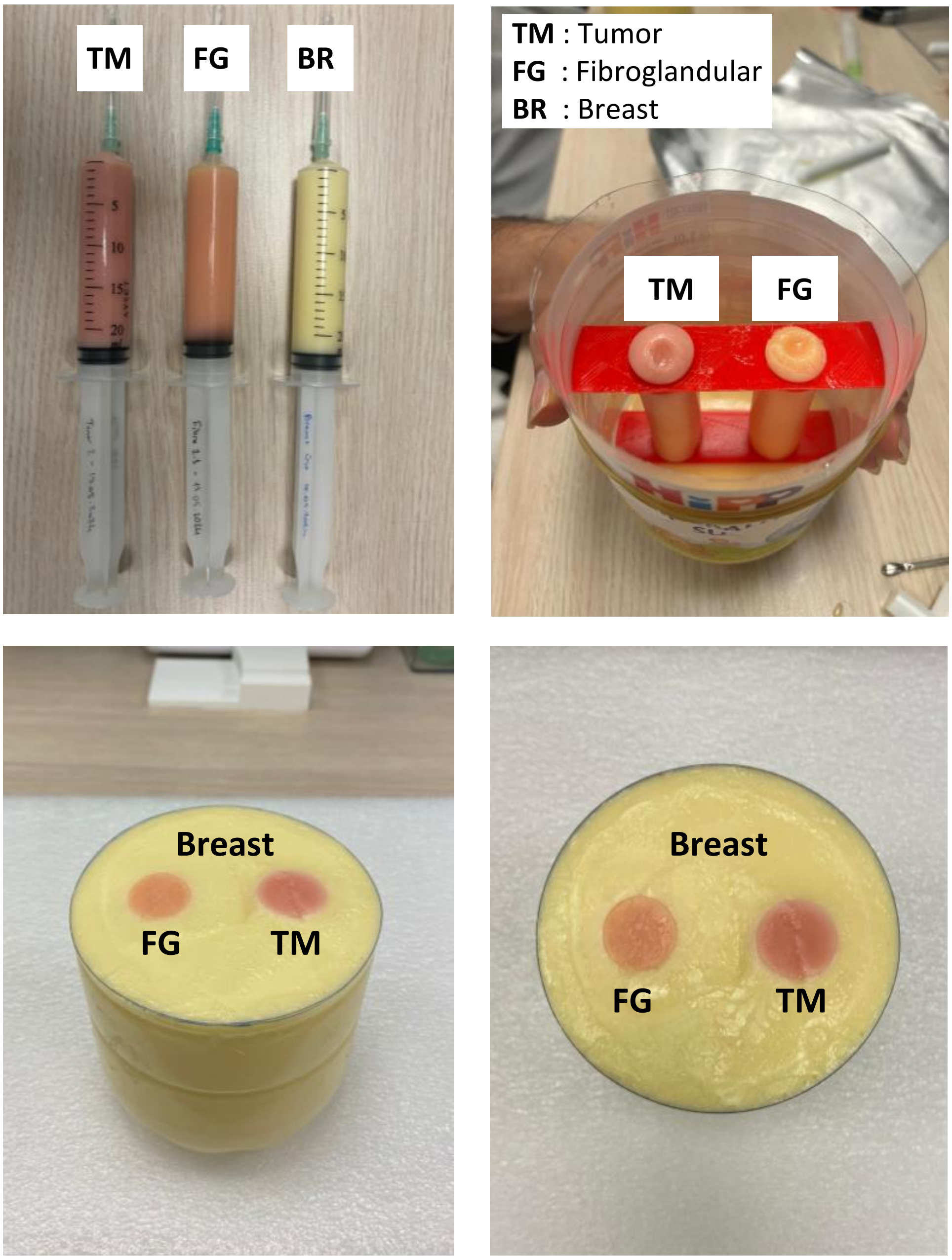

Figure 4.3: The construction steps and the completed form of the multi-modal imaging phantom (Phantom – 2). The syringes show the tumor and fibroglandular inclusions before they were inserted inside the Phantom – 2. Tumor and fibroglandular inclusions are colored using food coloring gel, and fixed inside the phantom mold. Phantom holders were used while filling the phantoms, and the top holders were removed at the end.

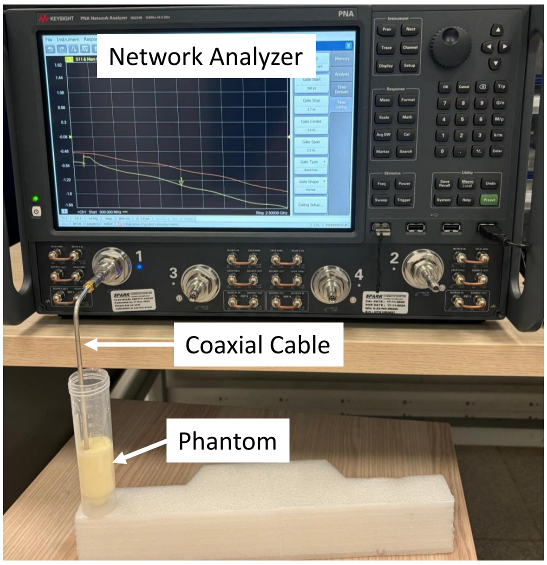

Figure 4.4: The system set-up for the dielectric measurements. Using open-ended coaxial line and network analyzer, reflection coefficients were measured.

Table 4.3: Measurement results for the dielectric properties of the microwave imaging phantom (Phantom – 1) at 1.5 GHz. The reference values are taken from [1].

	Relative Permittivity		Conductivity (S/m)	
	Measurement	Reference	Measurement	Reference
Breast Med3G9	22.8	24	0.27	0.43
Fibroglandular High2G9	40.2	39	0.52	0.64
Tumor Mali2G16	47.2	46	0.70	0.76

line, was used. The reflection coefficients for two calibration materials, i.e., water and oil, and the material under test were measured using a network analyzer. Then, the permittivity and conductivity values were obtained using the algorithm developed by Top et al. [172] and later improved in [173]. The details of the measurement procedure and the algorithm can be found in [173]. The experimental setup used to measure the dielectric properties of the phantom is shown in Figure 4.4, and the obtained results were tabulated in Table 4.3 along with reference values. The results showed that the phantoms were developed accurately and the permittivity and conductivity values are close to the reference values.

Table 4.4: Measurement results for the dielectric properties of the multimodel imaging phantom (Phantom – 2) at 1.3 GHz. The reference values are taken from [1]. * : High1G6 recipe given in [1] was slightly changed. The amount of oil was decreased from 34 ml to 29 ml.

	Permittivity		Conductivity (S/m)	
	Measurement	Ref [1]	Measurement	Ref [1]
Breast Med2G7	24.64	23.85	0.21	0.25
Fibroglandular High1G6*	41.58	38.27	0.34	0.42
Tumor Mali3G21	44.8	48.62	0.60	0.60

For the elastic properties measurement, only multi-modal imaging phantom (Phantom – 2) materials (Med2G7, High1G6, Mali3G21) was measured.

Elasticity measurement methods can be simply classified as dynamic and static measurements. In dynamic elasticity measurement, a time-varying force is applied to the material, whereas, in static measurements, constant or slowly varying force is applied to measure resulting deformation [1]. The studies in [1] showed that elasticity values changed depending on the applied pre-load and test speed used during measurement. In addition, in our previous studies, both static and dynamic methods were used for elasticity measurements [172]. It was observed that the dynamic method's performance was questionable for soft tissues, while the static method gave higher values than reference for hard tissues. Therefore, it was decided to apply the shear wave elasticity imaging for elasticity measurements.

The measurements were performed using The Verasonics Vantage Ultrasound Research System (Verasonics, Inc., Kirkland,WA, USA) at ASELSAN A.S. and L11-5V ultrasound probe with settings given in Table 5.4, and with focus depth of $\sim$ 10 mm. To verify the accuracy of the method, commercially available CIRS Model 040GSE multi-purpose, multi-tissue ultrasound phantom, which is commonly used by the ultrasound community for reliable testing and imaging performance [174] was used. The details for the shear wave elasticity imaging setup are given in the next chapter, including measurement system, imaging system parameters, used methodology, data acquisition and processing steps. For brevity, these steps are not repeated in here.

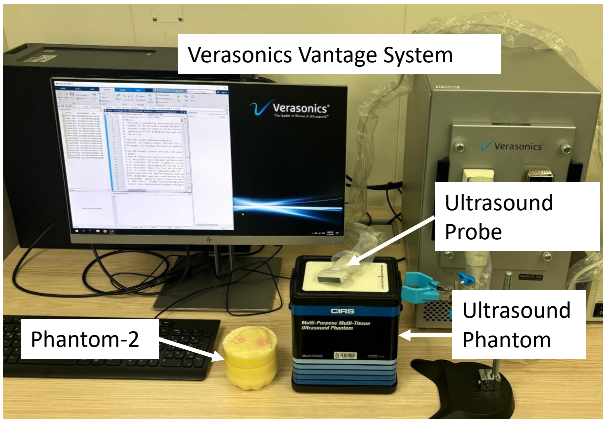

Figure 4.5: The system set-up for the elasticity measurements. Using Verasonics Vantage ultrasound research system and CIRS ultrasound phantom, shear wave elasticity measurements were performed. Then, homogeneous phantoms inside syringes were measured using the same imaging methodology.

Table 4.5: Measurement results for the elastic properties of the Phantom – 2. The reference values are taken from [1]. * : High1G6 recipe given in [1] was slightly changed. The amount of oil was decreased from 34 ml to 29 ml.

	Young's Modulus (kPa)	
	Measurement	Reference [1]
Breast Med2G7	9.80	8.60 ± 3.69
Fibroglandular High1G6*	8.50	8.00 ± 2.27
Tumor Mali3G21	48.50	32.6 ± 27.34

For elasticity measurements, the homogeneous region of the CIRS phantom was selected to eliminate errors due to reflections. The Young's modulus value of the CIRS phantom was found to be 22 kPa, close to the reference value of 20 kPa, confirming that the measurements were conducted properly. Using the same measurement methodology, elasticity measurements were also taken for the breast (Med2G7), fibroglandular (High1G6), tumor(Mali3G21) phantoms in syringe tubes, which are in homogeneous form. The obtained results were tabulated in Table 4.5 along with reference values. The results showed that the phantoms were developed accurately and the Young's modulus values are close to the reference values.

In addition, it was observed that the elasticity value of the phantom changes over days due to the ongoing gelatin-water cross-linking process. For the fibroglandular (High1G6) and tumor (Mali3G21) tissues, Young's modulus values measured from homogeneous tubes 8 hours after phantom preparation were 5 kPa and 34 kPa, respectively, while measurements taken the next day were 9.8 kPa and 48.5 kPa. Therefore, when performing shear wave elasticity imaging, the day the phantom was made and measured should be taken into account.

In conclusion, both the dielectric and mechanical properties of the phantoms were measured. Since the obtained values were appropriate for the imaging scenarios, the experiments described in the next chapter were carried out.

CHAPTER 5

EXPERIMENTAL STUDY

In this section, conducted experimental studies are grouped into two: Microwave imaging experiments and shear wave elasticity imaging experiments. The experimental setups for both microwave and shear wave elasticity imaging are presented. Measurements were conducted using the developed phantoms in Chapter 4. The image reconstruction results for microwave imaging and detected Young's modulus values for the shear wave elasticity imaging are presented.

The output image of the microwave imaging, i.e., quantitative map of dielectric properties, was used as prior information and provided the region of interest for the shear wave elasticity imaging. Then, shear wave elasticity imaging was applied directly to the suspicious regions, resulting in quantitative identification of malignant and healthy tissues.

5.1 Experimental Study for Microwave Imaging

5.1.1 Experimental Setup for Microwave Imaging

For the experimental studies, a microwave imaging system similar to the that of Dartmouth College [54, 175] and Chalmers University [93, 176] was developed. In this measurement system, all antennas act as both transmitter and receivers. While one of the antennas was transmitting, the other antennas functioned as receivers.

In microwave imaging setup, monopole antennas with a length of 12 cm were used. The outer conductor of the antenna has been removed 3 cm from the top. Monopole antenna was preferred due to several reasons. First, these types of antennas have already been used and have shown feasibility for microwave imaging [177]. Secondly, when the antennas are inserted into the lossy coupling liquid, antennas do not require a ground plane and operate in a wide impedance bandwidth. Thirdly, monopole antennas can be modelled as point sources in 2D simulations. Since microwave imaging requires forward problem solution for each antenna at each iteration step, 2D models were preferred for computational efficiency. Monopole antennas align with the 2D imaging assumptions. For monopole antenna design, we have used Huber Suhner Sucoform 141 cable, which has an outer diameter of 3.58 mm. 16 antennas of equal length were produced at ASELSAN REWIS. In our imaging system, these antennas were placed in a uniform circular arrangement in a diameter of 160 mm.

In microwave imaging setups, to maximize the energy that couples into the imaged object, a coupling liquid, whose permittivity value is close to the imaged object, is generally utilized [146]. The coupling liquid provides a matching between the imaged object and the antennas, as opposed to air coupled system in which reflections occur from the object and air interface. The coupling liquid is generally selected as a lossy liquid which enables the elimination of the multipath signals and surface waves. In addition, the lossy nature of the coupling medium causes monopole antennas to have a wide impedance bandwidth, and reduces the coupling between the neighbouring antennas. On the other hand, lossy nature of the coupling liquid introduces power loss especially for the antenna farthest from the transmitter. In this thesis, glycerin-water mixture, which is widely preferred for microwave imaging [146], was used as coupling liquid. A mixture of 80% glycerin and 20% water was used since it has a permittivity value ($\varepsilon_r^{bck} = 20.9, \sigma^{bck} = 1.15$@ 1.3 GHz) close to the developed breast phantom ($\varepsilon_r^{breast} = 24.6, \sigma^{breast} = 0.21$@ 1.3 GHz).

In microwave imaging, for the measurement of the transmitted and received signals, multi-port vector network analyzers or network analyzers with a switching matrix are generally used [176, 178] . In this thesis study, a 16-port Rohde & Schwarz ZNBT 20 (Rohde & Schwarz GmbH, Germany) vector network analyzer was used. This device can measure all return losses and coupling between each port, and the results are expressed in S-matrix with $N \times N$ elements, where N is the number of ports. Since it does not require a switching, the switching losses are low and the measurements can be performed quickly. The measurements were carried out using network analyzer with 0 dBm output power, 10 Hz IF bandwidth and over 20 samples. Generally, single frequency measurements were taken to increase the signal-to-noise ratio and decrease the overall measurement duration.

The imaging setup is shown in Figure 5.1. The return loss of the antennas inside the coupling liquid for a homogeneous background is given in Figure 5.2. It is observed that antennas have S_{11} values less than -10 dB at the operating frequencies of 1.3 GHz and 1.5 GHz. In addition to return loss values, coupling values between the antennas when antenna 1 was transmitting is given in Figure 5.3. For the neighbouring antennas, i.e, antenna #15 - #16, and antenna #2 - #3, the coupling is nearly -30 dB and -50 dB at 1.3 GHz. For the farthest antenna to the transmitter, i.e. antenna #9, the S_{91} = -68.2 dB at 1.3 GHz. The decrease in the received signal is caused by the lossy coupling liquid and the power loss increases as the frequency increases.

After performing the measurements using the network analyzer, the S-parameters need to be calibrated to obtain the E-field values to be used in the reconstruction [106, 177]. The calibration procedure can be summarized as follows. First, S-parameter measurements are taken without any object for a homogeneous background, whose electrical parameters are known before. These measurements are denoted as S^{bck}_{meas}. Second, using the electrical parameters of the homogeneous background, electric field values are calculated by solving the forward problem. The computed electric field values are denoted as E^{bck}_{calc}. Third, the S-parameter measurement is conducted when the object is present in the imaging domain. The measurement data is denoted as S^{obj}_{meas}. Then, the calibrated electric field values for the measured object E^{obj}_{meas} can be obtained using the following equation [106]:

$$E^{obj}_{meas} = \frac{S^{obj}_{meas}}{S^{bck}_{meas}} E^{bck}_{calc} \tag{5.1}$$

Note that this calibration technique accounts for the free space loss factor, magnitude and phase errors due to cables, connectors, and antenna location inaccuracies, since both background and object measurements share the same properties. This technique is effective especially in a lossy medium and for imaging scenarios where the object is away from the antennas so as not to affect the antenna radiation [177]. The measured S-parameters were calibrated using the procedure above and used as E_{meas} in the reconstruction algorithm.

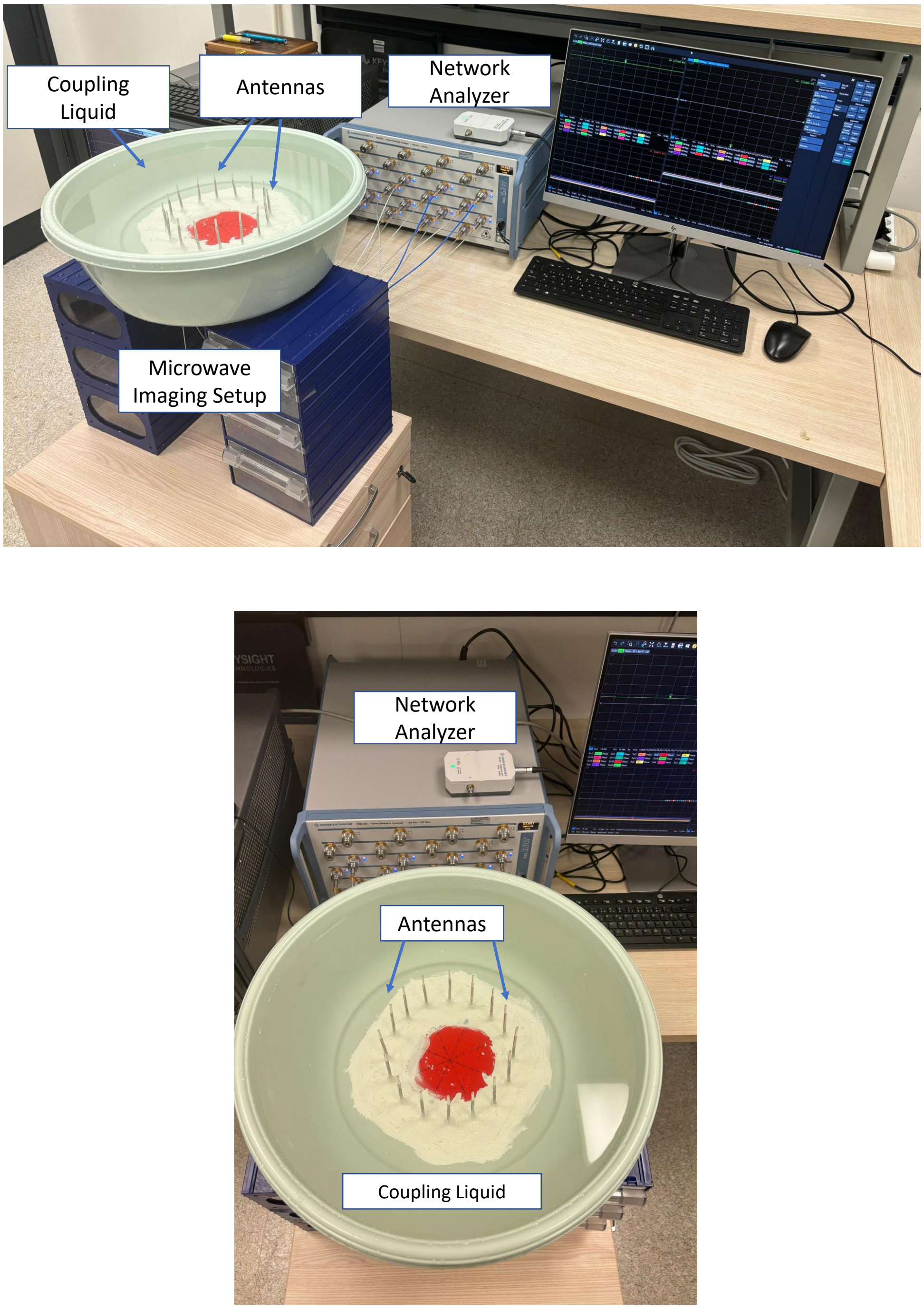

Figure 5.1: Measurement setup for microwave imaging with coupling liquid. N = 16 antennas were placed in a uniform circular arrangement in a radius of 160 mm. For measurements, the target is positioned inside the antennas.

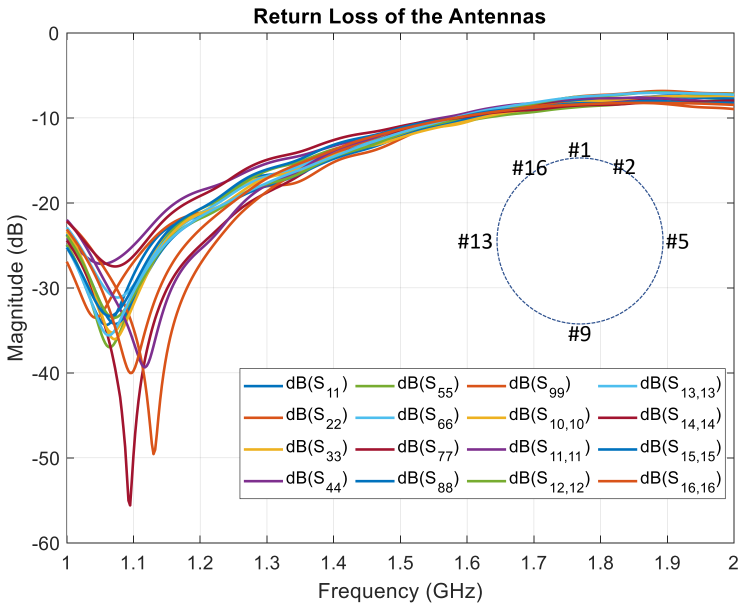

Figure 5.2: Return loss measurement of the antennas inside the coupling liquid. Inset figure shows the antenna positioning.

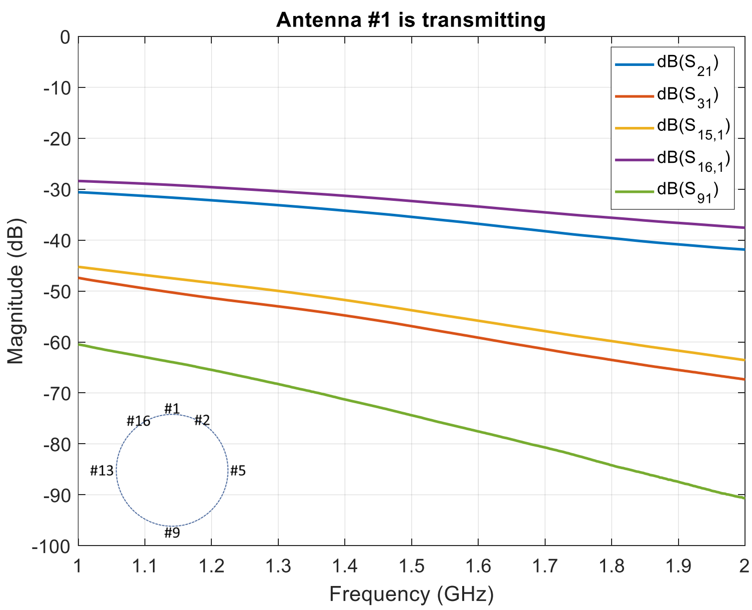

Figure 5.3: Coupling values between the antennas when antenna 1 is transmitting inside the coupling liquid. Inset figure shows the antenna positioning.

5.1.2 Measurements for Phantom – 1 : Microwave Imaging Phantom

Microwave imaging phantom (Phantom – 1) contains a breast phantom with 85 mm diameter, and fibroglandular and tumor inclusions with 20 mm diameter. The fibroglandular and tumor inclusions were positioned manually at $[x, y] = [-20, 0]$ mm and $[x, y] = [20, 0]$ mm, respectively. The permittivity and conductivity values of the phantom and the coupling liquid at 1.5 GHz are given in Table 5.1.

For the measurements, Phantom – 1 was inserted into the measurement setup as shown in Figure 5.4. A schematic, which shows the phantom, antenna, and coupling medium positions together with the dimensions and the electrical properties is given in Figure 5.5. Due to the high density of the coupling liquid, the phantom was tended to move upwards. To prevent this movement a cylinder made of delrin was inserted to the top of the phantom. In addition, the phantom was lifted up by inserting glass petri dishes underneath the phantom. The measurement setup was manually arranged to mimic 2D imaging scenario as close as possible. The simulation results for the imaging scenario where the phantom was inserted in the middle of the imaging area is presented in Figure 5.6 together with the actual permittivity and conductivity images. The permittivity and conductivity values along the $x = 0$ mm line is presented in Figure 5.6 together with the actual measurement data. The simulation results show that the permittivity and conductivity values have been reconstructed well at the target region.

For the experiments, the measurements were performed using network analyzer at 1.5 GHz, with an IF bandwidth of 10 Hz, and averaged over 20 measurements. The output power was 0 dBm.The operating frequency was selected where the return loss (S_{ii}) measurements were less than -10 dB and exhibited minimal differences. First, the phantom was not placed into the imaging setup, and an empty measurement was taken with the coupling liquid. Then, the phantom was inserted manually into the imaging setup. The empty measurement was used for the S-parameter to E-field conversion.

The image reconstructions were performed as explained in Section 2.2 - Inverse Problems. As the initial image, an empty model was given with electrical properties equal

Table 5.1: Permittivity and conductivity values of Phantom – 1 and the coupling liquid at 1.5 GHz

Frequency = 1.5 GHz	Permittivity	Conductivity (S/m)
Breast (Med3G9)	22.8	0.27
Fibroglandular (High2G9)	40.2	0.52
Tumor (Mali1G16)	47.2	0.70
Coupling Medium	21.7	1.43

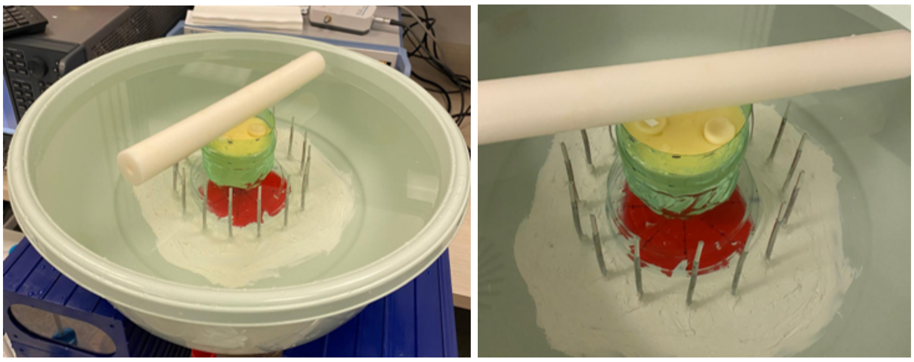

Figure 5.4: Measurement setup for the microwave imaging phantom (Phantom – 1). The phantom was positioned at the center of the imaging domain and fixed by placing a heavy delrin cylinder.

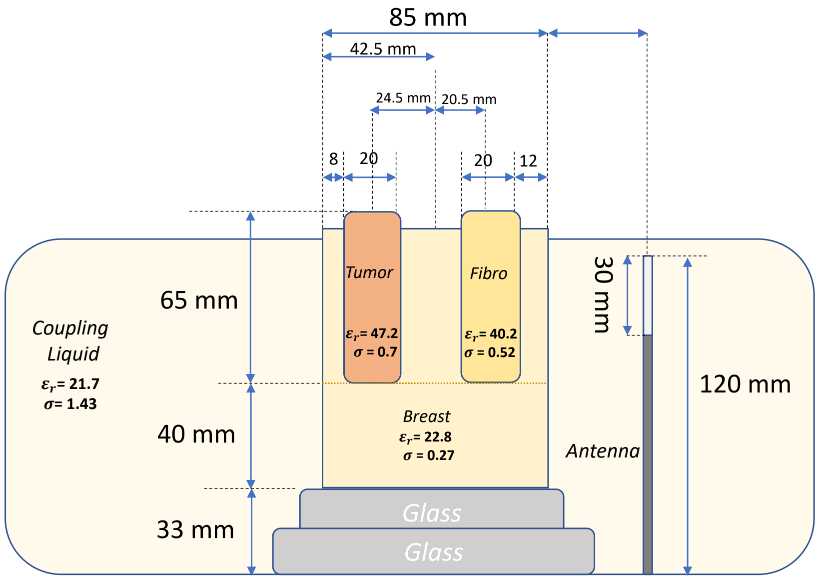

Figure 5.5: Schematic of the measurement setup for the microwave imaging phantom (Phantom – 1).

to the coupling liquid. The regularization parameter was set empirically, and decreased according to (2.100) as the iterations continue. The simulation was stopped when the error difference falls below 0.01. In general, the algorithm converged within 20 to 25 iterations. The image reconstruction results for the Phantom – 1 measurement is presented in Figure 5.7. The positions of the surrounding breast phantom, and tumor and fibroglandular inclusions are represented with a dashed circle. In addition, the permittivity and conductivity values along the x = 0 mm line was presented in Figure 5.7 together with the actual measurement data.

The measurement results show that tumor and fibroglandular inclusions can be identified successfully. For the permittivity images, the actual data and the reconstructed image are in good agreement in terms of both shape and the permittivity values. The tumor inclusion has slightly higher permittivity value than the fibroglandular inclusion, as expected. For the conductivity images, the surrounding coupling liquid and the object locations are partly visible. However, there are more artefacts surrounding the tumor and fibroglandular inclusions compared to the permittivity images.

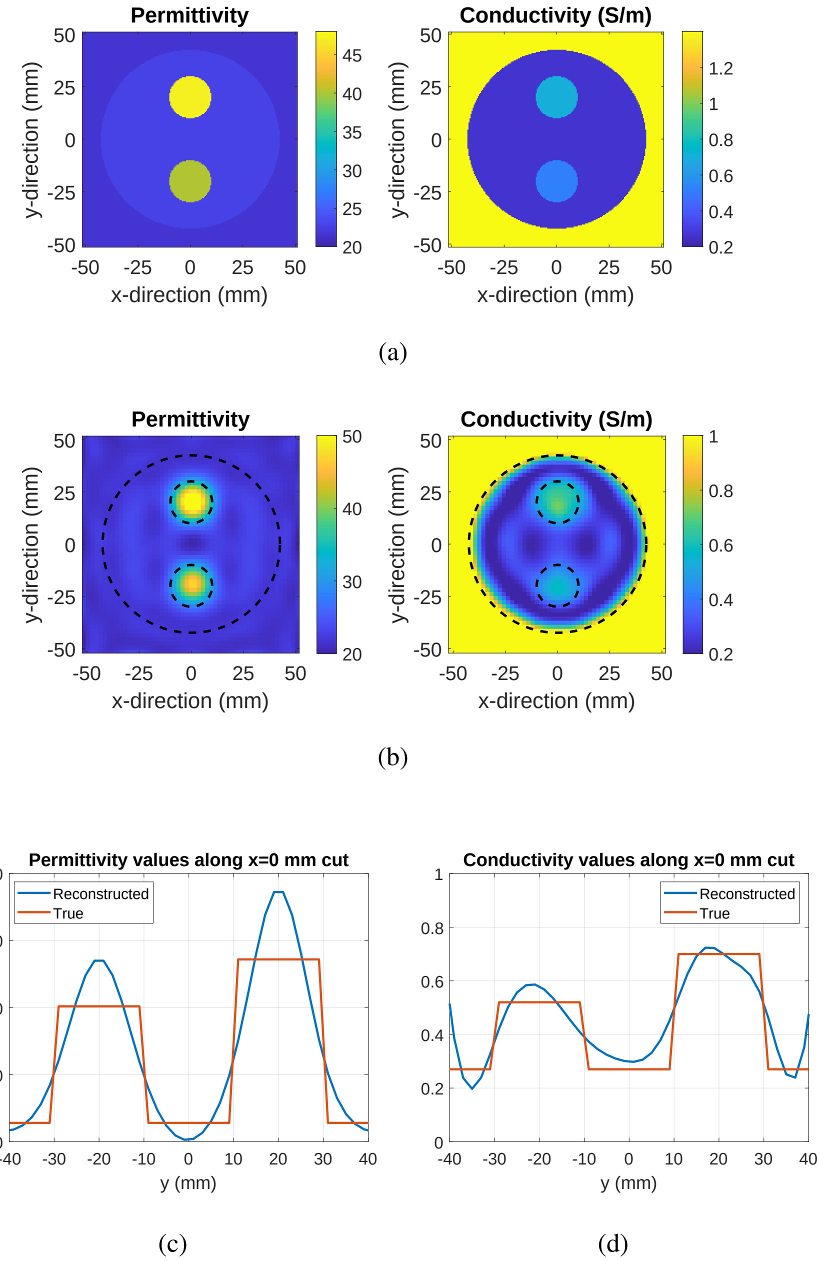

Figure 5.6: (a) The actual imaging scenario for microwave imaging phantom (Phantom – 1). (b) The simulation results for the actual imaging scenario. The reconstructed (c) permittivity and (d) conductivity (S/m) values along $y = 0\ mm$ cut.

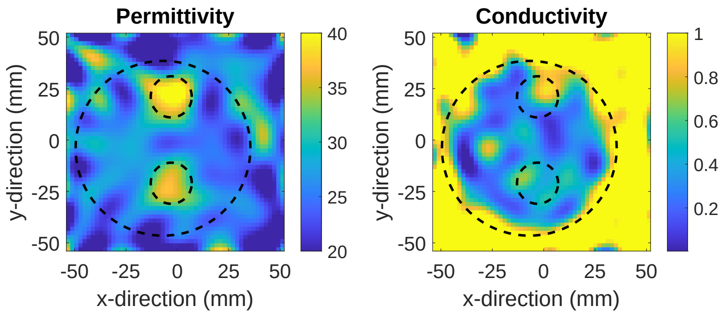

(a)

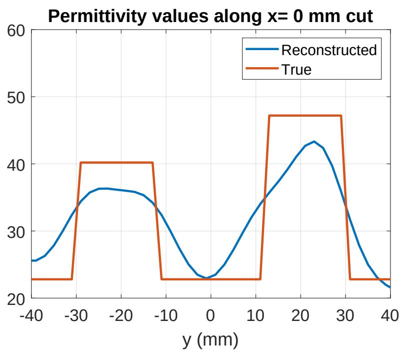

(b)

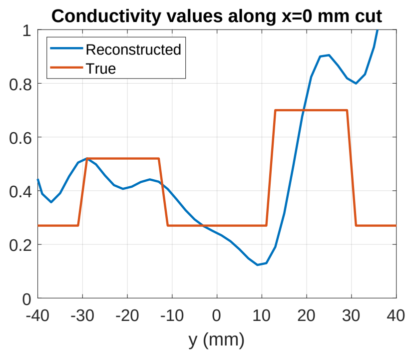

(c)

Figure 5.7: (a) The reconstruction results for microwave imaging phantom (Phantom – 1) measurements. (a) Reconstructed permittivity and conductivity (S/m) images. (c) Permittivity and (d) conductivity values along $y = 0\ mm$ cut.

5.1.3 Measurements for Phantom – 2 : Multi-Modal Imaging Phantom

Multi-modal imaging phantom (Phantom – 2) contains a breast phantom with 92 mm diameter, and fibroglandular and tumor inclusions with 20 mm diameter. The fibroglandular and tumor inclusions were inserted at $[x, y] = [-20, 0]$ mm and $[x, y] = [20, 0]$ mm, respectively. The permittivity and conductivity values of the Phantom – 2 and the coupling liquid at 1.3 GHz are given in Table 5.2. The 1.3 GHz is selected since the loss due to the coupling liquid decreases as the frequency decreases [146].

For the measurements, Phantom – 2 was inserted into the measurement setup as shown in Figure 5.8. The schematic which shows the phantom, antenna, and coupling medium positions together with the dimensions and the electrical properties is given in Figure 5.9.

Unlike the previous measurement, the phantom was fixed to the laboratory stand and positioned from above within the imaging area. Due to the high density of the coupling liquid, the phantom tended to move in different directions during the placement. The measurement setup was manually arranged to mimic 2D imaging scenario as close as possible.

The simulation results for the imaging scenario are presented in Figure 5.10 together with the actual permittivity and conductivity images. In addition, the permittivity and conductivity values along the $y = 0\ mm$ line were presented together with the actual measurement data.

The simulation results show that the permittivity and conductivity values have been reconstructed well at the target region. Note that, the permittivity values overshoot the true values as a result of the regularization algorithm. Since the sharp change of the electrical parameters between the target and the background medium is smoothed in the reconstructed image, the algorithm tries to compensate this change with an overshoot at the center region. Similar results can also be observed in [95, 147].

For the experiments, the measurements were performed at 1.3 GHz, with an IF bandwidth of 10 Hz, and averaged over 20 measurements. The output power was 0 dBm. First, the phantom was not placed into the imaging setup, and an empty measure-

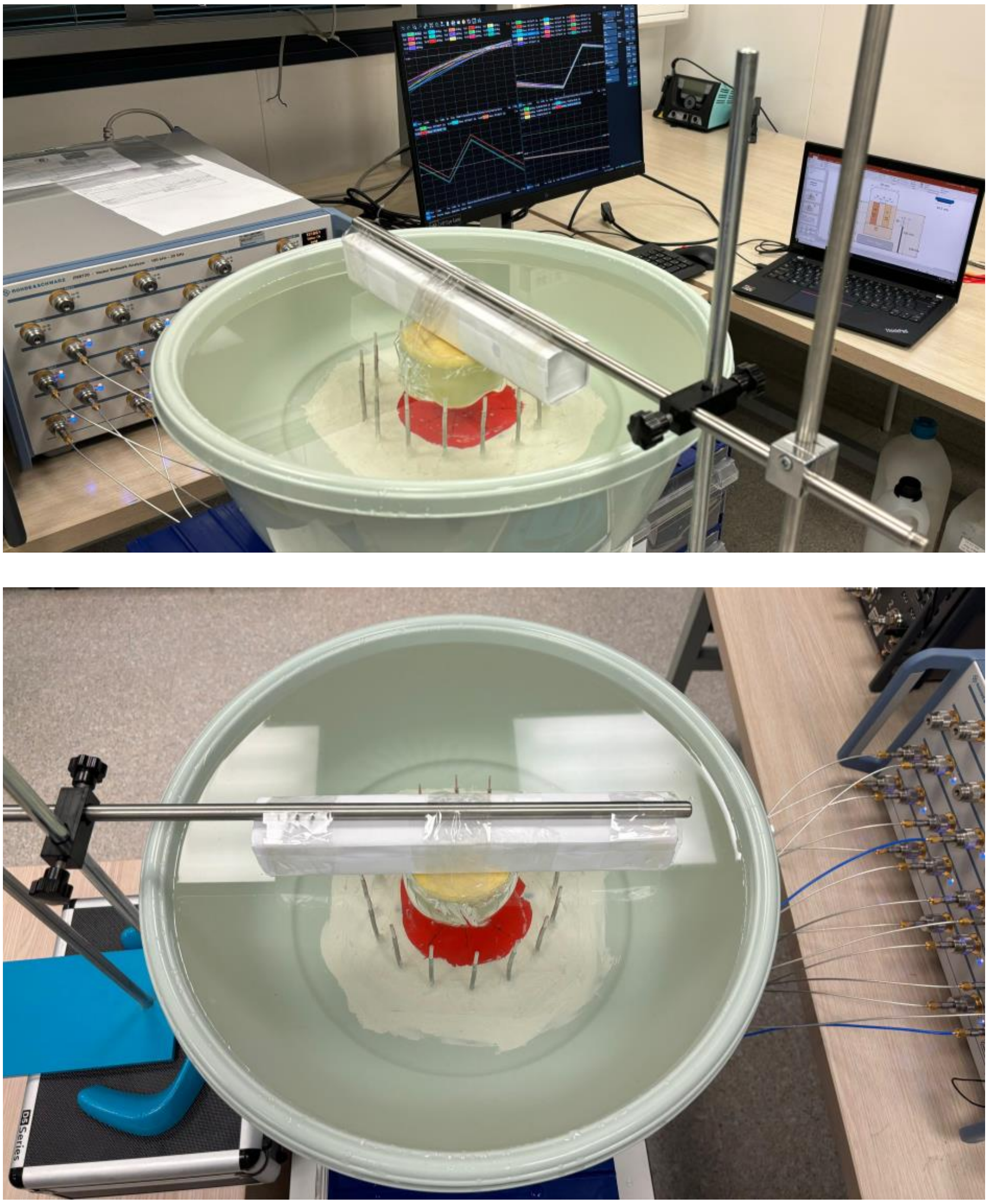

Figure 5.8: Measurement setup for the multi-modal imaging phantom (Phantom – 2). The phantom was positioned at the center of the imaging domain from above.

Table 5.2: Permittivity and conductivity values of multi-modal imaging phantom (Phantom – 2) and the coupling liquid at 1.3 GHz

Frequency = 1.3 GHz	Permittivity	Conductivity (S/m)
Breast (Med2G7)	24.6	0.21
Fibroglandular (High1G6)	41.5	0.34
Tumor (Mali3G21)	44.8	0.60
Coupling Medium	20.9	1.15

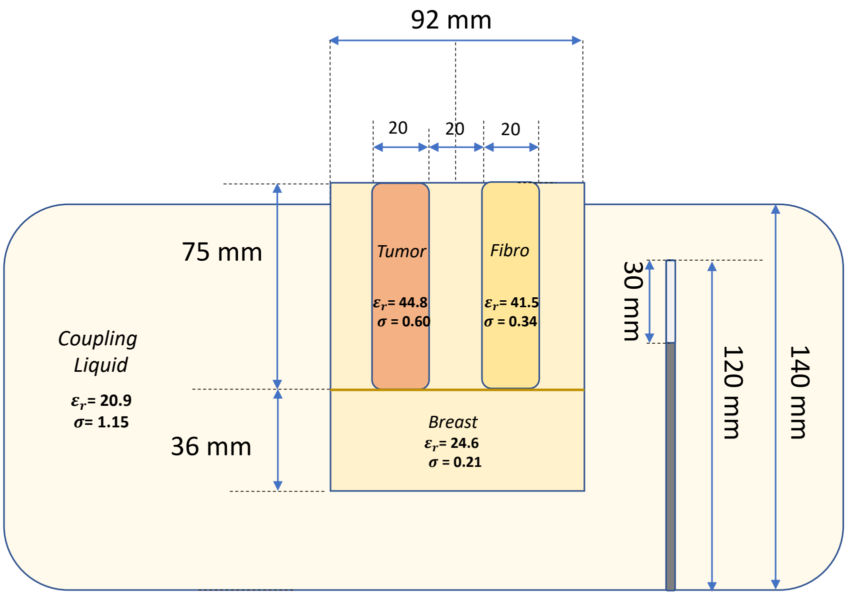

Figure 5.9: Schematic of the measurement setup for the multi-modal imaging phantom (Phantom – 2).

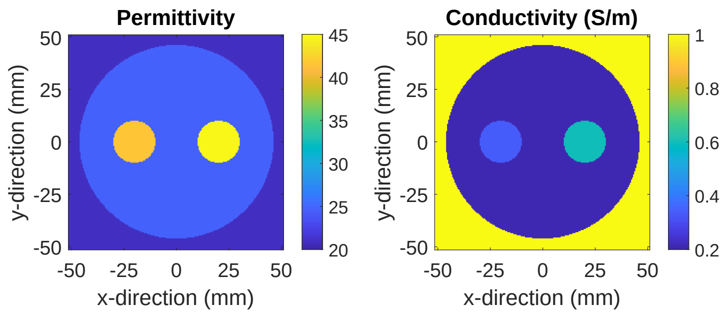

(a)

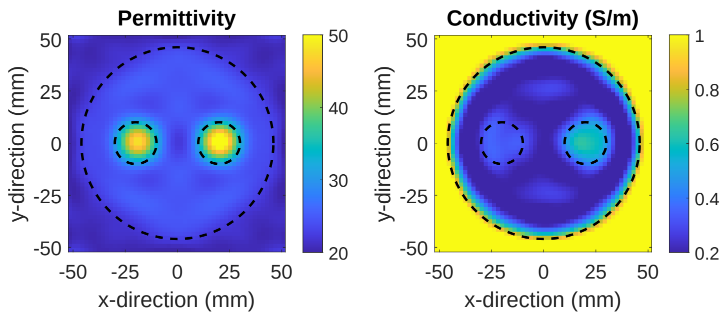

(b)

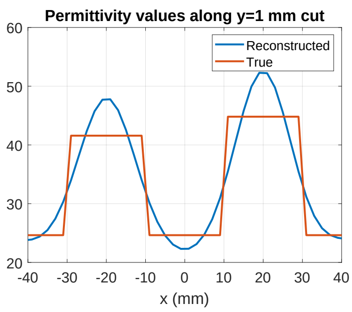

(c)

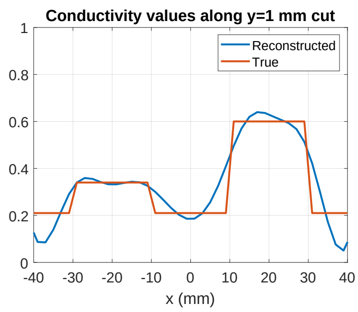

(d)

Figure 5.10: (a) The actual imaging scenario for multi-modal imaging phantom (Phantom – 2). (b) The simulation results for the actual imaging scenario. The reconstructed (c) permittivity and (d) conductivity (S/m) values along $y = 0$ mm cut.

ment was taken for coupling liquid. Then, the phantom was inserted manually into the imaging setup. The empty measurement was used for the S-parameter to E-field conversion.

Two sets of measurements were taken. In the first set, the phantom was kept in the middle of the imaging area and manually rotated around its axis for nearly 45, 90 and 180 degrees in the clock-wise direction. Therefore, the positioning of the tumor and fibroglandular inclusions was changed around the imaging axis. In the second set of measurements, the phantom was translated in the x and y directions. The translation was nearly $\pm$ 1.5 cm in the x direction. For the y direction, the translation was nearly -1.5 cm. Note that, since the positioning was done manually, both the rotation and translation values are approximate values.

The image reconstructions were performed as explained in Section 2.2 - Inverse Problems. As an inital image, an empty model was given with electrical properties equal to the coupling medium. The regularization parameter was set empirically, and decreased according to Equation 2.100 as the iterations continue. The simulation was stopped when the error difference falls below 0.001.

The reconstruction results for the first and second set of measurements are presented in Figure 5.11 and Figure 5.12, respectively. The positions of the surrounding breast phantom, and tumor and fibroglandular inclusions are represented with a dashed circle in the figures.

In addition, the permittivity and conductivity values for the 0 degree rotation case (See Figure-5.11) along the $y = 1$ mm line is presented in Figure 5.13 together with the actual measurement data. The maximum values of the permittivity and conductivity images of the 0 degree rotation case, and the actual values are given Table 5.3.

When the reconstruction results were examined, it was observed that the permittivity of the tumor and fibroglandular inclusions could be estimated close to the actual values and were similar to the ground truth image in terms of both location and shape.

However, when the conductivity images were examined, it was observed that the surrounding medium could be seen, but the tumor and fibroglandular inclusions were not very clearly visible. This finding is also compatible with the simulation results

Table 5.3: The maximum values of the reconstructed permittivity and conductivity images for 0 degree rotation case of multi-modal imaging phantom (Phantom – 2) (see Figure 5.11 - (a)). Actual values are obtained from phantom measurements.

	Permittivity		Conductivity (S/m)	
	Actual	Measurement	Actual	Measurement
Fibroglandular Tissue	41.58	36.04	0.34	0.43
Tumor Tissue	44.80	41.30	0.60	0.59

shown in Figure 5.10 and the previous studies that evaluate conductivity images [94, 147, 179]. In addition, the conductivity images exhibit lower values at the center of the imaging area than expected. This may be caused by the high contrast between the coupling liquid (σ = 1.15 S/m) and the breast phantom (σ = 0.21 S/m). Since the conductivity of the surrounding coupling liquid was reconstructed with a higher value (approximately σ = 1.5 S/m), the imaging algorithm might have tried to recover the contrast by decreasing the conductivity inside the imaging area.

5.2 Shear Wave Elasticity Imaging using Microwave Imaging as Prior Information

In this section, shear wave imaging measurements are performed on the multi-modal imaging phantom (Phantom – 2) using the prior information from microwave imaging. This prior information is used to position the ultrasound probe on the desired regions. Since microwave imaging provides a dielectric map of the imaged area, shear wave elasticity imaging can be conducted only in regions with potential tumors for better identification.

This section explains the experimental setup for shear wave elasticity imaging and the data processing for the estimation of Young's modulus. It then presents the conducted measurements and obtained results using the multi-modal imaging phantom (Phantom – 2).

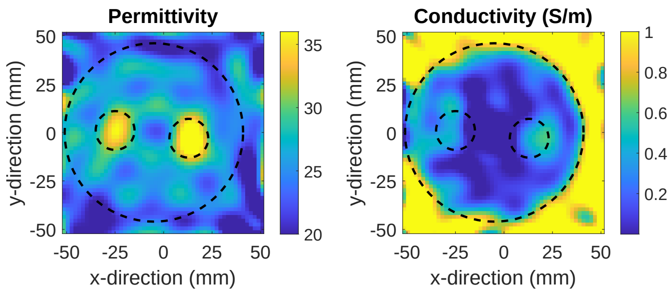

(a)

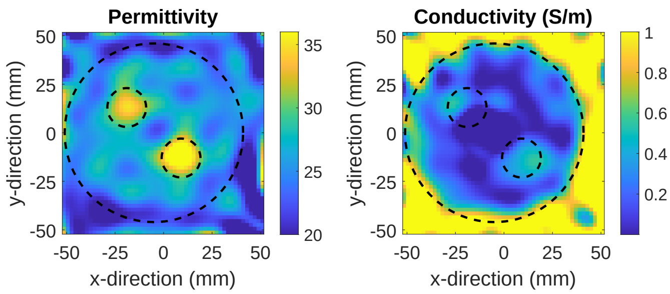

(b)

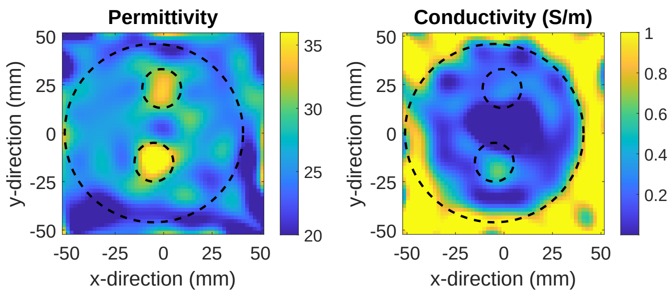

(c)

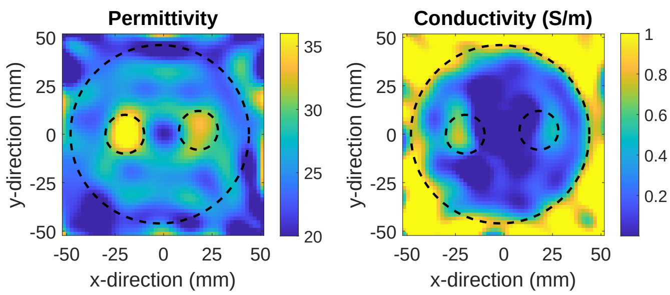

(d)

Figure 5.11: The reconstructed permittivity and conductivity values inside imaging area for multi-modal imaging phantom (Phantom – 2) measurements. (a) 0 degrees case. The tumor was centered at $[x, y] = [13, -3]\ mm$. Reconstructed images of the phantom for (b) 45, (c) 90, and (d) 180 degrees clock-wise rotation.

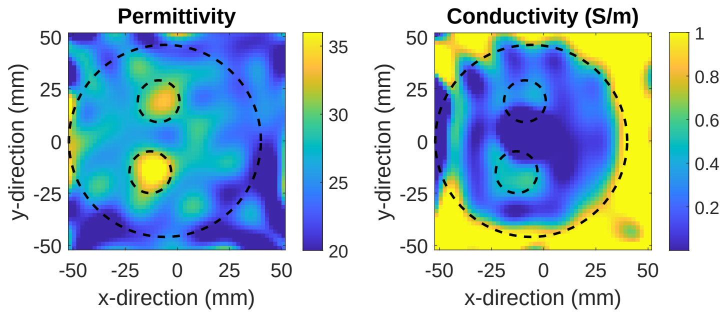

(a)

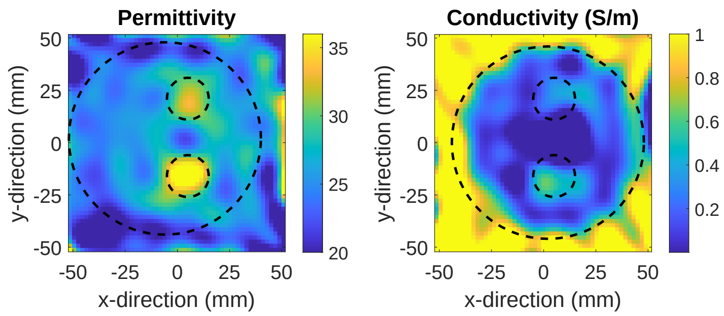

(b)

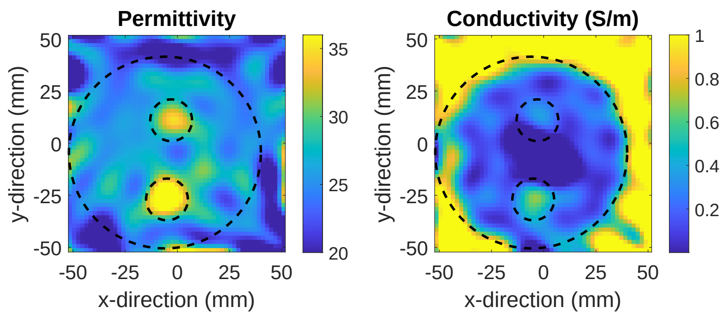

(c)

Figure 5.12: The reconstructed permittivity and conductivity values inside imaging area. The multi-modal imaging phantom (Phantom – 2) was manually translated to (a) -1.5 cm on the x-axis, (b) +1.5 cm on the x-axis, (c) -1.5 cm on the y-axis.

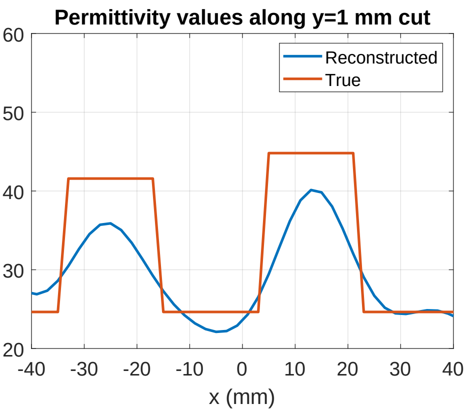

(a)

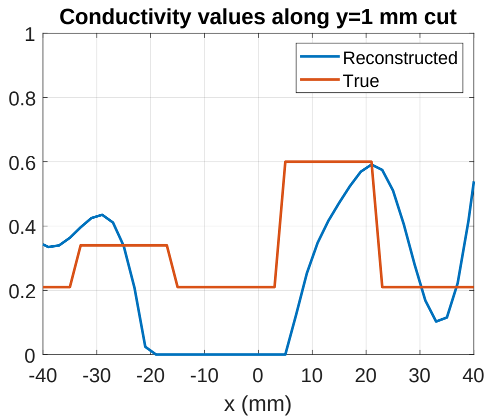

(b)

Figure 5.13: The reconstructed (a) permittivity and (b) conductivity (S/m) values along $y = 1\ mm$ cut for the multi-modal imaging phantom (Phantom – 2) given in Figure 5.11 (a) - 0 degrees rotation case.

5.2.1 Experimental Setup for Shear Wave Elasticity Imaging

Shear wave elasticity imaging experiments were conducted using the Verasonics Vantage ultrasound research system (Verasonics, Inc., Kirkland,WA, USA) [180]. This system comprises of a data acquisition system, a workstation, a data acquisition software, and variety of ultrasound transducers. Verasonics system provides a highly flexible platform for ultrasound research [180]. It allows the users to design transmit/receive sequences, and enables to acquire, store, display, and analyze the raw ultrasound data.

In this thesis study, Verasonics Vantage 256 system at ASELSAN Acoustic Research Laboratory has been utilized (see Figure 5.14). The system is operated using the settings given in Table 5.4 and L11-5V linear ultrasound probe is used for the measurements [180].

In Verasonics systems, a programming script which specifies the imaging parameters is written in MATLAB and loaded into system to generate an imaging sequence. After the completion of the sequence, the ultrasound data can be obtained as raw RF

Table 5.4: Imaging Parameters for shear wave elasticity imaging

Parameter	Value
L11-5V Bandwidth	[4.68 - 10.52] MHz
L11-5V Elevational Focus	18 mm
L11-5V Number of elements	128
L11-5V Pitch	0.3 mm
Push Frequency	7.6 MHz
Track Frequency	7.6 MHz
Speed of Sound	1540 m/s
Wavelength	0.202 mm
Number of push cycles	1000 cycles
Pulse Repetition Interval	100 us
Number of Push Pulse	4
Number of Tracking Frames	50

data, beamformed in-phase and quadrature (IQ) data, and envelope detected image data. In this thesis study, the programming script for the Verasonics system was written following the guidelines given in [181] and Vantage programming sequence manual [180].

The sequence for the shear wave elasticity imaging can be summarized as follows. First, an acoustic radiation force is created using a focused push pulse. Then, the induced shear waves are tracked very rapidly with a pulse repetition interval of 100 μs using plane waves. In our measurements, 4 push pulses were applied and the resulting shear waves were tracked using 50 frames after each push pulse. For the generation of the push beam, 32 elements located at the center of the transducer were used.

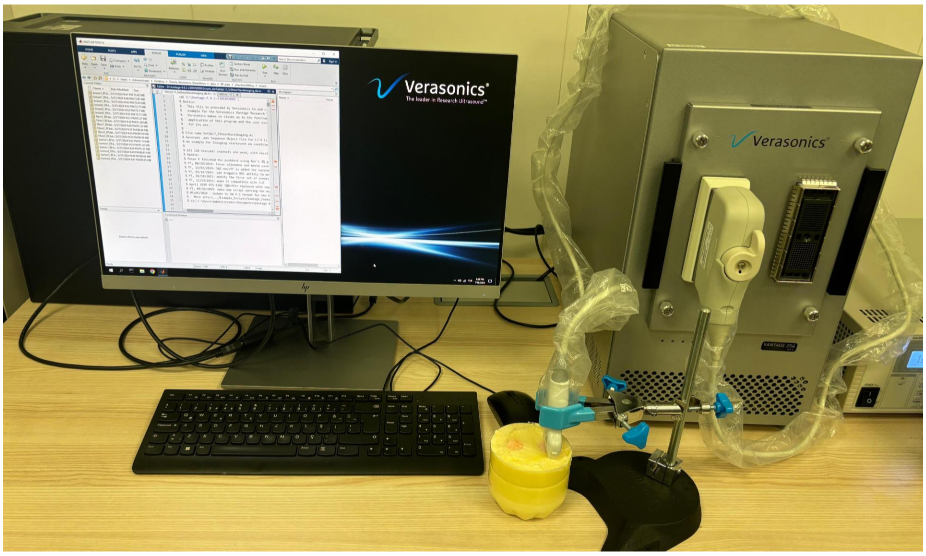

Figure 5.14: The Verasonics Vantage Ultrasound Research System at ASELSAN A.S.

5.2.2 Young's Modulus Estimation

After obtaining the received signal data using Verasonics system, mainly three steps need to be followed for the Young's modulus estimation [181]: 1) displacement estimation, 2) displacement data filtering, and 3) estimation of the shear wave speed. The flow chart for the estimation of the Young's modulus is given in Figure 5.15.

For the displacement estimation, generally phase shift algorithms are used [182]. Two of the commonly used phase shift algorithms are Kasai [183] and Loupas [184] algorithms. Kasai algorithm determines the displacement between a reference and displaced signal by measuring the average phase shift with respect to the constant center frequency (transducer operation frequency) and it is readily available in the Verasonics system. On the other hand, Loupas algorithm, accounts for the change in the center frequencies of the RF echoes at each axial position and leads to more accurate results. In this thesis study, the displacement estimation is obtained using the USTB ultrasound toolbox [185] which uses Loupas algorithm. The detailed explanations of the Kasai and Loupas algorithms are presented in Appendix A. As an example, the displacement data obtained using Phantom – 2 from the breast region at different time instances are shown in Figure 5.16. Note that, the displacement data is 3-D, which can be expressed as [axial $\times$ lateral $\times$ time]. The displacement data is calculated for each of the 4 push pulses and averaged to reduce the noise on the displacements.

For the second step, the displacement data was filtered using a directional filter. In shear wave elasticity imaging, the reflections occurring from the boundaries, which have different stiffness values can result in artifacts in the reconstructions. To eliminate this reflections, the 2D displacement data $d(x, t)$ which is a function of lateral position and time [lateral $\times$ time], is transformed to the frequency domain data (k_x, ω) and only the shear waves propagating through the desired direction (rightward or leftward) is selected [163]. For a propagating wave, the k-space domain is divided into four quadrants and the forward propagating waves corresponding to the first and third quadrants of the spectrum are selected. Using these quadrants and multiplying the frequency domain displacement data, the reverse propagating waves are eliminated. Then, using inverse Fourier transform, the displacement data in space-time domain is obtained. The process for the directional filtering is summarized in Figure 3.5. In addition, the displacement data obtained using multi-modal imaging phantom (Phantom – 2) from the breast-tumor interface before and after the directional filtering is shown in Figure 5.17.

For the third step, the shear wave speed was estimated using the displacement data. Before, using the estimation algorithms, the displacement data was transformed into 2D-data (lateral $\times$ time) by taking the average of the displacement data in the axial directions. The averaging was performed only in a region around the focal depth of the push beam which is called as depth of field (DOF). The DOF can be calculated as $8F^2\lambda$ where F is the F-number of the ultrasound transducer (ratio of focal depth to aperture size [181]) and λ is the wavelength of the transmitted ultrasound wave.

Another important point in shear wave estimation is choosing lateral positions away from the push beam. Since diffraction occurs in regions close to the push beam [186], lateral positions should be chosen away from the excitation beamwidth, which can approximately calculated as $F\lambda$. Especially in stiff regions, it is important to choose lateral positions away from the excitation due to the rapid shear wave progress.

After obtaining the 2D-displacement map, where the displacement is represented as a 2D data in position and time, generally time-of-flight methods, which are linear re-

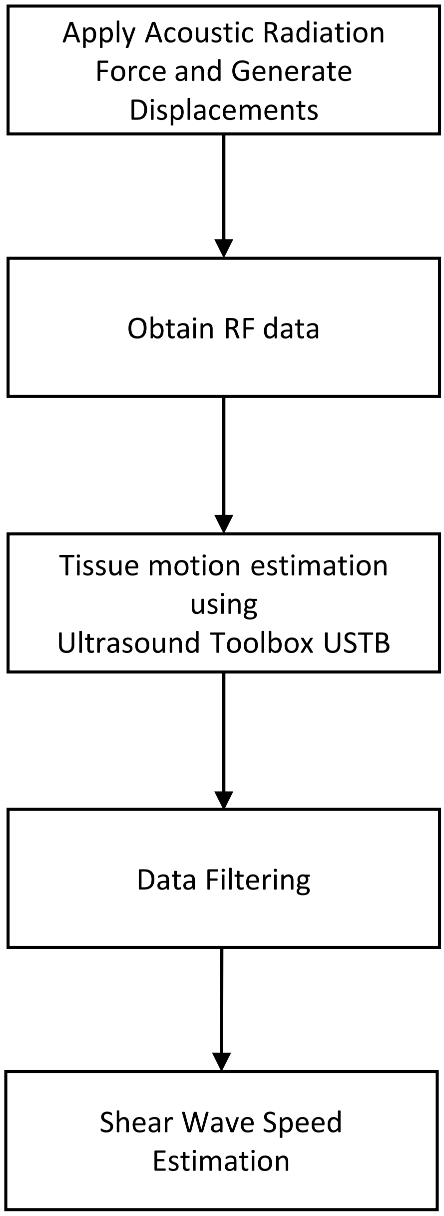

Figure 5.15: The flow chart for the data processing of shear wave elasticity imaging.

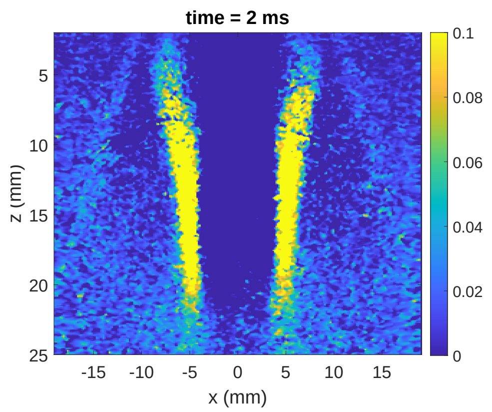

(a)

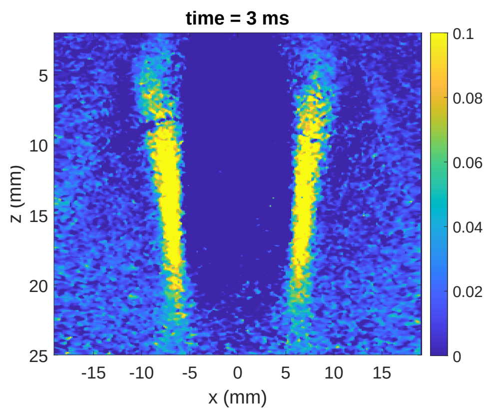

(b)

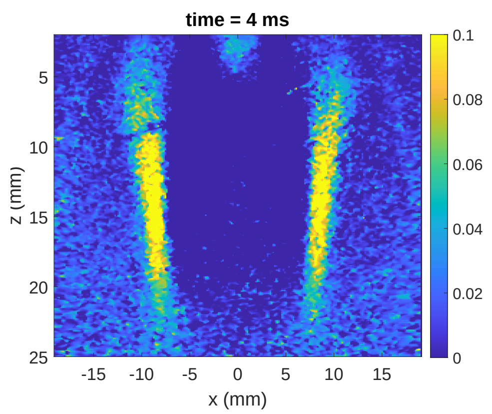

(c)

Figure 5.16: Displacement of the tissue at time instances t = 2, 3, 4 ms for the homogeneous breast region of the Phantom – 2. The colorbar shows the displacement in terms of μm.

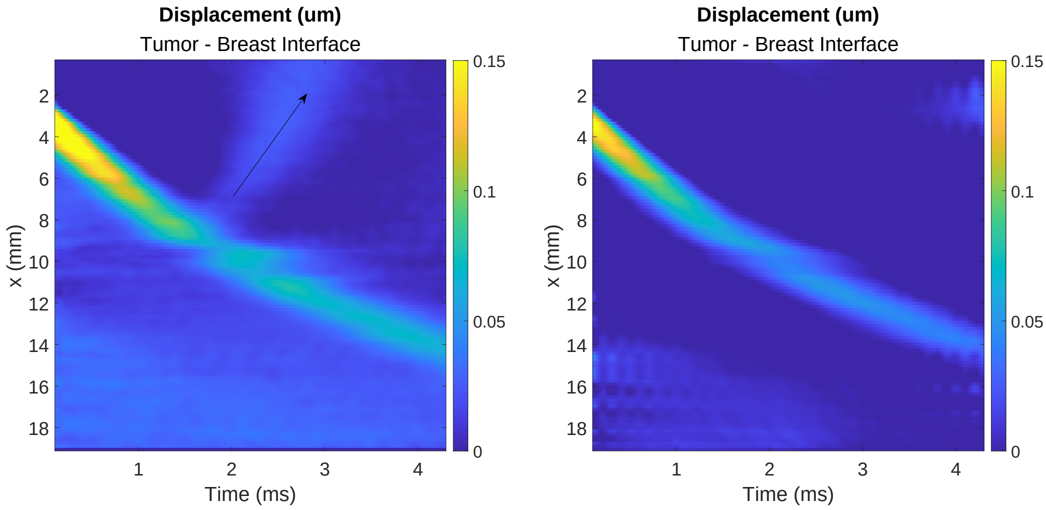

(a)

(b)

Figure 5.17: 2D displacement maps for the tumor-breast interface of the multi-modal imaging phantom (Phantom – 2) (a) before the directional filter and (b) after directional filter. The reflection at the tumor breast interface is represented with an arrow. The colorbar shows the displacement in terms of μm.

gression and shear wave trajectory detection, are used. In linear regression methods, such as time-to-peak displacement, the arrival time of the shear wave peaks at each lateral position is determined and linear regression is performed. Then, shear wave speed is calculated from the slope of the linear regression. This method has been applied successfully for shear wave elasticity imaging applications [33, 187]. However, this method may create an outlier data due to low SNR and/or inhomogeneities in the tissue, which results in error in the shear wave speed estimation. To eliminate the outlier data and to enable a better estimation of the shear wave speed, trajectory based shear wave speed estimation methods, e.g., Radon sum transformation can be used. In this method, the optimal trajectory is determined as follows:

- The lateral range is fixed as $[x_{start}, x_{end}]$.
- Linear trajectories are formed using the line equation

$$x = (t - t_{start})c + x_{start}, \tag{5.2}$$

from starting position (x_{start}, t_{start}) to an ending position (x_{end}, t_{end}), where c_s

corresponds to slope of the trajectory, i.e., the shear wave speed.

- While forming the linear trajectories, multiple starting times and multiple ending times are used which satisfies shear wave propagation away from the push pulse ($x_{end} > x_{start}$ and $t_{end} > t_{start}$).

- The displacement data is summed along in each trajectory, similar to the Radon transform. The Radon sums can be expressed as

$$S(t_{start}, t_{end}) = \sum_{x_{start}}^{x_{end}} d(x, t) \tag{5.3}$$

where $d(x, t)$ is the displacement data.

- The maximum value of the Radon sum corresponds to optimal trajectory which gives t_{start}^{opt} and t_{end}^{opt} values.

Using the t_{start}^{opt} and t_{end}^{opt} values in (5.2), the shear wave speed is found. While applying the algorithm, the time data is up-sampled to increase the time resolution.

In Radon sum implementation, generally, the entire region of interest is assumed to be a homogeneous medium. To determine the shear wave speed in heterogeneous medium, sub-regions can be selected and the Radon sum can be performed over these regions [188]. Depending on the size of the sub-regions, the accuracy of the shear wave speed estimations may change.

In the measurements conducted for this thesis, shear wave speed values are determined using Radon sum algorithm. Thanks to the additional information coming from microwave tomography, the region in which the Radon sum algorithm to be applied is known in advance.

After obtaining the shear wave speed, assuming a linear and elastic medium for the soft tissues, the Young's modulus is calculated as

$$YM = 3\,\rho\,c_s^2 \tag{5.4}$$

where ρ is the density of the tissue and c_s is the shear wave speed.

5.2.3 Measurements of Multi-Modal Imaging Phantom (Phantom – 2)

For the shear wave elasticity imaging, multi-modal imaging phantom (Phantom – 2), which was used in microwave imaging, was measured using the Verasonics Research System.

Initially, Young's modulus values were estimated by scanning the entire phantom. After that, measurements were conducted without scanning the phantom and the prior information obtained from microwave imaging was used to position the ultrasound probe at possible tumor regions. In the first measurement, the ultrasound probe was placed directly on top of the tumor, breast, and fibroglandular tissues, and the Young's modulus values were estimated. In the second measurement, the ultrasound probe was placed on two sides of the phantom, resembling the practical application of the proposed multi-modal imaging. The probe was aligned with the tumor and fibroglandular inclusions and Young's modulus values were estimated.

5.2.3.1 Scanning the Entire Phantom

Although the aim is to find Young's modulus values without performing a phantom scan, whole breast phantom was also scanned with a focus depth of 16 mm at 15 positions as shown in Figure 5.18- (a). The displacement maps are obtained and the Radon sum is applied for the shear wave detection using the prior information from microwave imaging. Since the push beam is applied directly at the center of the lateral axis, both rightward and leftward travelling waves are tracked. Considering the excitation beamwidth of the push beam, the displacement values close to the focused region are omitted. This region is then interpolated using the Young's modulus values estimated from the shear wave speeds of the rightward and the leftward tracking waves. The obtained shear wave image is shown in Figure 5.18-(b) with dashed lines representing the position of the fibroglandular and tumor tissues. As can be seen in Figure, the Young's modulus values of the phantom has been obtained quantitatively, and the tumor is distinguishable.

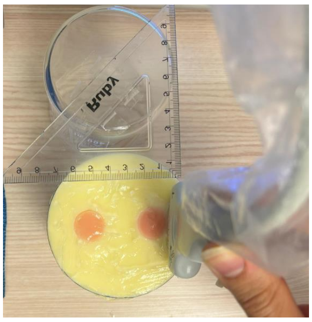

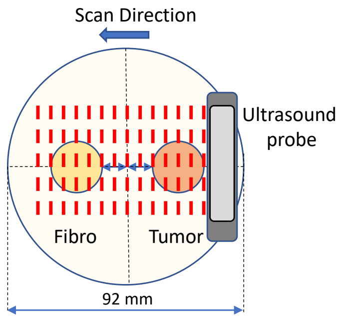

(a)

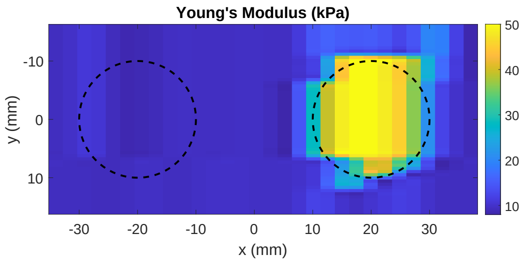

(b)

Figure 5.18: (a) The scan trajectory. (b) Reconstructed shear wave image of Phantom – 2 for the given scan trajectory. Dashed lines show the position of the fibroglandular and tumor tissues.

5.2.3.2 Positioning the Ultrasound Probe on Possible Tumor Regions

This section presents the results obtained using prior information from microwave imaging to position the ultrasound probe in two different cases. In the first case, the ultrasound probe was placed directly on top of the tumor, breast, and fibroglandular tissues. In the second case, practical application of multi-modal imaging was considered and the ultrasound probe was placed at two sides of the phantom, aligning with the tumor and fibroglandular tissues. The imaging setup that is intended for the practical use of the proposed method is depicted in Figure 5.19 and the schematic representation of the two imaging scenarios is shown in Figure 5.20.

The imaging setup intended for the practical use includes a shear wave imaging ultrasound system with a linear ultrasound probe and a microwave imaging system. The ultrasound probe can move automatically with a mechanical actuator, without depending on the operator. The linear ultrasound probe is located outside of the imaging area to avoid interfering with the microwave imaging. First, microwave imaging is performed. The quantitative permittivity map obtained from microwave imaging serves as prior information, guiding the ultrasound probe to the the suspicious tissues. Then, the ultrasound probe, controlled by the mechanical actuator, is positioned on the suspicious regions, without applying pressure to the tissues. Shear wave imaging is performed and quantitative Young's modulus values are obtained for the suspicious regions. Using these quantitative Young's modulus and dielectric parameters, tumor identification may be achieved through the proposed multi-modal imaging.

For the first scenario, shear wave measurements were performed at three locations: on top of the tumor inclusion, fibroglandular inclusion, and breast. The focus depth was 16 mm. The shear wave measurement setup in which the ultrasound probe is located on top of the tumor inclusion is shown in Figure 5.21. The obtained 2D displacement maps were presented along with the B-mode images for tumor in Figure 5.22. Similarly, obtained B-mode images and displacement maps are presented for breast and fibroglandular region in Figure 5.23, and Figure 5.24, respectively.

For the measurements taken on the tumor inclusion, the slope changed at the interface between the tumor and breast tissue (see Figure 5.22). The shear wave speed

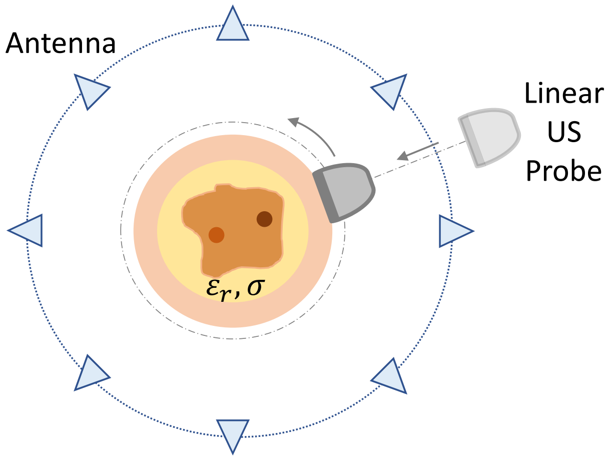

Figure 5.19: The imaging setup that is intended for the practical use of the proposed method. The imaging setup includes a linear ultrasound probe for shear wave imaging and a microwave imaging system. The ultrasound probe can move automatically with a mechanical actuator, without operator dependence. First, the probe is positioned outside the imaging area to avoid interference with microwave imaging, which is performed to obtain a quantitative permittivity map. This map guides the probe to the suspicious tissues. The probe is then moved to these regions without applying pressure, and shear wave imaging is performed to obtain quantitative Young's modulus values. Using these values and dielectric parameters, tumors may be identified through the proposed multi-modal imaging.

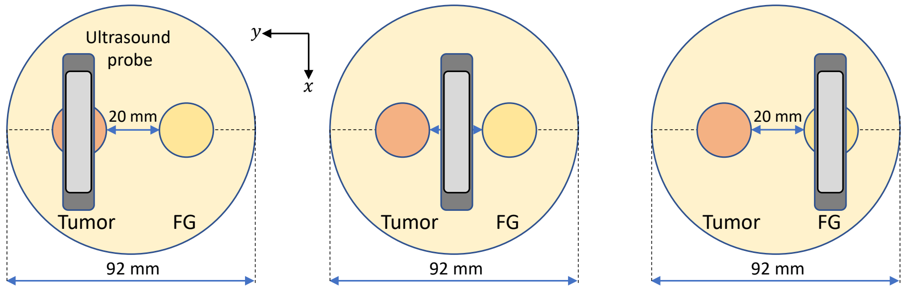

(a)

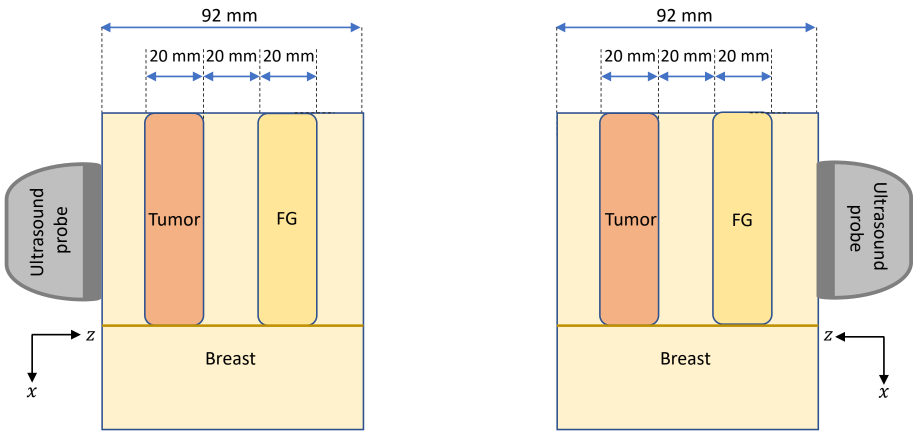

(b)

Figure 5.20: (a) The first imaging scenario. The ultrasound probe was positioned at three locations: on top of the tumor inclusion, breast, and fibroglandular (FG) inclusion. (b) The second imaging scenario. The ultrasound probe was positioned at the sides of the phantom, aligning with the tumor and fibroglandular tissues. The ultrasound beam was focused on the tumor and fibroglandular tissues.

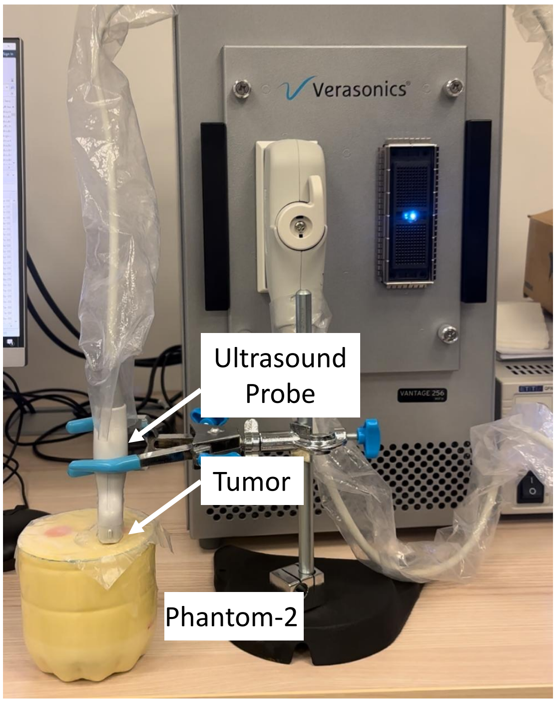

Figure 5.21: The measurement setup for the shear wave elasticity imaging. The ultrasound probe is positioned on top of the tumor inclusion.

was calculated using Radon sum algorithm. Only the shear waves propagating inside the tumor inclusion were used for the calculation. As previously stated, the borders for the shear wave elasticity imaging region was determined according to microwave imaging results. Similarly, the shear wave speeds were measured for the fibroglandular and breast tissues. The shear wave speeds (c_s) and Young's modulus (YM) values for the tumor, breast, and fibroglandular tissues were found as c_s = [4.02 - 1.80 - 1.68] m/s, YM = [48.5 - 9.8 - 8.52] kPa, respectively. The obtained results were tabulated in Table 5.5 together with the reference values. The measured and reference values are consistent with each other.

In the second scenario, which is similar to the practical application of the proposed method, shear wave measurements were performed on both sides of the phantom. For both the tumor and fibroglandular tissue, measurements were taken by focusing the ultrasound beam on two different depths: 22 mm and 24 mm. For the measurements taken on the tumor, the B-mode image with focus points and the obtained 2D displacement maps are shown in Figure 5.25. The shear wave speed was calculated using Radon sum algorithm. The shear wave speed and Young's modulus (YM) val-

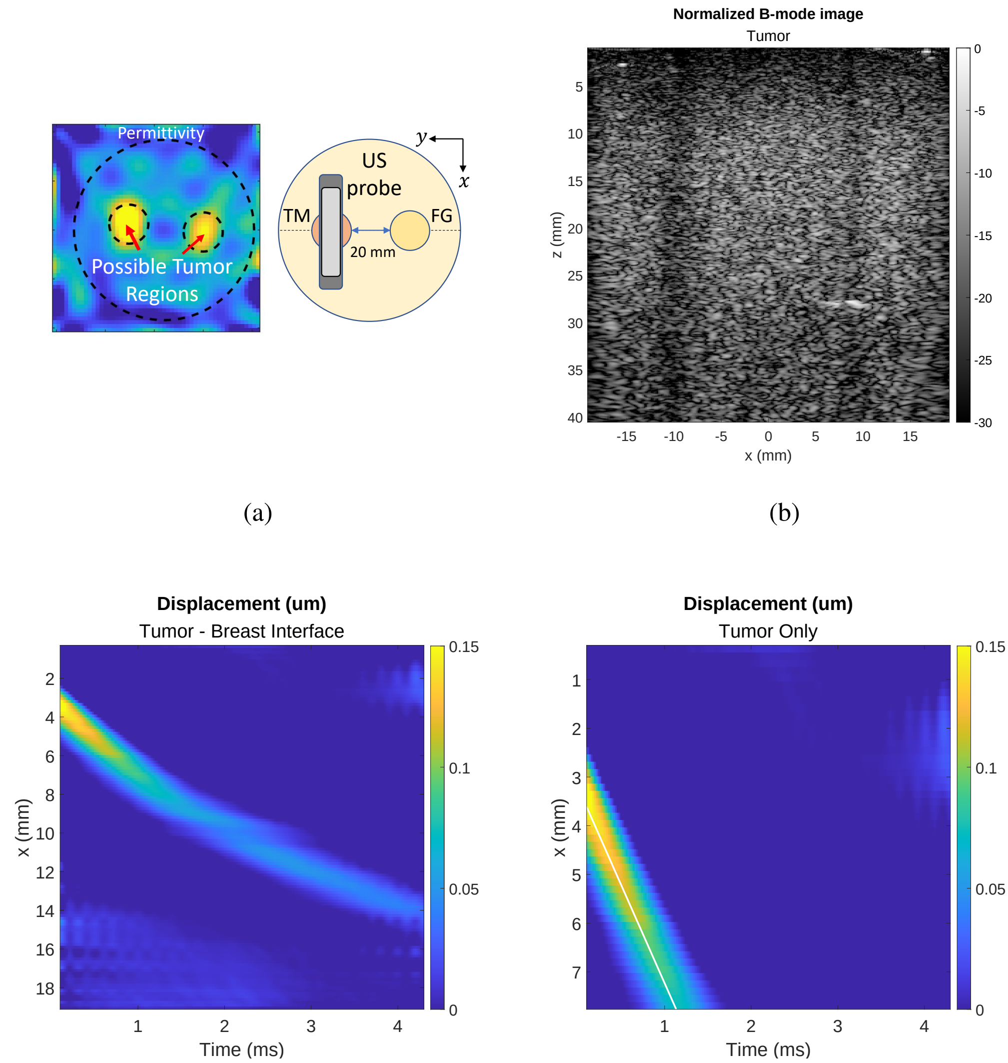

(a) (b) (c) (d)

Figure 5.22: Elasticity measurement results of the multi-modal imaging phantom for the first imaging scenario, see Figure 5.20. (a) The ultrasound (US) probe was positioned on top of the tumor inclusion using the permittivity map obtained from MWI as a prior information. FG is fibroglandular inclusion and TM is the tumor inclusion. (b) The B-mode image of the tumor inclusion. The borderlines of the tumor is visible at x = -10 mm and x = 10 mm. (c) 2D displacement map for the rightward travelling waves. The break point between the tumor and breast around x = 10 mm can be observed. (d) Displacement map for the selected tumor region. Notice that the x positions are different from the positions in (b) and cover only the tumor inclusion. The white line represents the optimal Radon sum trajectory. The shear wave speed was found as 4.02 m/s which corresponds to Young's modulus of **48.5 kPa**.

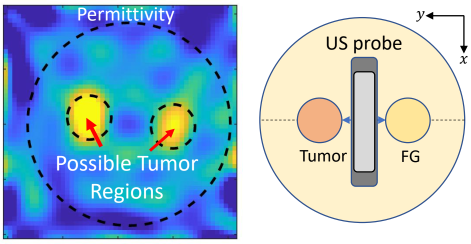

(a)

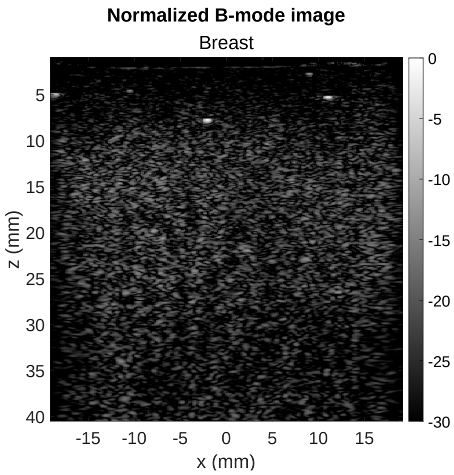

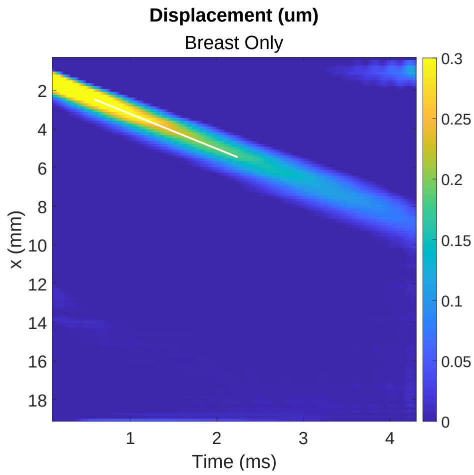

(b) (c)

Figure 5.23: Elasticity measurement results of the multi-modal imaging phantom for the first imaging scenario, see Figure 5.20. (a) The US probe was positioned on top of the breast region using the permittivity map obtained from MWI as a prior information. FG is fibroglandular inclusion. (b) The B-mode image of the breast image. There is no borderlines as in the case of tumor and fibroglandular inclusions. (c) 2D displacement map for the rightward travelling waves. There is no break point since the breast is homogeneous. The white line represents the optimal Radon sum trajectory. The shear wave wave speed was found as 1.8 m/s which corresponds to Young's modulus of **9.8 kPa**.

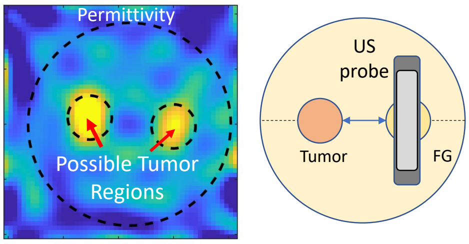

(a)

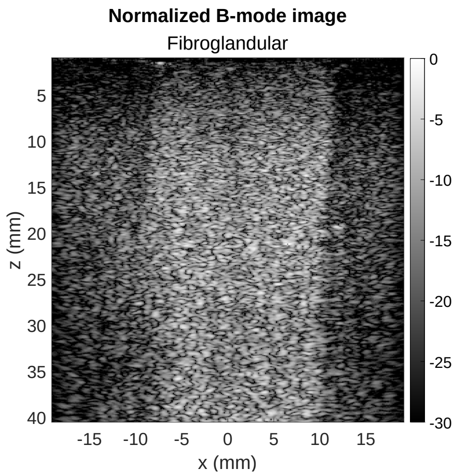

(b)

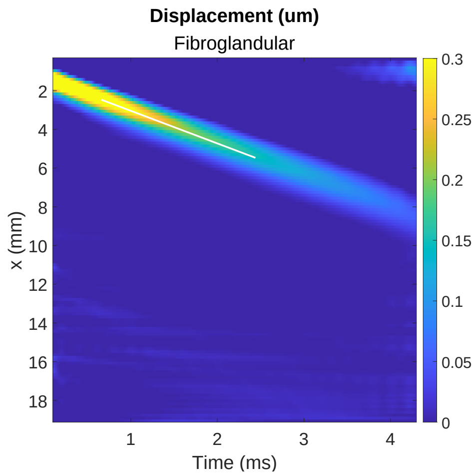

(c)

Figure 5.24: Elasticity measurement results of the multi-modal imaging phantom for the first imaging scenario, see Figure 5.20. (a) The US probe was positioned on top of the fibroglandular inclusion using the permittivity map obtained from MWI as a prior information. (b) The B-mode image of the fibroglandular inclusion. The borderlines of the fibroglandular inclusion is visible at x = -10 mm and x = 10 mm. (c) 2D displacement map for the rightward travelling waves. The white line represents the optimal Radon sum trajectory. The shear wave wave speed was found as 1.68 m/s which corresponds to Young's modulus of **8.5 kPa**. Since the shear wave speeds are close to each other, the slope was not changed in the transition between the fibroglandular and breast tissue.

Table 5.5: Comparison between the actual and measured Young's modulus values of multi-modal imaging phantom (Phantom – 2) for the first scenario (See Figure 5.20) - (a)). The actual values are obtained from phantom measurements.

	Young's Modulus (kPa)	
	Measurement	Actual
Breast Tissue	9.8	12.6
Fibroglandular Tissue	8.5	10.5
Tumor Tissue	48.5	46.7

ues at the tumor region were found as c_s = [3.89 - 3.94] m/s, YM = [45.4 - 46.6] kPa, for the focus depth of [22 - 24] mm, respectively. Similarly, the B-mode image with focus points and the obtained 2D displacement maps for the fibroglandular tissue are presented in Figure 5.26. The shear wave speeds and Young's modulus values of the fibroglandular tissue were found as c_s = [1.58 - 1.56] m/s, YM = [7.48 - 7.30] kPa, for the focus depth of [22 - 24 mm], respectively. The obtained results were tabulated in Table 5.6 together with the reference and first imaging scenario values. The measured and reference values were consistent with each other. In addition, the measured values are close to those obtained in the first imaging scenario where the focus depth was 16 mm. Results showed that, the tumor can be successfully identified using the prior information coming from microwave imaging. Furthermore, shear wave elasticity imaging contributes to the microwave imaging since the fibroglandular tissue which has a similar permittivity to the tumor is shown to have lower stiffness, therefore, it is identified as healthy tissue.

Finally, a summary of the obtained results are presented in Figure 5.27. The quantitative dielectric distribution obtained from microwave imaging has been used as prior input for shear wave imaging. This approach allowed the ultrasound beam to be focused to the targeted tissues, and the quantitative stiffness values (Young's modulus) of the tissues determined. It is shown that the use of multi-modal imaging facilitated quantitative tumor detection, and the results were consistent with reference values.

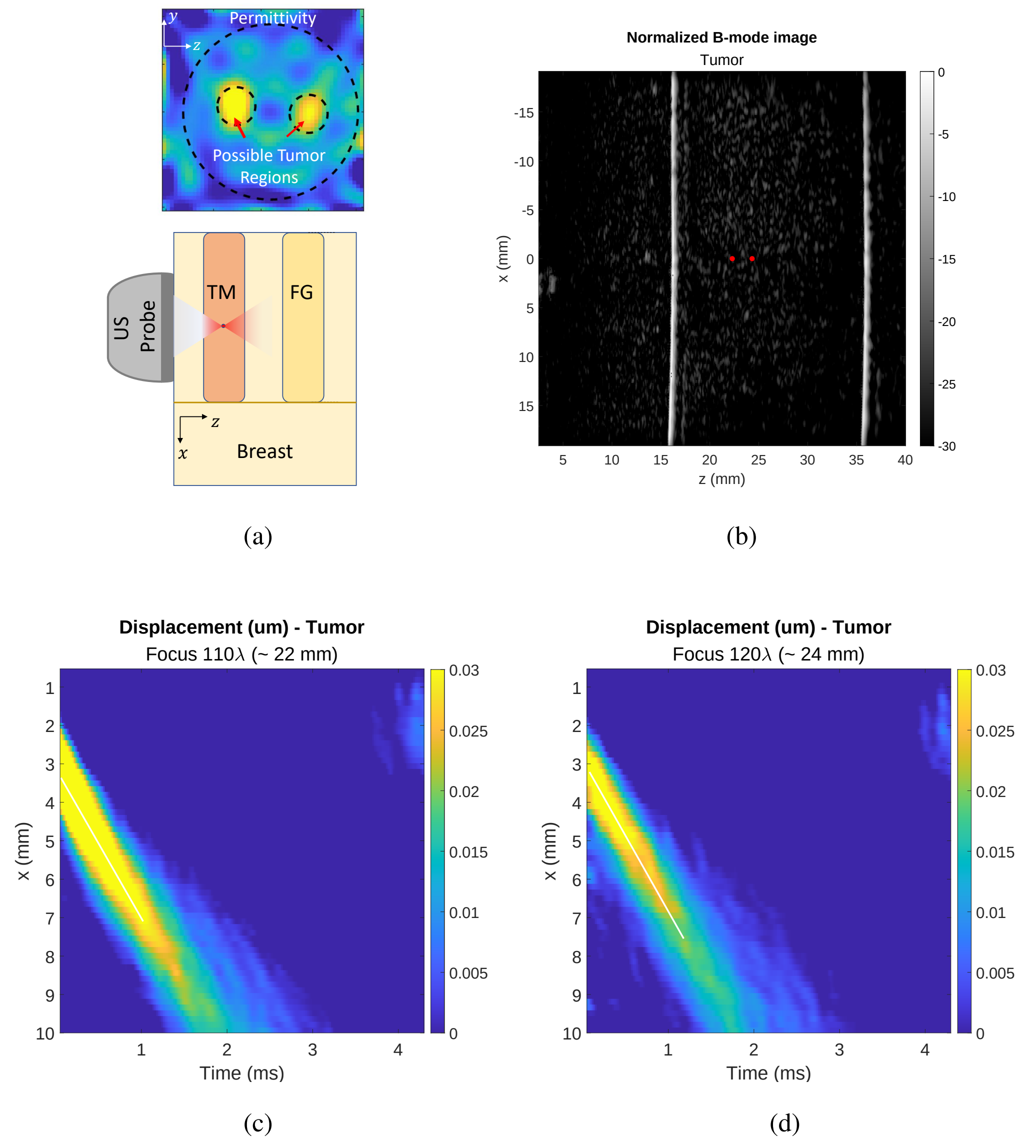

Figure 5.25: Elasticity measurement results of the multi-modal imaging phantom for the second imaging scenario, see Figure 5.20. (a) The US probe was positioned at the left-hand side of phantom and focused on the tumor inclusion using the permittivity map obtained from MWI as a prior information. (b) The B-mode image of the phantom. The borderlines of the tumor is visible at $z \sim 16$ mm and $z \sim 36$ mm. The red dots show the focus locations at 22 mm 24 mm. (c) 2D displacement maps for the focus depth of 22 mm, and (d) 24 mm. The white line represents the optimal Radon sum trajectory. The shear wave speeds were found as c_s = [3.89 - 3.94] m/s, which corresponds to Young's modulus of **YM = [45.4 - 46.6] kPa**, for the focus depth of [22 - 24] mm, respectively.

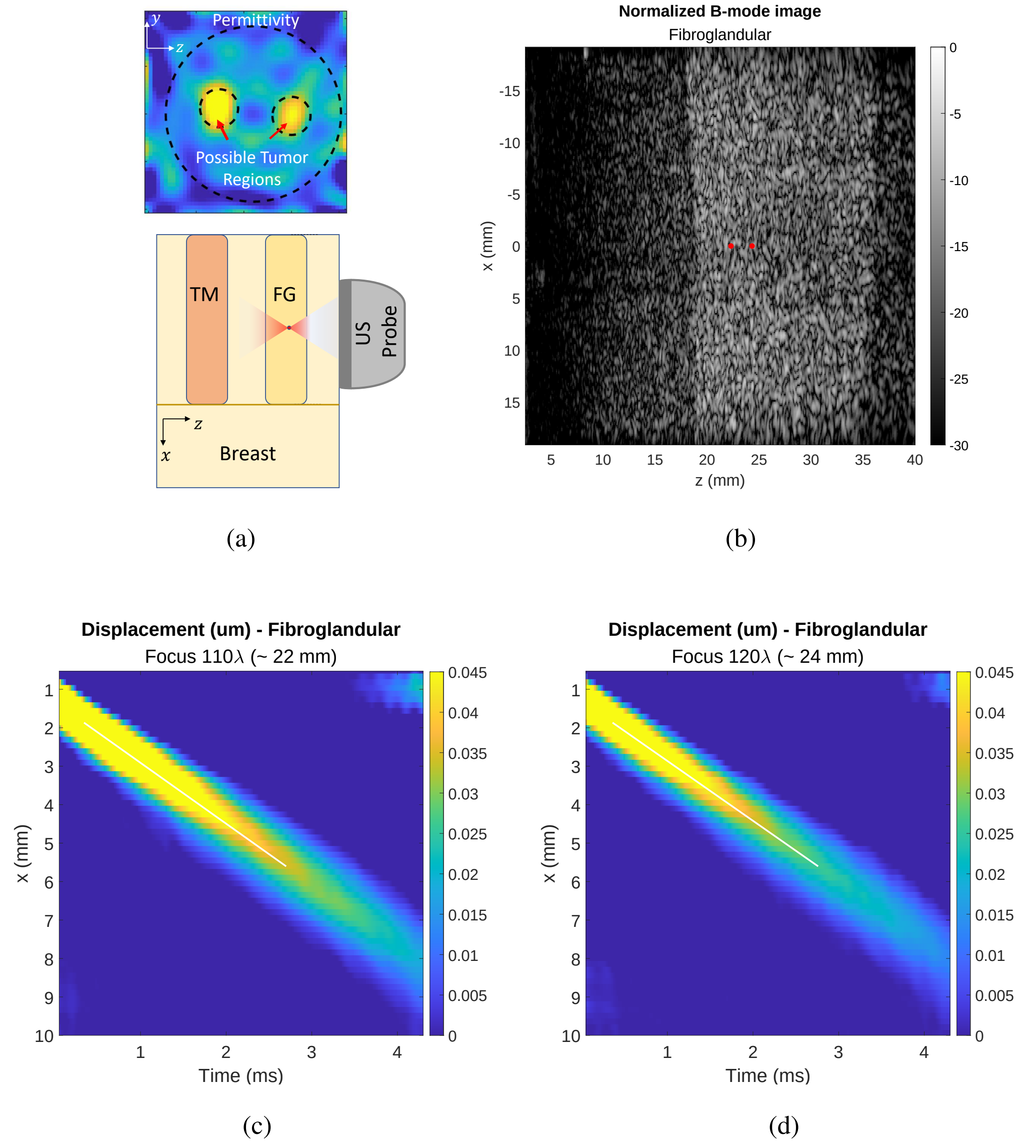

Figure 5.26: Elasticity measurement results of the multi-modal imaging phantom for the second imaging scenario, see Figure 5.20. (a) The US probe was positioned at the right-hand side of phantom and focused on the fibroglandular inclusion using the permittivity map obtained from MWI as a prior information. (b) The B-mode image of the phantom. The borderlines of the fibroglandular inclusion is visible at $z \sim 18$ mm and $z \sim 36$ mm. The red dots show the focus locations at 22 mm, and 24 mm. (c) 2D displacement maps for the focus depth of 22 mm, and (d) 24 mm. The white line represents the optimal Radon sum trajectory. The shear wave speeds were found as c_s = [1.58 - 1.56] m/s, which corresponds to Young's modulus of **YM = [7.48 - 7.30] kPa**, for the focus depth of [22 - 24] mm, respectively.

Table 5.6: Comparison between the actual and measured Young's modulus values of multi-modal imaging phantom (Phantom – 2) at the tumor and fibroglandular region. Imaging scenarios were depicted in Figure 5.20). The actual values are obtained from phantom measurements. z_f is the focus depth of the ultrasound beam.

	Young's Modulus (kPa)		
	First Scenario z_f = 16 mm	Second Scenario z_f = [22 mm - 24 mm]	Actual
Fibroglandular Tissue	8.5	[7.48 - 7.30]	10.5
Tumor Tissue	48.5	[45.4 - 46.6]	46.7

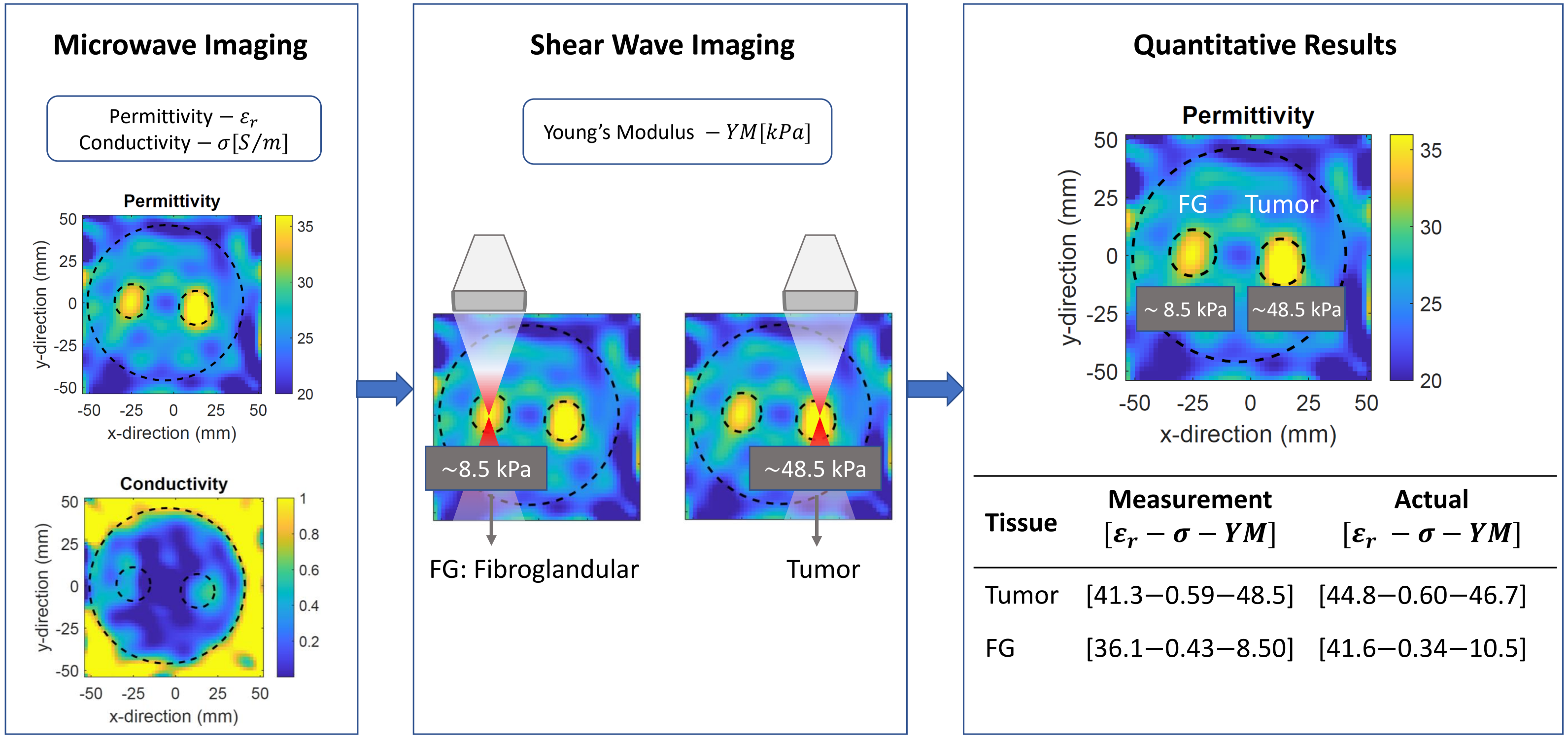

Figure 5.27: The summary of the proposed proposed imaging method and the obtained results. While healthy fibroglandular (FG) and tumor tissues have similar dielectric properties, they differ in elasticity, with the tumor being stiffer than the healthy FG tissues. The quantitative permittivity map obtained from microwave imaging serves as prior information, guiding shear wave to the suspicious tissues. By utilizing the quantitative Young's modulus values obtained from shear wave imaging, breast tumors can be identified. The maximum values of the measured electrical and mechanical parameters were tabulated with the actual values.

5.3 Discussion and Conclusions

5.3.1 Discussion and Conclusions on Microwave Imaging

In this section, experimental study for the microwave imaging is presented. The microwave imaging setup was developed using 16 antennas and the coupling medium. The phantom was inserted into the imaging area and the measurements were taken using 16-channel network analyzer. The measured signals were calibrated and used for the reconstruction. The reconstruction results show that microwave imaging was performed well and the actual data and measurement values are in good agreement.

Even though the reconstruction results and the actual measurements were close to each other, some discrepancies were observed especially in the background breast phantom region, influenced by several factors.

First off all, although measurements were taken in 3D-space, the reconstruction simulations were performed in 2D to reduce computational burden. Therefore, 3D wave propagation effects and reflections from the air/coupling liquid interfaces were not taken into account. In addition, the monopole antennas were modeled as point sources and propagation effects were ignored. Therefore, the radiation characteristics of the antenna was not considered.

Secondly, the measurement system noise caused artifacts in the images. The high conductivity of the coupling liquid has caused the decrease in the received signal especially for the antennas furthest from the transmitter. This may affect the possible region selection for SWEI especially in tissues with low dielectric contrast. In this study, to increase the signal-to-noise ratio, an IF bandwidth of 10 Hz was used, and measurements were taken over 20 samples. The tumor and fibroglandular inclusions with a relative permittivity contrast ($\varepsilon_r^{tumor}/\varepsilon_r^{fibro}$) of 1.08 was successfully identified.

Thirdly, the mismatches between imaging model and the measurement system, and positioning inaccuracies were not taken into account. Since the measurement was made manually, the phantom was not placed exactly perpendicular to the imaging axis, and it was slightly inclined especially for the multi-modal imaging phantom

(Phantom – 2). For the permittivity reconstructions, this caused tumor and fibroglandular inclusions to slightly spread in the images and resulted in decrease in their maximum values to be lower than the actual values.

For reconstructions, the Gauss-Newton based iterative algorithm with Levenberg-Marquardt regularization was used in this thesis. However, imaging performance can be improved with other algorithms. For example, log-phase formulation [95, 127], which involves phase unwrapping and gives more weight to the relative change in the signal level rather than the absolute change, can result in better reconstruction images. In addition, the reconstructions were performed at single frequency. Incorporating multiple frequency information [137]. or using the time domain signals [138] may enhance the accuracy of the reconstructed images.

The reconstruction results for permittivity were better than those for conductivity. Since the contrast in permittivity within tissues is much higher than the contrast in conductivity, changes in conductivity have less impact on the convergence of the results compared to changes in the dielectric constant [189]. This issue is often observed in microwave imaging studies, and efforts are being made to improve it. To enhance conductivity images, a pre-scaling procedure was suggested in [189]. Additionally, a recent study [97] addressed the imbalance between relative permittivity and conductivity reconstructions. By using fraction parameters and weighting the permittivity values, the reconstruction results showed improved conductivity images.

To conclude, it is shown with phantom experiments that the tumor and fibroglandular inclusions can be identified, and their electrical parameter values can be obtained quantitatively using microwave imaging. The results also show that fibroglandular region has lower permittivity ($\varepsilon_r^{fibro} \sim 35$) value than tumor region ($\varepsilon_r^{tumor} \sim 40$). However, low contrast between these values may decrease specificity of microwave imaging for tumor detection. The obtained microwave imaging results can be used as a prior information in shear wave elasticity imaging to achieve a better identification.

5.3.2 Discussion and Conclusions on Shear Wave Elasticity Imaging

In clinical practice, the shear wave imaging method is used together with B-mode ultrasound imaging, which can show suspicious areas [190]. According to the clinical use guidelines for breast ultrasound elastography prepared by the World Federation of Ultrasound in Medicine and Biology (WFUMB) [190], obtaining a good B-mode image is the primary requirement for a good elastography image. Poor B-mode image quality or failure to detect a suspicious area with B-mode can negatively impact elastography results [190]. The second requirement in the WFUMB guidelines is to keep the ultrasound probe perpendicular to the skin. If the probe is not held at the correct angle, shear wave propagation cannot be accurately tracked in the intended area. Moreover, even in the absence of tumors, tissue hardening can occur. For instance, conditions like fat necrosis, fibroadenoma, and fibrocyst can lead to tissue hardening compared to normal tissue [36].

In this thesis study, the contribution of microwave imaging to shear wave imaging is the use of an additional physical parameter (permittivity and conductivity) alongside the B-mode image. This approach provides extra information, allowing for better identification of potential tumor areas.

In the previous section, experimental results for shear wave elasticity imaging was presented. The shear wave elasticity imaging measurements were performed using Verasonics Ultrasound Research System and L11-5V linear ultrasound probe. Obtained ultrasound data was transformed to displacement data using USTB toolbox, then obtained displacement values are post-processed and the shear wave speed is determined. Assuming a linear and elastic material, the Young's modulus values are determined from shear wave speed. The obtained measurement results show that shear wave elasticity imaging was performed well and the actual data and the measurement values are in good agreement.

Although the results shows that the tumor and the fibroglandular tissue can be identified successfully, it would be useful to discuss some factors related to shear wave elasticity imaging.

First of all, the shear wave speed estimations were performed assuming the soft tissues can be modeled as a linear elastic material. However, tissues generally have viscoelastic behaviour, which causes shear waves to disperse and attenuate [191, 192]. This may hinder accurate shear wave speed estimation when using time of flight methods. In the conducted experiments, we have observed the shear waves on the region of interest which was predetermined using the microwave imaging, therefore it was possible to follow shear waves in the relevant area before they propagate far away from the focus and attenuate.

In addition, the prior information from microwave imaging helps to decrease overall scan time for the shear wave elasticity imaging. Since the possible region of interests are identified using microwave imaging, only these regions are imaged without scanning the whole phantom.

Secondly, the displacement data obtained from shear wave elasticity imaging was filtered using a 2D directional filter, which helps to eliminate the reflected waves by selecting only the rightward or leftward propagating waves. However, reflected waves can occur both in and out of the imaging plane. Higher dimensional filters can be used [193] reduce the reflections artifacts leading to improved image reconstructions.

Thirdly, shear wave elasticity imaging measurements were performed at a depth of 16 mm on top of the multi-modal imaging phantom, and at depths of 22 mm and 24 mm on the sides of the multi-modal imaging phantom. The Young's modulus value for the tumor was 48.5 kPa at the 16 mm focusing depth. For the imaging depths of 22 mm and 24 mm, the Young's modulus values were 45.4 kPa and 46.6 kPa, respectively. Measured Young's modulus values were very close to each other but slightly different. This may be caused by reflections occurring at the breast-tumor and breast-fibroglandular interfaces. Note that the effect of the depth of focus on the shear wave speed estimation becomes significant for curvilinear array probes, while the linear probes show little dependence on the focal depth [194]. In this thesis study, we have used linear array ultrasound imaging probe L11-5V.

Finally, the shear wave elasticity imaging measurements suffer from operator dependency. Depending on the applied force to the the transducer during the measurements, and depending on the orientation of the transducer, the shear wave speed estimations may vary [49]. In our multi-modal imaging setup, we propose positioning the ultrasound transducer to the possible tumor regions without operator dependency.

Note that, the elasticity information obtained from shear wave imaging depends on the limitations of the shear wave technique. For example, in heterogeneous materials, reflections at boundary areas can distort the wave shape and make tracking the wave more difficult. The images obtained from different imaging configurations in [162] show that the shear wave images vary based on the wavelength of the applied stimulus, the kernel size used to calculate the shear wave speed, and the method used to determine the wave arrival time [162]. Additionally, the images can differ based on the strategy used for applying and tracking the acoustic radiation force. For instance, in point-SWE, the acoustic radiation force is focused on a single point, which makes it highly affected by heterogeneous distributions and causes the shear waves to quickly decay [190]. Therefore, the WFUMB guidelines recommend avoiding point shear wave imaging for breast tissue scanning, and instead, recommend using 2D-SWE imaging. 2D-SWE methods can vary based on their application techniques. For example, in supersonic shear imaging (SSI) [48, 195], multiple focus points are used, and continuous push pulses are sent to each focus point, producing large amplitude planar shear waves. On the other hand, in the comb-push method [196], multiple focused or unfocused push pulses are transmitted simultaneously or at different times. By tracking the shear waves, 2D shear wave speed maps for a broad distribution area can be obtained. In addition, assessing the quality of the shear waves is an important factor [190]. Despite the tissue being cancerous, it might be misdiagnosed as healthy based on the shear wave speed alone [190]. Therefore, a quality map is created by analyzing the progression characteristics and noise levels of the tracked shear waves.

To conclude, it is shown with the phantom experiments that the tumor and fibroglandular tissues can be identified and their Young's modulus values can be obtained quantitatively using shear wave elasticity imaging. The results showed that the tumor inclusion has a maximum YM value of 48.5 kPa, whereas, the fibroglandular inclusion has a maximum YM value of 8.5 kPa, which are consistent with the reference values (YM^{ref}_{tumor} = 46.7 kPa, YM^{ref}_{fibro} = 10.5 kPa). The YM values were obtained using the microwave imaging results as a prior information and the shear wave speed estimations are carried out only for the possible region of interest, resulting in increase in the accuracy and decrease in the overall scan time.

CHAPTER 6

CONCLUSIONS AND FUTURE WORK

In this thesis study, the potential of a multi-physics, multi-modal imaging technique that combines microwave and shear wave elasticity imaging to enhance breast cancer diagnosis was presented. The method is based on the dielectric and mechanical properties of the malignant and healthy tissues.

In this method, initially, microwave imaging is conducted to identify potential regions of interest for tumor detection. Subsequently, using the quantitative dielectric distribution map from the microwave imaging as prior information, shear wave elasticity imaging is applied to the suspicious tissues, to obtain quantitative Young's modulus values.

Using both microwave and shear wave elasticity imaging methods together, as proposed, improves their imaging performance by compensating for each method's limitations and providing complementary information. The combination of shear and microwave imaging offers advantages over utilizing either microwave imaging or shear wave elasticity imaging alone. The advantages can be listed as follows:

1) Obtaining quantitative data for electrical and mechanical parameters

Evaluating quantitative electrical and mechanical parameters data together provides more information compared to using only one method. Additionally, acquiring quantitative information not only improves diagnostic accuracy but also provides details relevant to the staging of the tumor and allows for monitoring during treatment phases.

2) Improving the imaging performance of the MWI for low-contrast scenarios

Studies on the dielectric properties of tissues have shown that the dielectric contrast between healthy and malignant tissues can be low in dense breast tissues. Consequently, microwave imaging alone may not be sufficient for diagnosis. On the other hand, shear wave imaging is capable of identifying tissues by using the elastic contrast between them. Therefore, by integrating information from shear wave elasticity imaging, tumors that might not be detected by microwave imaging alone can be identified.

3) Improving the imaging performance of the SWEI

The imaging performance of the shear wave imaging depends on successful generation of acoustic radiation force in the tissue and accurate tracking the propagated shear waves. Therefore, it is important that the acoustic radiation force is minimally influenced by the operator, accurately focused, and resulting shear waves are properly tracked. The additional information obtained from microwave imaging, together with the B-mode image, assists in directing ultrasound to potential areas of the tumor. Therefore, this approach can enhance the accuracy of Young's modulus estimation.

4) Non-invasive, patient friendly and cost-effective breast screening

Both microwave and shear wave elasticity imaging are non-invasive, non-ionizing techniques, making them safe for patients. In addition, the multi model use of shear wave and microwave imaging method is cost effective compared to previously suggested multi-modal MRI or computed ultrasound tomography methods. Since shear wave elasticity imaging is already used in clinical settings, the integration of the microwave imaging systems seems feasible.

In this thesis study, numerical simulations conducted for microwave imaging were presented. Using 2D FDTD method, the forward problem was solved and compared with the analytical results. In the inverse problem, nonlinear minimization problem was solved through an iterative process using Gauss-Newton method with Levenberg-Marquardt regularization. A simple 2D cylindrical target with a diameter of 20 mm and electrical parameters of $\varepsilon_{r,t} = 45$, $\sigma_t = 2$ S/m was illuminated by 16 antennas at 1.5 GHz. The background medium with electrical parameters $\varepsilon_{r,b} = 20$, $\sigma_b = 1.3$ S/m was used for the simulations and the quantitative reconstruction results were provided. Both location and the dielectric properties of the object were reconstructed well, verifying that the problem is formulated and solved correctly. It is observed that due to the smoothing effect of the regularization algorithm at the edges, the numerically reconstructed values were slightly higher than actual values. The maximum value of the reconstructed permittivity was 49. The relative error was $err \sim 0.09$. The relative error was calculated using the formula $err = |\varepsilon_{true} - \varepsilon_{recon}^{max}|/|\varepsilon_{true}|$, where ε_{true} is the relative permittivity of the actual data, and $\varepsilon_{recon}^{max}$ is the maximum relative permittivity of the reconstructed data.

In addition, in the solution of the inverse problem imaging for microwave imaging, the different applications of the adjoint method in microwave imaging investigated in detail. Clear and concise analytical expressions for the adjoint formulations were provided in a unified manner, filling a gap in existing literature where such formulations are predominantly presented based on specific applied problems. The update direction calculations were classified into two groups: the *direct* and the *indirect* methods and the mathematical derivations for each group were presented independent of the forward solution method. The resulting analytical expressions were verified through numerical simulations, and the computational loads were measured in terms of the number of forward simulation runs. The results have demonstrated the differences between various applications of the adjoint method and have shown the computational efficiency that can be achieved through the proper strategy. In an imaging configuration where N_s and N_r represent the number of source and receiver antennas, respectively, using the *direct* approach to calculate the derivative of the cost function requires $2 \times N_s$ forward simulations. On the other hand, the *indirect* approach requires $N_s + N_r$ forward simulations. However, due to the reciprocity principle, transmitters and receivers can be used interchangeably. Therefore, the number of forward simulations for the *indirect* method reduces to $[N_s + N_r - (N_s \cap N_r)]$, where $(N_s \cap N_r)$ is the number of transceivers. The *indirect* method is more efficient when $[N_s + N_r - (N_s \cap N_r)] < [2 \times N_s]$, simplifying to $N_s > [N_r - (N_s \cap N_r)]$. In microwave imaging, where antennas act as both transmitters and receivers ($N_s = N_r = N$ and $(N_s \cap N_r) = N$), the *direct* and *indirect* methods require $2 \times N$ and N forward solutions, respectively. Therefore, the *indirect* method, requiring half the number of forward solutions, is computationally advantageous in microwave imaging scenarios.

In addition to microwave imaging, numerical tools were developed for shear wave elasticity imaging. In the forward problem, the velocity-stress equations were discretized in time domain and solved using 2D FDTD. Obtained results were verified with the simulations conducted using commercial multiphysics software COMSOL 5.6. In the inverse problem, an imaging scenario where the Young's modulus of the background medium was 15 kPa were considered. Target with a stiffness value of 60 kPa was modeled as a cylindrical inclusion with a diameter of 10 mm and imaged through scanning of the ultrasound focus at different depths, from -6 mm to 6 mm with 2 mm steps. The acoustic radiation force was applied in the axial direction and was modeled as Gaussian waveform in both time and space domain. Obtained displacement values were filtered using directional filter and the time-of-flight method, namely time-to-peak-slope, was used to determine shear wave speed. The Young's modulus values reconstructed quantitatively for the imaged region were nearly 60 kPa and consistent with the actual data. Some artifacts were observed in the reconstructed image due to the reflections from the edges of the tumor.

For experimental studies, tissue phantoms that mimic the electrical and mechanical properties of the breast tissue were developed. Measured permittivity, conductivity, and Young's modulus values of the phantoms showed good agreement with the reference values. Two breast tissue phantoms are developed for the experiments, one for microwave imaging and one for multi-modal imaging, each containing fibroglandular tissue and tumor inclusions with a diameter of 20 mm.

To demonstrate the feasibility of the applied method, both microwave imaging and shear wave imaging experiments were conducted. A microwave imaging setup consisting of 16 circularly positioned monopole antennas was developed. In experiments, imaging area was filled with glycerin-water mixture of coupling liquid to maximize the energy that couples to object, and to eliminate the multi-path signals. Developed breast phantoms were measured inside the coupling liquid. The measurements were performed using 16-channel network analyzer. Obtained S-parameter values were converted to electric field an the used in the reconstruction algorithm. The reconstructed quantitative permittivity images of the developed breast phantoms at different positions and rotations were presented. For the experiments performed using multi-modal imaging phantom (phantom-2) , the maximum value of the tumor and fibroglandular inclusions were measured as 41.3 and 36.04 respectively. The results were found consistent with the measured reference permittivity values for the tumor and fibroglandular tissues ($\varepsilon^{ref}_{r_{tumor}}$ = 44.8 and $\varepsilon^{ref}_{r_{fibro}}$ = 41.58). The relative error values were found as $err_{tumor} \sim 0.08$ and $err_{fibro} \sim 0.13$ for the tumor and fibroglandular inclusions, respectively.

The quantitative permittivity map obtained from microwave imaging was utilized as prior information, guiding shear wave imaging to the suspicious tissues. The shear wave imaging experiments were conducted using Verasonics Vantage Research Ultrasound system and L11-5V linear ultrasound probe. Obtained ultrasound data was transformed to displacement data using USTB toolbox, then obtained displacement values are post-processed, resulting in quantitative YM values. The maximum YM values of the tumor and fibroglandular inclusions were found as 48.5 kPa and 8.5 kPa, respectively, which are consistent with the measured reference values ($\mathrm{YM}^{ref}_{tumor}$ = 46.7 kPa, $\mathrm{YM}^{ref}_{fibro}$ = 10.5 kPa). The relative error values were found as $err^{\mathrm{YM}}_{tumor} \sim 0.04$ and $err^{\mathrm{YM}}_{fibro} \sim 0.23$ for the tumor and fibroglandular inclusions, respectively.

To conclude, it is shown with the phantom experiments that using the quantitative dielectric distribution map from the microwave imaging as prior information and applying shear wave elasticity imaging to the the suspicious tissues, facilitated to obtain quantitative electrical and mechanical parameters.

This thesis presented the preliminary research on the multi-model imaging method proposed for breast cancer detection through the utilization of the microwave and shear wave elasticity imaging. The performance of the imaging method can be further enhanced with the further studies:

1. Development of rapid and efficient computational tools for solving the microwave imaging forward problem in 3D scenarios.
2. Examining the impact of different algorithms on image reconstruction performance of the microwave imaging and incorporating multiple frequency or time-domain signals into the reconstruction algorithms.
3. Investigation of the performance of different shear wave imaging methods such as supersonic shear imaging (SSI) [195] and combpush ultrasound shear elastography (CUSE) [196]).

4. Conducting simulations with realistic tissue models.

5. Performing experimental studies with 3D phantoms.

6. Using the B-mode ultrasound images obtained from shear wave imaging as a morphological background for microwave imaging reconstruction.

7. Integrating information from both imaging methods into the reconstruction algorithm to achieve joint inversion.

REFERENCES

[1] S. D. Meo, A. Cannatà, S. Morganti, G. Matrone, and M. Pasian, "On the dielectric and mechanical characterization of tissue-mimicking breast phantoms," *Physics in Medicine Biology*, vol. 67, p. 155018, jul 2022.

[2] S. Di Meo, P. Espin-Lopez, A. Martellosio, M. Pasian, M. Bozzi, L. Peregrini, A. Mazzanti, F. Svelto, P. Summers, G. Renne, L. Preda, and M. Bellomi, "Experimental validation of the dielectric permittivity of breast cancer tissues up to 50 GHz," in *2017 IEEE MTT-S International Microwave Workshop Series on Advanced Materials and Processes for RF and THz Applications (IMWS-AMP)*, pp. 1–3, 2017.

[3] Y. Kuwahara and A. Malik, "Microwave imaging for early breast cancer detection," *New Perspect. Breast Imaging*, pp. 45–71, 2017.

[4] World Health Organization, "Breast cancer." https://www.who.int/newsroom/fact-sheets/detail/breast-cancer, 2020. [Online; accessed 16-July-2024].

[5] A. Modiri, S. Goudreau, A. Rahimi, and K. Kiasaleh, "Review of breast screening: toward clinical realization of microwave imaging," *Medical Physics*, vol. 44, no. 12, pp. e446–e458, 2017.

[6] L. Wang, "Microwave imaging and sensing techniques for breast cancer detection," *Micromachines*, vol. 14, no. 7, p. 1462, 2023.

[7] J.-C. Bolomey, "Crossed viewpoints on microwave-based imaging for medical diagnosis: From genesis to earliest clinical outcomes," *The World of Applied Electromagnetics*, pp. 369–414, 2018.

[8] S. Gabriel, R. Lau, and C. Gabriel, "The dielectric properties of biological tissues: II. measurements in the frequency range 10 Hz to 20 GHz," *Physics in Medicine & Biology*, vol. 41, no. 11, p. 2251, 1996.

[9] M. Lazebnik, D. Popovic, L. McCartney, C. B. Watkins, M. J. Lindstrom, J. Harter, S. Sewall, T. Ogilvie, A. Magliocco, T. M. Breslin, *et al.*, "A large-scale study of the ultrawideband microwave dielectric properties of normal, benign and malignant breast tissues obtained from cancer surgeries," *Physics in Medicine & Biology*, vol. 52, no. 20, p. 6093, 2007.

[10] M. Lazebnik, L. McCartney, D. Popovic, C. B. Watkins, M. J. Lindstrom, J. Harter, S. Sewall, A. Magliocco, J. H. Booske, M. Okoniewski, *et al.*, "A large-scale study of the ultrawideband microwave dielectric properties of normal breast tissue obtained from reduction surgeries," *Physics in Medicine & Biology*, vol. 52, no. 10, p. 2637, 2007.

[11] S. Di Meo, P. F. Espin-Lopez, A. Martellosio, M. Pasian, M. Bozzi, L. Perregrini, A. Mazzanti, F. Svelto, P. E. Summers, G. Renne, L. Preda, and M. Bellomi, "Dielectric properties of breast tissues: Experimental results up to 50 GHz," in *12th European Conference on Antennas and Propagation (EuCAP 2018)*, pp. 1–5, 2018.

[12] N. K. Nikolova, *Introduction to microwave imaging*. Cambridge University Press, 2017.

[13] M. Pastorino and A. Randazzo, *Microwave imaging methods and applications*. Artech House, 2018.

[14] S. Noghanian, A. Sabouni, T. Desell, and A. Ashtari, *Microwave tomography: global optimization, prallelization and performance evaluation*. Springer New York, 2014.

[15] D. O'Loughlin, M. O'Halloran, B. M. Moloney, M. Glavin, E. Jones, and M. A. Elahi, "Microwave breast imaging: Clinical advances and remaining challenges," *IEEE Transactions on Biomedical Engineering*, vol. 65, no. 11, pp. 2580–2590, 2018.

[16] R. C. Conceição, J. J. Mohr, M. O'Halloran, and et al, *An introduction to microwave imaging for breast cancer detection*. Springer, 2016.

[17] M. Savazzi, O. Karadima, D. O. R. Duarte, J. Tobon Vasquez, F. Vipiana, P. Kosmas, C. A. Fernandes, J. M. Felício, and R. C. Conceição, "Experimen-

tal assessment of axillary lymph node microwave tomography using anthropomorphic phantoms," *IEEE Journal of Electromagnetics, RF and Microwaves in Medicine and Biology*, vol. 7, no. 2, 2023.

[18] M. A. Aldhaeebi, K. Alzoubi, T. S. Almoneef, S. M. Bamatraf, H. Attia, and O. M. Ramahi, "Review of microwaves techniques for breast cancer detection," *Sensors*, vol. 20, no. 8, 2020.

[19] N. AlSawaftah, S. El-Abed, S. Dhou, and A. Zakaria, "Microwave imaging for early breast cancer detection: current state, challenges, and future directions," *Journal of Imaging*, vol. 8, no. 5, 2022.

[20] A. Janjic, M. Cayoren, I. Akduman, T. Yilmaz, E. Onemli, O. Bugdayci, and M. E. Aribal, "SAFE: A novel microwave imaging system design for breast cancer screening and early detection—clinical evaluation," *Diagnostics*, vol. 11, no. 3, 2021.

[21] O. Ozgun and M. Kuzuoglu, "Coordinate transformation aided finite element method for contour detection of breast tumors in microwave imaging," *International Journal for Numerical Methods in Biomedical Engineering*, vol. 34, no. 10, 2018.

[22] L. Guo, A. S. M. Alqadami, and A. Abbosh, "Stroke diagnosis using microwave techniques: review of systems and algorithms," *IEEE Journal of Electromagnetics, RF and Microwaves in Medicine and Biology*, vol. 7, no. 2, pp. 122–135, 2023.

[23] T. Henriksson, S. Sahebdivan, R. Planas, C. Brunner, L. Kellermair, M. Guger, W. Struhal, P. Fuchs, J. Reichl, A. Stelzer, S. Semenov, S. Pearce, and M. R. Vosko, "Human brain imaging by electromagnetic tomography: a mobile brain scanner for clinical settings," *2022 16th European Conference on Antennas and Propagation (EuCAP)*, 2022.

[24] O. Karadima, M. Rahman, I. Sotiriou, N. Ghavami, P. Lu, S. Ahsan, and P. Kosmas, "Experimental validation of microwave tomography with the DBIM-TwIST algorithm for brain stroke detection and classification," *Sensors*, vol. 20, no. 3, 2020.

[25] A. Fhager, S. Candefjord, M. Elam, and M. Persson, "Microwave diagnostics ahead: saving time and the lives of trauma and stroke patients," *IEEE Microwave Magazine*, vol. 19, no. 3, pp. 78–90, 2018.

[26] P.-H. Tournier, M. Bonazzoli, V. Dolean, F. Rapetti, F. Hecht, F. Nataf, I. Aliferis, I. El Kanfoud, C. Migliaccio, M. de Buhan, M. Darbas, S. Semenov, and C. Pichot, "Numerical modeling and high-speed parallel computing: new perspectives on tomographic microwave imaging for brain stroke detection and monitoring," *IEEE Antennas and Propagation Magazine*, vol. 59, no. 5, pp. 98–110, 2017.

[27] M. Hopfer, R. Planas, A. Hamidipour, T. Henriksson, and S. Semenov, "Electromagnetic tomography for detection, differentiation, and monitoring of brain stroke: A virtual data and human head phantom study," *IEEE Antennas and Propagation Magazine*, vol. 59, no. 5, pp. 86–97, 2017.

[28] X. Chen, *Computational methods for electromagnetic inverse scattering*. John Wiley & Sons Singapore Pte. Ltd, May 2018.

[29] T. Reimer and S. Pistorius, "Review and analysis of tumour detection and image quality analysis in experimental breast microwave sensing," *Sensors*, vol. 23, no. 11, p. 5123, 2023.

[30] K. J. Parker, M. M. Doyley, and D. J. Rubens, "Imaging the elastic properties of tissue: the 20 year perspective," *Physics in Medicine & Biology*, vol. 56, no. 1, p. R1, 2010.

[31] A. Sarvazyan, T. J Hall, M. W Urban, M. Fatemi, S. R Aglyamov, and B. S Garra, "An overview of elastography-an emerging branch of medical imaging," *Current Medical Imaging*, vol. 7, no. 4, pp. 255–282, 2011.

[32] J. R. Doherty, G. E. Trahey, K. R. Nightingale, and M. L. Palmeri, "Acoustic radiation force elasticity imaging in diagnostic ultrasound," *IEEE Transactions on Ultrasonics, Ferroelectrics, and Frequency Control*, vol. 60, no. 4, pp. 685–701, 2013.

[33] M. Palmeri, M. Wang, J. Dahl, K. Frinkley, and K. Nightingale, "Quantifying

hepatic shear modulus in vivo using acoustic radiation force," *Ultrasound in Medicine & Biology*, vol. 34, no. 4, pp. 546–558, 2008.

[34] N. G. Ramião, P. S. Martins, R. Rynkevic, A. A. Fernandes, M. Barroso, and D. C. Santos, "Biomechanical properties of breast tissue, a state-of-the-art review," *Biomechanics and Modeling in Mechanobiology*, vol. 15, pp. 1307–1323, 2016.

[35] T. A. Krouskop, T. M. Wheeler, F. Kallel, B. S. Garra, and T. Hall, "Elastic moduli of breast and prostate tissues under compression," *Ultrasonic Imaging*, vol. 20, no. 4, pp. 260–274, 1998.

[36] A. Samani and D. Plewes, "An inverse problem solution for measuring the elastic modulus of intact ex vivo breast tissue tumours," *Physics in Medicine & Biology*, vol. 52, no. 5, p. 1247, 2007.

[37] T. Umemoto, E. Ueno, T. Matsumura, M. Yamakawa, H. Bando, T. Mitake, and T. Shiina, "Ex vivo and in vivo assessment of the non-linearity of elasticity properties of breast tissues for quantitative strain elastography," *Ultrasound in Medicine & Biology*, vol. 40, no. 8, pp. 1755–1768, 2014.

[38] A. Srivastava, Y. Verma, K. Rao, and P. Gupta, "Determination of elastic properties of resected human breast tissue samples using optical coherence tomographic elastography," *Strain*, vol. 47, no. 1, pp. 75–87, 2011.

[39] S. Kruse, J. Smith, A. Lawrence, M. Dresner, A. Manduca, J. F. Greenleaf, and R. L. Ehman, "Tissue characterization using magnetic resonance elastography: preliminary results," *Physics in Medicine & Biology*, vol. 45, no. 6, p. 1579, 2000.

[40] R. M. Sigrist, J. Liau, A. El Kaffas, M. C. Chammas, and J. K. Willmann, "Ultrasound elastography: review of techniques and clinical applications," *Theranostics*, vol. 7, no. 5, p. 1303, 2017.

[41] A. Tang, G. Cloutier, N. M. Szeverenyi, and C. B. Sirlin, "Ultrasound elastography and MR elastography for assessing liver fibrosis: part 1, principles and techniques," *American Journal of Roentgenology*, vol. 205, no. 1, pp. 22–32, 2015.

[42] R. G. Barr, G. Ferraioli, M. L. Palmeri, Z. D. Goodman, G. Garcia-Tsao, J. Rubin, B. Garra, R. P. Myers, S. R. Wilson, D. Rubens, *et al.*, "Elastography assessment of liver fibrosis: society of radiologists in ultrasound consensus conference statement," *Radiology*, vol. 276, no. 3, pp. 845–861, 2015.

[43] K. Nightingale, "Acoustic radiation force impulse (ARFI) imaging: a review," *Current Medical Imaging*, vol. 7, no. 4, pp. 328–339, 2011.

[44] J. Bamber, D. Cosgrove, C. F. Dietrich, J. Fromageau, J. Bojunga, F. Calliada, V. Cantisani, J.-M. Correas, M. D'Onofrio, E. Drakonaki, *et al.*, "EFSUMB guidelines and recommendations on the clinical use of ultrasound elastography. part 1: Basic principles and technology," *Ultraschall in der Medizin-European Journal of Ultrasound*, vol. 34, no. 02, pp. 169–184, 2013.

[45] D. Cosgrove, F. Piscaglia, J. Bamber, J. Bojunga, J.-M. Correas, O. a. Gilja, A. Klauser, I. Sporea, F. Calliada, V. Cantisani, *et al.*, "EFSUMB guidelines and recommendations on the clinical use of ultrasound elastography. part 2: Clinical applications," *Ultraschall in der Medizin-European Journal of Ultrasound*, vol. 34, no. 03, pp. 238–253, 2013.

[46] L. Chen, J. He, G. Liu, K. Shao, M. Zhou, B. Li, and X. Chen, "Diagnostic performances of shear-wave elastography for identification of malignant breast lesions: a meta-analysis," *Japanese Journal of Radiology*, vol. 32, pp. 592–599, 2014.

[47] A. Feldmann, C. Langlois, M. Dewailly, E. F. Martinez, L. Boulanger, O. Kerdraon, and N. Faye, "Shear wave elastography (SWE): an analysis of breast lesion characterization in 83 breast lesions," *Ultrasound in Medicine & Biology*, vol. 41, no. 10, pp. 2594–2604, 2015.

[48] N. Nitta, M. Yamakawa, H. Hachiya, and T. Shiina, "A review of physical and engineering factors potentially affecting shear wave elastography," *Journal of Medical Ultrasonics*, vol. 48, no. 4, pp. 403–414, 2021.

[49] A. I. Alrashed and A. M. Alfuraih, "Reproducibility of shear wave elastography among operators, machines, and probes in an elasticity phantom," *Ultrasonography*, vol. 40, no. 1, p. 158, 2021.

[50] J. Gu, E. C. Polley, R. Ternifi, R. Nayak, J. C. Boughey, R. T. Fazzio, M. Fatemi, and A. Alizad, "Individualized-thresholding shear wave elastography combined with clinical factors improves specificity in discriminating breast masses," *The breast*, vol. 54, pp. 248–255, 2020.

[51] Y. Deng, M. L. Palmeri, N. C. Rouze, S. J. Rosenzweig, M. F. Abdelmalek, and K. R. Nightingale, "Analyzing the impact of increasing mechanical index and energy deposition on shear wave speed reconstruction in human liver," *Ultrasound in Medicine & Biology*, vol. 41, no. 7, pp. 1948–1957, 2015.

[52] G. Boverman, C. E. L. Davis, S. D. Geimer, and P. M. Meaney, "Image registration for microwave tomography of the breast using priors from nonsimultaneous previous magnetic resonance images," *IEEE Journal of Electromagnetics, RF and Microwaves in Medicine and Biology*, vol. 2, no. 1, pp. 2–9, 2018.

[53] A. H. Golnabi, P. M. Meaney, S. D. Geimer, and K. D. Paulsen, "3-D Microwave tomography using the soft prior regularization technique: evaluation in anatomically realistic MRI-derived numerical breast phantoms," *IEEE Transactions on Biomedical Engineering*, vol. 66, pp. 2566–2575, Sept. 2019.

[54] P. M. Meaney, Z. Kordiboroujeni, G. Player, A. Golnabi, X. Yang, T. Eastlake, and K. D. Paulsen, "MR/Microwave tomography integrated breast cancer imaging," in *2024 18th European Conference on Antennas and Propagation (EuCAP)*, pp. 1–4, 2024.

[55] N. Abdollahi, D. Kurrant, P. Mojabi, M. Omer, E. Fear, and J. LoVetri, "Incorporation of ultrasonic prior information for improving quantitative microwave imaging of breast," *IEEE Journal on Multiscale and Multiphysics Computational Techniques*, vol. 4, pp. 98–110, 2019.

[56] N. Bayat, P. Mojabi, J. LoVetri, and P. Mojabi, "On microwave breast imaging with ultrasound spatial priors," in *2020 XXXIIIrd General Assembly and Scientific Symposium of the International Union of Radio Science*, pp. 1–4, 2020.

[57] Y. Qin, T. Rodet, M. Lambert, and D. Lesselier, "Joint inversion of electromagnetic and acoustic data with edge-preserving regularization for breast

imaging," *IEEE Transactions on Computational Imaging*, vol. 7, pp. 349–360, 2021.

[58] H. Fogel, M. Hughson, M. Asefi, I. Jeffrey, and J. LoVetri, "Generation of prior information in a dual-mode microwave-ultrasound breast imaging system," *Sensors*, vol. 22, no. 18, p. 7087, 2022.

[59] C. B. Top, A. K. Tafreshi, and N. G. Gençer, "Microwave sensing of acoustically induced local harmonic motion: Experimental and simulation studies on breast tumor detection," *IEEE Transactions on Microwave Theory and Techniques*, vol. 64, no. 11, pp. 3974–3986, 2016.

[60] S. D. Meo, L. Pasotti, E. Lashkevich, G. Magenes, M. Pasian, and G. Matrone, "Combining millimeter-wave imaging, ultrasound and elastography in a new multimodal approach for breast cancer detection: Initial experimental results," in *2020 42nd Annual International Conference of the IEEE Engineering in Medicine Biology Society (EMBC)*, pp. 1807–1810, 2020.

[61] H. Jiang, C. Li, D. Pearlstone, and L. L. Fajardo, "Ultrasound-guided microwave imaging of breast cancer: Tissue phantom and pilot clinical experiments," *Medical Physics*, vol. 32, no. 8, pp. 2528–2535, 2005.

[62] M. Omer, P. Mojabi, D. Kurrant, J. LoVetri, and E. Fear, "Proof-of-concept of the incorporation of ultrasound-derived structural information into microwave radar imaging," *IEEE Journal on Multiscale and Multiphysics Computational Techniques*, vol. 3, pp. 129–139, 2018.

[63] X. Song, M. Li, F. Yang, S. Xu, and A. Abubakar, "Study on joint inversion algorithm of acoustic and electromagnetic data in biomedical imaging," *IEEE Journal on Multiscale and Multiphysics Computational Techniques*, vol. 4, pp. 2–11, 2019.

[64] P. Mojabi, M. Hughson, V. Khoshdel, I. Jeffrey, and J. LoVetri, "CNN for compressibility to permittivity mapping for combined ultrasound-microwave breast imaging," *IEEE Journal on Multiscale and Multiphysics Computational Techniques*, vol. 6, pp. 62–72, 2021.

[65] C. B. Top and N. G. Gençer, "Harmonic motion microwave doppler imaging: A simulation study using a simple breast model," *IEEE Transactions on Medical Imaging*, vol. 33, no. 2, pp. 290–300, 2014.

[66] C. B. Top and N. G. Gençer, "Simulation of the scattered field from a vibrating tumor inside the tissue using 3D-FDTD method," *IEEE Microwave and Wireless Components Letters*, vol. 23, no. 6, pp. 273–275, 2013.

[67] U. İrgin, C. B. Top, A. K. Tafreshi, and N. G. Gencer, "Received signal in harmonic motion microwave doppler imaging as a function of tumor position in a 3D scheme," in *2017 11th International Symposium on Medical Information and Communication Technology (ISMICT)*, pp. 86–90, 2017.

[68] A. K. Tafreshi, C. B. Top, and N. G. Gençer, "Two-dimensional multi-frequency imaging of a tumor inclusion in a homogeneous breast phantom using the harmonic motion doppler imaging method," *Physics in Medicine & Biology*, vol. 62, no. 12, p. 4852, 2017.

[69] İrgin, C. B. Top, D. A. Soydan, and N. G. Gençer, "Enhancing the sensitivity of harmonic motion microwave doppler imaging using main signal cancellation circuit," in *12th European Conference on Antennas and Propagation (EuCAP 2018)*, pp. 1–5, 2018.

[70] İrgin, C. B. Top, and N. G. Gençer, "The effect of contrasts in electrical and mechanical properties between breast tissues on harmonic motion microwave doppler imaging signal," *IEEE Journal of Electromagnetics, RF and Microwaves in Medicine and Biology*, vol. 5, no. 4, pp. 362–370, 2021.

[71] D. A. Soydan, İrgin, C. B. Top, and N. G. Gençer, "An improved receiver for harmonic motion microwave doppler imaging," in *2020 14th European Conference on Antennas and Propagation (EuCAP)*, pp. 1–5, 2020.

[72] K. Talaga, "Combined microwave, ultrasound and strain imaging for breast tissue characterization," Master's Thesis, University of Calgary, Canada, 2022.

[73] P. M. Meaney, P. A. Kaufman, L. S. Muffly, M. Click, S. P. Poplack, W. A. Wells, G. N. Schwartz, R. M. di Florio-Alexander, T. D. Tosteson, Z. Li, *et al.*,

"Microwave imaging for neoadjuvant chemotherapy monitoring: Initial clinical experience," *Breast Cancer Research*, vol. 15, pp. 1–16, 2013.

[74] D. A. Soydan, C. B. Top, and N. G. Gençer, "On the utilization of the adjoint method in microwave tomography," *International Journal for Numerical Methods in Biomedical Engineering*, vol. 40, no. 6, p. e3818, 2024.

[75] J.-M. Jin, *Theory and computation of electromagnetic fields*. John Wiley & Sons, Second ed., 2015.

[76] A. Taflove, S. C. Hagness, and M. Piket-May, "Computational electromagnetics: the finite-difference time-domain method," *The Electrical Engineering Handbook*, vol. 3, no. 629-670, p. 15, 2005.

[77] K. Yee, "Numerical solution of initial boundary value problems involving maxwell's equations in isotropic media," *IEEE Transactions on Antennas and Propagation*, vol. 14, no. 3, pp. 302–307, 1966.

[78] J. A. Roden and S. D. Gedney, "Convolution PML (CPML): An efficient FDTD implementation of the CFS–PML for arbitrary media," *Microwave and optical technology letters*, vol. 27, no. 5, pp. 334–339, 2000.

[79] M. Kuzuoglu and R. Mittra, "Frequency dependence of the constitutive parameters of causal perfectly matched anisotropic absorbers," *IEEE Microwave and Guided Wave Letters*, vol. 6, no. 12, pp. 447–449, 1996.

[80] A. Fichtner, H.-P. Bunge, and H. Igel, "The adjoint method in seismology," *Physics of the Earth and Planetary Interiors*, vol. 157, pp. 86–104, Aug. 2006.

[81] M. Pérez-Liva, J. L. Herraiz, J. M. Udías, E. Miller, B. T. Cox, and B. E. Treeby, "Time domain reconstruction of sound speed and attenuation in ultrasound computed tomography using full wave inversion," *The Journal of the Acoustical Society of America*, vol. 141, pp. 1595–1604, Mar. 2017.

[82] F. Nicoud, "An adjoint-based method for the computation of gradients in coagulation schemes," *International Journal for Numerical Methods in Biomedical Engineering*, vol. 39, no. 5, 2023.

[83] D. Nolte and C. Bertoglio, “Inverse problems in blood flow modeling: A review,” *International Journal for Numerical Methods in Biomedical Engineering*, vol. 38, no. 8, 2022.

[84] S. Lohrengel, M. Mahmoudzadeh, F. Oumri, S. Salmon, and F. Wallois, “A homogenized cerebrospinal fluid model for diffuse optical tomography in the neonatal head,” *International Journal for Numerical Methods in Biomedical Engineering*, vol. 38, no. 1, 2022.

[85] H. Dehghani, S. Srinivasan, B. W. Pogue, and A. Gibson, “Numerical modelling and image reconstruction in diffuse optical tomography,” *Philosophical Transactions of the Royal Society A: Mathematical, Physical and Engineering Sciences*, vol. 367, pp. 3073–3093, Aug. 2009.

[86] A. SR, “Optical tomography in medical imaging,” *Inverse Problems*, vol. 15, p. R41, apr 1999.

[87] A. Klotzsche, H. Vereecken, and J. van der Kruk, “Review of crosshole ground-penetrating radar full-waveform inversion of experimental data: Recent developments, challenges, and pitfalls GPR FWI of experimental data,” *Geophysics*, vol. 84, no. 6, 2019.

[88] T. W. Hughes, I. A. Williamson, M. Minkov, and S. Fan, “Forward-mode differentiation of Maxwell’s equations,” *ACS Photonics*, vol. 6, no. 11, pp. 3010–3016, 2019.

[89] M. M. T. Maghrabi, M. H. Bakr, S. Kumar, A. Z. Elsherbeni, and V. Demir, “FDTD-dased adjoint sensitivity analysis of high-frequency nonlinear structures,” *IEEE Transactions on Antennas and Propagation*, vol. 68, no. 6, pp. 4727–4737, 2020.

[90] Q. Fang, P. Meaney, S. Geimer, A. Streltsov, and K. Paulsen, “Microwave image reconstruction from 3-D fields coupled to 2-D parameter estimation,” *IEEE Transactions on Medical Imaging*, vol. 23, no. 4, pp. 475–484, 2004.

[91] Q. Fang, P. M. Meaney, and K. D. Paulsen, “Viable three-dimensional medical microwave tomography: theory and numerical experiments,” *IEEE Transactions on Antennas and Propagation*, vol. 58, no. 2, pp. 449–458, 2010.

[92] P. M. Meaney, C. J. Fox, S. D. Geimer, and K. D. Paulsen, "Electrical characterization of glycerin : water mixtures: Implications for use as a coupling medium in microwave tomography," *IEEE Transactions on Microwave Theory and Techniques*, vol. 65, no. 5, pp. 1471–1478, 2017.

[93] S. Hosseinzadegan, A. Fhager, M. Persson, S. D. Geimer, and P. M. Meaney, "Discrete dipole approximation-based microwave tomography for fast breast cancer imaging," *IEEE Transactions on Microwave Theory and Techniques*, vol. 69, no. 5, pp. 2741–2752, 2021.

[94] S. Hosseinzadegan, A. Fhager, M. Persson, S. Geimer, and P. Meaney, "Expansion of the nodal-adjoint method for simple and efficient computation of the 2D tomographic imaging Jacobian matrix," *Sensors*, vol. 21, no. 3, 2021.

[95] T. Rubaek, P. M. Meaney, P. Meincke, and K. D. Paulsen, "Nonlinear microwave imaging for breast-cancer screening using Gauss–Newton's method and the CGLS inversion algorithm," *IEEE Transactions on Antennas and Propagation*, vol. 55, no. 8, pp. 2320–2331, 2007.

[96] D. G. Drogoudis, G. Kyriacou, and J. Sahalos, "Microwave tomography employing an adjoint network based sensitivity matrix," *Progress In Electromagnetics Research*, vol. 94, pp. 213–242, 2009.

[97] M. A. Islam, A. Kiourti, and J. L. Volakis, "A novel method to mitigate real–imaginary image imbalance in microwave tomography," *IEEE Transactions on Biomedical Engineering*, vol. 67, no. 5, pp. 1328–1337, 2020.

[98] M. El-Shenawee, O. Dorn, and M. Moscoso, "An adjoint-field technique for shape reconstruction of 3-D penetrable object immersed in lossy medium," *IEEE Transactions on Antennas and Propagation*, vol. 57, no. 2, pp. 520–534, 2009.

[99] O. Dorn and D. Lesselier, "Level set methods for inverse scattering," *Inverse Problems*, vol. 22, p. R67, jun 2006.

[100] P.-H. Tournier, I. Aliferis, M. Bonazzoli, M. De Buhan, M. Darbas, V. Dolean, F. Hecht, P. Jolivet, I. El Kanfoud, C. Migliaccio, *et al.*, "Microwave tomo-

graphic imaging of cerebrovascular accidents by using high-performance computing," *Parallel Computing*, vol. 85, pp. 88–97, 2019.

[101] P. Meaney, S. Geimer, A. Golnabi, and K. Paulsen, "Impact of skin on microwave tomography in the lossy coupling medium," *Sensors*, vol. 22, no. 19, p. 7353, 2022.

[102] Y. Song and N. K. Nikolova, "Memory-efficient method for wideband self-adjoint sensitivity analysis," *IEEE Transactions on Microwave Theory and Techniques*, vol. 56, no. 8, pp. 1917–1927, 2008.

[103] L. Liu, A. Trehan, and N. K. Nikolova, "Detection using microwaves and self-adjoint sensitivity analysis," *2010 URSI International Symposium on Electromagnetic Theory*, pp. 467–470, 2010.

[104] E. Abenius and B. Strand, "Solving inverse electromagnetic problems using fdtd and gradient-based minimization," *International Journal for Numerical Methods in Engineering*, vol. 68, no. 6, pp. 650–673, 2006.

[105] F. M. Saraskanroud and I. Jeffrey, "Hybrid approaches in microwave imaging using quantitative time- and frequency-domain algorithms," *IEEE Transactions on Computational Imaging*, vol. 8, pp. 121–132, 2022.

[106] A. Fhager, M. Gustafsson, and S. Nordebo, "Image reconstruction in microwave tomography using a dielectric Debye model," *IEEE Transactions on Biomedical Engineering*, vol. 59, no. 1, pp. 156–166, 2012.

[107] J. E. Johnson, T. Takenaka, and T. Tanaka, "Two-dimensional time-domain inverse scattering for quantitative analysis of breast composition," *IEEE Transactions on Biomedical Engineering*, vol. 55, no. 8, pp. 1941–1945, 2008.

[108] I. T. Rekanos, "Time-domain inverse scattering using lagrange multipliers: An iterative FDTD-based optimization technique," *Journal of Electromagnetic Waves and Applications*, vol. 17, no. 2, pp. 271–289, 2003.

[109] T. Takenaka, H. Jia, and T. Tanaka, "Microwave imaging of electrical property distributions by a forward-backward time-stepping method," *Journal of Electromagnetic Waves and Applications*, vol. 14, no. 12, pp. 1609–1626, 2000.

[110] E. J. Joseph, K. A. H. Ping, K. Kipli, D. A. A. Mat, S. Sahrani, D. N. A. Zaidel, M. I. Sariphn, and M. H. Marhaban, "Integration of image segmentation method in inverse scattering for brain tumour detection," *Progress In Electromagnetics Research M*, vol. 61, pp. 111–122, 2017.

[111] D. Gibbins, D. Byrne, T. Henriksson, B. Monsalve, and I. J. Craddock, "Less becomes more for microwave imaging: design and validation of an ultrawideband measurement array," *IEEE Antennas and Propagation Magazine*, vol. 59, no. 5, pp. 72–85, 2017.

[112] L. Beilina and E. Lindström, "An adaptive finite element/finite difference domain decomposition method for applications in microwave imaging," *Electronics*, vol. 11, no. 9, p. 1359, 2022.

[113] S. J. Norton, "Iterative inverse scattering algorithms: methods of computing Fréchet derivatives," *The Journal of the Acoustical Society of America*, vol. 106, pp. 2653–2660, Nov. 1999.

[114] A. Aghasi and E. L. Miller, "Sensitivity calculations for Poisson's equation via the adjoint field method," *IEEE Geoscience and Remote Sensing Letters*, vol. 9, pp. 237–241, Mar. 2012.

[115] T. Zhu, "Time-reverse modelling of acoustic wave propagation in attenuating media," *Geophysical Journal International*, vol. 197, pp. 483–494, Apr. 2014.

[116] G. A. Meles, S. A. Greenhalgh, A. G. Green, H. Maurer, and J. Van der Kruk, "GPR full-waveform Ssnsitivity and resolution analysis using an FDTD adjoint method," *IEEE Transactions on Geoscience and Remote Sensing*, vol. 50, pp. 1881–1896, May 2012.

[117] A. Hördt, "Calculation of electromagnetic sensitivities in the time domain," *Geophysical Journal International*, vol. 133, no. 3, pp. 713–720, 1998.

[118] M. Commer, *Three-dimensional inversion of transient-electromagnetic data: A comparative study.* Ph.D. Thesis, Universität zu Köln, 2003.

[119] G. S. Reuber and F. J. Simons, "Multi-physics adjoint modeling of earth structure: combining gravimetric, seismic, and geodynamic inversions," *GEM - International Journal on Geomathematics*, vol. 11, p. 30, Nov 2020.

[120] F. Lavoué, *2D Full waveform inversion of ground penetrating radar data : towards multiparameter imaging from surface data*. Ph.D Thesis, Université de Grenoble, July 2014.

[121] D.-H. Sheen, K. Tuncay, C.-E. Baag, and P. J. Ortoleva, "Time domain Gauss—Newton seismic waveform inversion in elastic media," *Geophysical Journal International*, vol. 167, no. 3, pp. 1373–1384, 2006.

[122] M. Mirzanejad, K. T. Tran, and Y. Wang, "Three-dimensional Gauss–Newton constant-Q viscoelastic full-waveform inversion of near-surface seismic wavefields," *Geophysical Journal International*, vol. 231, pp. 1767–1785, 07 2022.

[123] Y. Tao and M. K. Sen, "Frequency-domain full waveform inversion with a scattering-integral approach and its sensitivity analysis," *Journal of Geophysics and Engineering*, vol. 10, p. 065008, Dec. 2013.

[124] M. Mirzanejad, K. T. Tran, and Y. Wang, "Three-dimensional Gauss–Newton constant- Q viscoelastic full-waveform inversion of near-surface seismic wavefields," *Geophysical Journal International*, vol. 231, pp. 1767–1785, Sept. 2022.

[125] S. Hosseinzadegan, S. Geimer, A. Fhager, M. Persson, and P. Meaney, "Fast Jacobian matrix formulation for microwave tomography applications," *15th European Conference on Antennas and Propagation (EuCAP)*, 2021.

[126] A. Franchois and C. Pichot, "Microwave imaging-complex permittivity reconstruction with a Levenberg-Marquardt method," *IEEE Transactions on Antennas and Propagation*, vol. 45, pp. 203–215, Feb. 1997.

[127] P. Meaney, K. Paulsen, B. Pogue, and M. Miga, "Microwave image reconstruction utilizing log-magnitude and unwrapped phase to improve high-contrast object recovery," *IEEE Transactions on Medical Imaging*, vol. 20, pp. 104–116, Feb. 2001.

[128] A. Franchois and A. G. Tijhuis, "A quasi-Newton reconstruction algorithm for a complex microwave imaging scanner environment," *Radio Science*, vol. 38, Apr. 2003.

[129] J. Nocedal and S. J. Wright, *Numerical optimization*. New York: Springer, 2nd ed ed., 2006.

[130] J. Zaeytijd, A. Franchois, C. Eyraud, and J.-M. Geffrin, "Full-wave three-dimensional microwave imaging with a regularized Gauss–Newton method—theory and experiment," *IEEE Transactions on Antennas and Propagation*, vol. 55, no. 11, pp. 3279–3292, 2007.

[131] S. Coşğun, E. Bilgin, and M. Çayören, "Quasi-Newton-based inversion method for determining complex dielectric permittivity of 3-D inhomogeneous objects," *IEEE Transactions on Antennas and Propagation*, vol. 70, pp. 4810–4817, June 2022.

[132] F. Anis, Y. Lou, A. Conjusteau, R. Su, T. Oruganti, S. A. Ermilov, A. A. Oraevsky, and M. A. Anastasio, "Investigation of the adjoint-state method for ultrasound computed tomography: a numerical and experimental study," *Proc. SPIE 8943, Photons Plus Ultrasound: Imaging and Sensing*, 2014.

[133] S. Bernard, V. Monteiller, D. Komatitsch, and P. Lasaygues, "Ultrasonic computed tomography based on full-waveform inversion for bone quantitative imaging," *Physics in Medicine & Biology*, vol. 62, pp. 7011–7035, Aug. 2017.

[134] P. Marty, C. Boehm, and A. Fichtner, "Acoustoelastic full-waveform inversion for transcranial ultrasound computed tomography," *Proc. SPIE 11602, Medical Imaging: Ultrasonic Imaging and Tomography*, 2021.

[135] F. Lucka, M. Pérez-Liva, B. E. Treeby, and B. T. Cox, "High resolution 3D ultrasonic breast imaging by time-domain full waveform inversion," *Inverse Problems*, vol. 38, p. 025008, Feb. 2022.

[136] W. Chew and J. Lin, "A frequency-hopping approach for microwave imaging of large inhomogeneous bodies," *IEEE Microwave and Guided Wave Letters*, vol. 5, no. 12, pp. 439–441, 1995.

[137] Z. Miao and P. Kosmas, "Multiple-frequency dbim-twist algorithm for microwave breast imaging," *IEEE Transactions on Antennas and Propagation*, vol. 65, no. 5, pp. 2507–2516, 2017.

[138] F. M. Saraskanroud and I. Jeffrey, "A comparison of time-domain and frequency-domain microwave imaging of experimental targets," *IEEE Transactions on Computational Imaging*, vol. 7, pp. 611–623, 2021.

[139] P. Mojabi and J. LoVetri, "Ultrasound tomography for simultaneous reconstruction of acoustic density, attenuation, and compressibility profiles," *The Journal of the Acoustical Society of America*, vol. 137, pp. 1813–1825, Apr. 2015.

[140] C. Shin, K. Yoon, K. J. Marfurt, K. Park, D. Yang, H. Y. Lim, S. Chung, and S. Shin, "Efficient calculation of a partial-derivative wavefield using reciprocity for seismic imaging and inversion," *Geophysics*, vol. 66, pp. 1856–1863, 06 2001.

[141] J. R. Ernst, H. Maurer, A. G. Green, and K. Holliger, "Full-waveform inversion of crosshole radar data based on 2-D finite-difference time-domain solutions of Maxwell's equations," *IEEE Transactions on Geoscience and Remote Sensing*, vol. 45, no. 9, pp. 2807–2828, 2007.

[142] J. Virieux and S. Operto, "An overview of full-waveform inversion in exploration geophysics," *Geophysics*, vol. 74, pp. WCC1–WCC26, Nov. 2009.

[143] R. Modrak and J. Tromp, "Seismic waveform inversion best practices: regional, global and exploration test cases," *Geophysical Journal International*, vol. 206, pp. 1864–1889, Sept. 2016.

[144] F. Lavoué, R. Brossier, L. Métivier, S. Garambois, and J. Virieux, "Two-dimensional permittivity and conductivity imaging by full waveform inversion of multioffset GPR data: a frequency-domain quasi-Newton approach," *Geophysical Journal International*, vol. 197, pp. 248–268, Apr. 2014.

[145] Q. Fang, *Computational methods for microwave medical imaging*. Ph.D. Thesis, Dartmouth College, 2004.

[146] P. M. Meaney, C. J. Fox, S. D. Geimer, and K. D. Paulsen, "Electrical characterization of glycerin : water mixtures: Implications for use as a coupling medium in microwave tomography," *IEEE Transactions on Microwave Theory and Techniques*, vol. 65, no. 5, pp. 1471–1478, 2017.

[147] T. Rydholm, A. Fhager, M. Persson, and P. M. Meaney, "A first evaluation of the realistic supelec-breast phantom," *IEEE Journal of Electromagnetics, RF and Microwaves in Medicine and Biology*, vol. 1, no. 2, pp. 59–65, 2017.

[148] K. Levenberg, "A method for the solution of certain non-linear problems in least squares," *Quarterly of Applied Mathematics*, vol. 2, no. 2, pp. 164–168, 1944.

[149] D. W. Marquardt, "An algorithm for least-squares estimation of nonlinear parameters," *Journal of the Society for Industrial and Applied Mathematics*, vol. 11, no. 2, pp. 431–441, 1963.

[150] N. Joachimowicz, C. Pichot, and J. Hugonin, "Inverse scattering: an iterative numerical method for electromagnetic imaging," *IEEE Transactions on Antennas and Propagation*, vol. 39, no. 12, pp. 1742–1753, 1991.

[151] C. T. Kelley, *Iterative methods for linear and nonlinear equations*. SIAM, 1995.

[152] M. Lazebnik, M. Okoniewski, J. H. Booske, and S. C. Hagness, "Highly accurate Debye models for normal and malignant breast tissue dielectric properties at microwave frequencies," *IEEE Microwave and Wireless Components Letters*, vol. 17, no. 12, pp. 822–824, 2007.

[153] M. Palmeri, A. Sharma, R. Bouchard, R. Nightingale, and K. Nightingale, "A finite-element method model of soft tissue response to impulsive acoustic radiation force," *IEEE Transactions on Ultrasonics, Ferroelectrics, and Frequency Control*, vol. 52, no. 10, pp. 1699–1712, 2005.

[154] S. Stein and M. Wysession, *An introduction to seismology, earthquakes, and earth structure*. John Wiley & Sons, 2009.

[155] S. Calle, F. Patat, M. E. Hachemi, and J.-P. Remenieras, "A new numerical approach to simulate shear waves generated by a localized radiation force in heterogeneous media," in *2006 IEEE Ultrasonics Symposium*, pp. 1676–1679, 2006.

[156] J. Virieux, "P-SV wave propagation in heterogeneous media: Velocity-stress finite-difference method," *Geophysics*, vol. 51, no. 4, pp. 889–901, 1986.

[157] M. Orescanin, Y. Wang, and M. F. Insana, “3-D FDTD simulation of shear waves for evaluation of complex modulus imaging,” *IEEE Transactions on Ultrasonics, Ferroelectrics, and Frequency Control*, vol. 58, no. 2, pp. 389–398, 2011.

[158] R. W. Graves, “Simulating seismic wave propagation in 3D elastic media using staggered-grid finite differences,” *Bulletin of the Seismological Society of America*, vol. 86, no. 4, pp. 1091–1106, 1996.

[159] The MathWorks Inc., *MATLAB version: R2022b*, Natick, Massachusetts, United States,2022.

[160] COMSOL AB, *COMSOL Multiphysics® v. 5.6*, Stockholm, Sweden, 2021.

[161] Mads Herring Jensen, “Introduction to the elastic waves, time explicit interface.” https://www.comsol.com/blogs/introduction-to-the-elastic-waves-time-explicit-interface, 2020. [Online; accessed 14-July-2024].

[162] N. C. Rouze, M. H. Wang, M. L. Palmeri, and K. R. Nightingale, “Parameters affecting the resolution and accuracy of 2-D quantitative shear wave images,” *IEEE Transactions on Ultrasonics, Ferroelectrics, and Frequency Control*, vol. 59, no. 8, pp. 1729–1740, 2012.

[163] T. Deffieux, J.-l. Gennisson, J. Bercoff, and M. Tanter, “On the effects of reflected waves in transient shear wave elastography,” *IEEE Transactions on Ultrasonics, Ferroelectrics, and Frequency Control*, vol. 58, no. 10, pp. 2032–2035, 2011.

[164] A. Abu Bakar, A. Abbosh, and M. Bialkowski, “Fabrication and characterization of a heterogeneous breast phantom for testing an ultrawideband microwave imaging system,” in *Asia-Pacific Microwave Conference 2011*, pp. 1414–1417, 2011.

[165] B. Henin, A. M. Abbosh, and W. A. Abdulla, “Electro-biomechanical breast phantom for hybrid breast imaging,” in *2015 International Symposium on Antennas and Propagation (ISAP)*, pp. 1–3, 2015.

[166] M. Lazebnik, E. L. Madsen, G. R. Frank, and S. C. Hagness, "Tissue-mimicking phantom materials for narrowband and ultrawideband microwave applications," *Physics in Medicine & Biology*, vol. 50, no. 18, p. 4245, 2005.

[167] E. Porter, J. Fakhoury, R. Oprisor, M. Coates, and M. Popović, "Improved tissue phantoms for experimental validation of microwave breast cancer detection," in *Proceedings of the Fourth European Conference on Antennas and Propagation*, pp. 1–5, 2010.

[168] C. Hahn and S. Noghanian, "Heterogeneous breast phantom development for microwave imaging using regression models," *International Journal of Biomedical Imaging*, vol. 2012, no. 1, p. 803607, 2012.

[169] C. Kelly, J. Lobo, M. Honarvar, Y. Shao, and S. Salcudean, "An automated breast ultrasound scanner with integrated shear wave elastography, doppler flow imaging and photoacoustic tomography," in *2018 IEEE International Ultrasonics Symposium (IUS)*, pp. 1–4, 2018.

[170] H. M. Ismail, C. G. Pretty, M. K. Signal, M. Haggers, C. Zhou, and J. G. Chase, "Mechanical behaviour of tissue mimicking breast phantom materials," *Biomedical Physics & Engineering Express*, vol. 3, no. 4, p. 045010, 2017.

[171] S. Di Meo, L. Pasotti, I. Iliopoulos, M. Pasian, M. Ettorre, M. Zhadobov, and G. Matrone, "Tissue-mimicking materials for breast phantoms up to 50 GHz," *Physics in Medicine & Biology*, vol. 64, no. 5, p. 055006, 2019.

[172] C. B. Top, *Harmonic Motion Microwave Doppler Imaging Method*. Ph.D. Thesis, Middle East Technical University, 2013.

[173] A. K. Tafreshi, *Design and Realization of a Hybrid Medical Imaging System : Harmonic Motion Microwave Doppler Imaging*. Ph.D. Thesis, Middle East Technical University, 2016.

[174] CIRS Inc., "Multi-purpose multi-tissue ultrasound phantom model 040GSE." https://www.cirsinc.com/products/ultrasound/multi-purpose-multi-tisse-ultrasound-phantom. [Online; accessed 19-July-2024].

[175] P. Meaney, M. Fanning, D. Li, S. Poplack, and K. Paulsen, "A clinical prototype for active microwave imaging of the breast," *IEEE Transactions on Microwave Theory and Techniques*, vol. 48, no. 11, pp. 1841–1853, 2000.

[176] T. Rydholm, A. Fhager, M. Persson, and P. M. Meaney, "Comparing a time-domain and frequency-domain based algorithm in microwave tomography," *12th European Conference on Antennas and Propagation (EuCAP 2018)*, pp. 1–3, 2018.

[177] P. Meaney, K. Paulsen, and J. Chang, "Near-field microwave imaging of biologically-based materials using a monopole transceiver system," *IEEE Transactions on Microwave Theory and Techniques*, vol. 46, no. 1, pp. 31–45, 1998.

[178] A. Fhager, P. Hashemzadeh, and M. Persson, "Reconstruction quality and spectral content of an electromagnetic time-domain inversion algorithm," *IEEE Transactions on Biomedical Engineering*, vol. 53, no. 8, pp. 1594–1604, 2006.

[179] S. Semenov, A. Bulyshev, A. Abubakar, V. Posukh, Y. Sizov, A. Souvorov, P. van den Berg, and T. Williams, "Microwave-tomographic imaging of the high dielectric-contrast objects using different image-reconstruction approaches," *IEEE Transactions on Microwave Theory and Techniques*, vol. 53, no. 7, pp. 2284–2294, 2005.

[180] Verasonics Inc. https://verasonics.com. [Online; accessed 17-July-2024].

[181] Y. Deng, N. C. Rouze, M. L. Palmeri, and K. R. Nightingale, "Ultrasonic shear wave elasticity imaging sequencing and data processing using a verasonics research scanner," *IEEE Transactions on Ultrasonics, Ferroelectrics, and Frequency Control*, vol. 64, no. 1, pp. 164–176, 2017.

[182] G. Pinton, J. Dahl, and G. Trahey, "Rapid tracking of small displacements with ultrasound," *IEEE Transactions on Ultrasonics, Ferroelectrics, and Frequency Control*, vol. 53, no. 6, pp. 1103–1117, 2006.

[183] C. Kasai, K. Namekawa, A. Koyano, and R. Omoto, "Real-time two-dimensional blood flow imaging using an autocorrelation technique," *IEEE Transactions on Sonics and Ultrasonics*, vol. 32, no. 3, pp. 458–464, 1985.

[184] T. Loupas, J. Powers, and R. Gill, “An axial velocity estimator for ultrasound blood flow imaging, based on a full evaluation of the doppler equation by means of a two-dimensional autocorrelation approach,” *IEEE Transactions on Ultrasonics, Ferroelectrics, and Frequency Control*, vol. 42, no. 4, pp. 672–688, 1995.

[185] A. Rodriguez-Molares, O. M. H. Rindal, O. Bernard, A. Nair, M. A. Lediju Bell, H. Liebgott, A. Austeng, and L. Lvstakken, “The ultrasound toolbox,” in *2017 IEEE International Ultrasonics Symposium (IUS)*, pp. 1–4, 2017.

[186] M. H. Wang, M. L. Palmeri, V. M. Rotemberg, N. C. Rouze, and K. R. Nightingale, “Improving the robustness of time-of-flight based shear wave speed reconstruction methods using ransac in human liver in vivo,” *Ultrasound in Medicine & Biology*, vol. 36, no. 5, pp. 802–813, 2010.

[187] M. Tanter, J. Bercoff, A. Athanasiou, T. Deffieux, J.-L. Gennisson, G. Montaldo, M. Muller, A. Tardivon, and M. Fink, “Quantitative assessment of breast lesion viscoelasticity: Initial clinical results using supersonic shear imaging,” *Ultrasound in Medicine Biology*, vol. 34, no. 9, pp. 1373–1386, 2008.

[188] N. C. Rouze, M. H. Wang, M. L. Palmeri, and K. R. Nightingale, “Robust estimation of time-of-flight shear wave speed using a radon sum transformation,” in *2010 IEEE International Ultrasonics Symposium*, pp. 21–24, 2010.

[189] P. M. Meaney, E. Demidenko, N. K. Yagnamurthy, D. Li, M. W. Fanning, and K. D. Paulsen, “A two-stage microwave image reconstruction procedure for improved internal feature extraction,” *Medical Physics*, vol. 28, no. 11, pp. 2358–2369, 2001.

[190] R. G. Barr, K. Nakashima, D. Amy, D. Cosgrove, A. Farrokh, F. Schafer, J. C. Bamber, L. Castera, B. I. Choi, Y.-H. Chou, *et al.*, “WFUMB guidelines and recommendations for clinical use of ultrasound elastography: Part 2: breast,” *Ultrasound in Medicine & Biology*, vol. 41, no. 5, pp. 1148–1160, 2015.

[191] T. Deffieux, G. Montaldo, M. Tanter, and M. Fink, “Shear wave spectroscopy for in vivo quantification of human soft tissues visco-elasticity,” *IEEE Transactions on Medical Imaging*, vol. 28, no. 3, pp. 313–322, 2009.

[192] Y. Yang, M. W. Urban, and R. J. McGough, "GPU-based Green's function simulations of shear waves generated by an applied acoustic radiation force in elastic and viscoelastic models," *Physics in Medicine & Biology*, vol. 63, no. 10, p. 10NT01, 2018.

[193] S. L. Lipman, N. C. Rouze, M. L. Palmeri, and K. R. Nightingale, "Evaluating the improvement in shear wave speed image quality using multidimensional directional filters in the presence of reflection artifacts," *IEEE Transactions on Ultrasonics, Ferroelectrics, and Frequency Control*, vol. 63, no. 8, pp. 1049–1063, 2016.

[194] H. Zhao, P. Song, M. W. Urban, R. R. Kinnick, M. Yin, J. F. Greenleaf, and S. Chen, "Bias observed in time-of-flight shear wave speed measurements using radiation force of a focused ultrasound beam," *Ultrasound in Medicine & Biology*, vol. 37, no. 11, pp. 1884–1892, 2011.

[195] J. Bercoff, M. Tanter, and M. Fink, "Supersonic shear imaging: a new technique for soft tissue elasticity mapping," *IEEE Transactions on Ultrasonics, Ferroelectrics, and Frequency Control*, vol. 51, no. 4, pp. 396–409, 2004.

[196] P. Song, H. Zhao, A. Manduca, M. W. Urban, J. F. Greenleaf, and S. Chen, "Comb-push ultrasound shear elastography (CUSE): A novel method for two-dimensional shear elasticity imaging of soft tissues," *IEEE Transactions on Medical Imaging*, vol. 31, no. 9, pp. 1821–1832, 2012.

APPENDIX A

TISSUE MOTION ESTIMATION

In this thesis study, the tissue motion estimation is done using the ultrasound toolbox USTB [185] in MATLAB. The purpose of this appendix is to supplement information about tissue motion algorithms used in Chapter 5.

In ultrasound applications, tissue motion estimations are generally achieved using phase shift algorithms. Two of the commonly used phase shift algorithms are Kasai [183] and Loupas [184] algorithms. Kasai algorithm is readily available in the Verasonics system, and Loupas algorithm is available ultrasound toolbox USTB.

The Kasai algorithm [183], also called as the 1-D autocorrelator, developed to estimate blood flow velocity in Doppler systems. Using the beamformed in-phase and quadrature (IQ) data, displacement between a reference and displaced signal is determined by measuring the average phase shift with respect to the constant center frequency.

On the other hand, Loupas algorithm, also called as the 2-D autocorrelator, uses information from the depth samples and the pulses within an axial range to calculate the displacement. Lopuas algorithm accounts for the change in the center frequencies of the RF echoes at each axial position and leads to more accurate results.

Using Kasai algorithm, the displacement can be expressed as [182]

$$\bar{u} = \frac{c}{4\pi f_c} \arctan\left(\frac{\sum\limits_{n=0}^{N-2}\left[\sum\limits_{m=0}^{M-1} Q(m,n) \sum\limits_{m=0}^{M-1} I(m,n+1) - \sum\limits_{m=0}^{M-1} I(m,n) \sum\limits_{m=0}^{M-1} Q(m,n+1)\right]}{\sum\limits_{n=0}^{N-2}\left[\sum\limits_{m=0}^{M-1} I(m,n) \sum\limits_{m=0}^{M-1} I(m,n+1) + \sum\limits_{m=0}^{M-1} Q(m,n) \sum\limits_{m=0}^{M-1} Q(m,n+1)\right]} \right), \tag{A.1}$$

and using Loupas algorithm, the displacement can be expressed as [182]

$$\bar{u} = \frac{c}{4\pi f_c} \frac{\arctan\left(\frac{\sum_{m=0}^{M-1}\sum_{n=0}^{N-2}[Q(m,n)I(m,n+1)-I(m,n)Q(m,n+1)]}{\sum_{m=0}^{M-1}\sum_{n=0}^{N-2}[I(m,n)I(m,n+1)+Q(m,n)Q(m,n+1)]}\right)}{1+\arctan\left(\frac{\sum_{m=0}^{M-2}\sum_{n=0}^{N-1}[Q(m,n)I(m+1,n)-I(m,n)Q(m+1,n)]}{\sum_{m=0}^{M-2}\sum_{n=0}^{N-1}[I(m,n)I(m+1,n)+Q(m,n)Q(m+1,n)]}\right)/2\pi}, \tag{A.2}$$

where $\bar{u}$ is the average displacement estimate over a given axial range, M, and an ensemble length of N. c is the speed of sound, f_c is the center frequency of the RF signal, and I and Q are the in-phase and quadrature components of the RF signal.

CURRICULUM VITAE

PERSONAL INFORMATION

Surname, Name: Alptekin Soydan, Damla

EDUCATION

Degree	Institution	Year of Grad.
M.S.	METU Electrical–Electronics Engineering	2015
B.S.	METU Electrical–Electronics Engineering	2012

PROFESSIONAL EXPERIENCE

Year	Place	Enrollment
2012–2013	ASELSAN A.S.	Engineer
2013–2014	METU	Research Assistant
2014–2020	METU	Reasearch & Teaching Assistant
2020–Present	ASELSAN A.S.	Engineer

PUBLICATIONS

Journal Articles

Soydan DA, Top C.B., Gençer N.G., On the utilization of the adjoint method in microwave tomography. *Int J Numer Meth Biomed Engng*. 2024; 40(6):e3818., doi:10.1002/cnm.3818 (Accepted: 17 March 2024)

(In progress) **Soydan DA,** Top CB, Gençer N.G., Multi-Modal Quantitative Microwave and Shear Wave Imaging for Breast Tumor Identification, *will be submitted.*

Conference Papers

Soydan, D.A., İrgin, Ü., Top, C.B. and Gençer, N.G. , An Improved Receiver for Harmonic Motion Microwave Doppler Imaging 14th European Conference on Antennas and Propagation (EuCAP) pp. 1-5. IEEE, 2020

İrgin Ü. , Top C. B. , **Soydan D. A.** and Gençer N. G., Enhancing the sensitivity of Harmonic Motion Microwave Doppler Imaging using main signal cancellation circuit," 12th European Conference on Antennas and Propagation (EuCAP 2018), London, 2018

Alptekin D., Alatan L., and Gençer N. G."Dual band PIFA design for biomedical applications," in, Proc. European Conf. on Antennas and Propagation (EuCAP), 2016

Alptekin D., Alatan L., and Gençer N. G.Performance analysis of an implantable antenna, in Turkish, Biomedical Engineering Meting (BIYOMUT), 2016

Alptekin D., Gençer N. G."A dual band antenna design for implantable medical devices," in Turkish, Biomedical Engineering Meting (BIYOMUT), 2014

Other Journal Articles and Conference Papers

A. Güngör, B. Askin, **D. A. Soydan**, C. B. Top, E. U. Saritas and T. Çukur, "DEQ-MPI: A Deep Equilibrium Reconstruction With Learned Consistency for Magnetic Particle Imaging," *IEEE Transactions on Medical Imaging*, vol. 43, no. 1, pp. 321-334, Jan. 2024

Kilic, B., **Soydan, D.A.**, Güngör, A. and Top, C.B, Inverse Radon transform-based reconstruction with an open-sided magnetic particle imaging prototype Signal, Image and Video Processing17(4), pp.1563-1570., 2023

Soydan, D.A., Karaca S., Güngör, A. and Top, C.B. , 3D Trajectory Analysis for Tomographic Field Free Line Magnetic Particle Imaging International Journal on Magnetic Particle Imaging IJMPI9(1 Suppl 1), 2023

Gungor, A., Aşkın, B., **Soydan, D.A.**, Saritas, E.U., Top, C.B. and Çukur, T. , A Denoiser Scaling Technique for Plug-and-Play MPI Reconstruction International Journal on Magnetic Particle Imaging IJMPI9(1 Suppl 1), 2023

Karaca, S., **Soydan, D.A.**, Top, C.B. and Saritas, E.U. , A Simulation Study for an Open-Sided Hybrid MPI-MRI Scanner International Journal on Magnetic Particle Imaging IJMPI9(1 Suppl 1), 2023

Güngör, A., Askin, B., **Soydan, D.A.**, Saritas, E.U., Top, C.B. and Çukur, T. , TranSMS: Transformers for super-resolution calibration in magnetic particle imaging, IEEE Transactions on Medical Imaging Signal, Image and Video Processing41(12), pp.3562-3574, 2022

Soydan, D.A., Karaca S., and Top, C.B. Increasing the efficiency of open-sided field free line scanning MPI system using silicon-steel core International Journal on Magnetic Particle Imaging IJMPI8(1 Suppl 1), 2022

Soydan, D.A., Karaca S., and Top, C.B. , Effect of Steel Loading on the Background Signal of an Open-Sided MPI System 30th Signal Processing and Communications Applications Conference (SIU) pp. 1-4. IEEE, 2022

Askin, B., Güngör, A., **Soydan, D.A.**, Saritas, E.U., Top, C.B. and Cukur, T , PP-MPI: A deep plug-and-play prior for magnetic particle imaging reconstruction International Workshop on Machine Learning for Medical Image Reconstruction (pp. 105-114. Springer International Publishing, 2022

Soydan, D.A., Güngör, A. and Top, C.B A Simulation Study for Three Dimensional Tomographic Field Free Line Magnetic Particle Imaging 43rd Annual International Conference of the IEEE Engineering in Medicine & Biology Society (EMBC)(pp. 3701-3704. IEEE, 2021

Güngör, A., Askin, B., **Soydan, D.A.**, Top, C.B. and Cukur, T. , Deep learned super resolution of system matrices for magnetic particle imaging 43rd Annual International Conference of the IEEE Engineering in Medicine & Biology Society (EMBC) (pp. 3749-3752. IEEE, 2021

Askin, B., Güngör, A., **Soydan, D.A.**, Top, C.B. and Cukur, T , A CNN based super-resolution technique for magnetic particle imaging system matrix 29th Signal Processing and Communications Applications Conference (SIU)(pp. 1-4.) IEEE, 2021

Awards & Grants

2021 *Best Student Paper Finalist* Student Paper Competition IEEE Engineering in Medicine and Biology Society (EMBC2021)

2021 *Best Paper Award* IEEE 30th Signal Processing and Communications Applications Conference (SIU2021)

2017 *Full Scholarship* Diagnostic and Therapeutic Applications of Electromagnetics, European School of Antennas, 11-15 Sept., Napoli, Italy.

2016 1^{st} *Place Best Presentation*, Graduate Student Academic Research Workshop Electrical and Electronics Engineering, METU

2016 *Best Poster* Graduate Student Academic Research Workshop Electrical and Electronics Engineering, METU

2016 *Full Scholarship* School on Microwave Imaging and Diagnostics, European School of Antennas, 10-14 Oct., Taormina, Italy.